

# A Discontinuous Galerkin Method for Diffusion Flames

**Embedded in a low-Mach solver framework**

Zur Erlangung des akademischen Grades Doktor-Ingenieur (Dr.-Ing.)

Vorgelegte Dissertation von Juan Francisco Gutiérrez Jorquera aus Santiago, Chile

Tag der Einreichung: 25. Oktober 2022, Tag der Prüfung: 25. Oktober 2022

Erstreferent: Prof. Dr.-Ing Martin Oberlack

Koreferent: Gutachter 2

Darmstadt



TECHNISCHE  
UNIVERSITÄT  
DARMSTADT

Fachbereich Maschinenbau  
Fachgebiet für  
Strömungsdynamik

A Discontinuous Galerkin Method for Diffusion Flames  
Embedded in a low-Mach solver framework

Vorgelegte Dissertation von Juan Francisco Gutiérrez Jorquera

Tag der Einreichung: 25. Oktober 2022  
Tag der Prüfung: 25. Oktober 2022

Darmstadt

Bitte zitieren Sie dieses Dokument als:  
URN: urn:nbn:de:tuda-tuprints-1234  
URL: <http://tuprints.ulb.tu-darmstadt.de/12345>  
DOI: <https://doi.org/10.25534/tuprints-1234>

Dieses Dokument wird bereitgestellt von tuprints,  
E-Publishing-Service der TU Darmstadt  
<http://tuprints.ulb.tu-darmstadt.de>  
[tuprints@ulb.tu-darmstadt.de](mailto:tuprints@ulb.tu-darmstadt.de)

Die Veröffentlichung steht unter folgender Creative Commons Lizenz:  
Namensnennung 4.0 International  
<https://creativecommons.org/licenses/by/4.0/>  
This work is licensed under a Creative Commons License:  
Attribution 4.0 International  
<https://creativecommons.org/licenses/by/4.0/>

*Dedication*



---

---

## **Erklärungen laut Promotionsordnung**

---

### **§ 8 Abs. 1 lit. c PromO**

---

Ich versichere hiermit, dass die elektronische Version meiner Dissertation mit der schriftlichen Version übereinstimmt.

### **§ 8 Abs. 1 lit. d PromO**

---

Ich versichere hiermit, dass zu einem vorherigen Zeitpunkt noch keine Promotion versucht wurde. In diesem Fall sind nähere Angaben über Zeitpunkt, Hochschule, Dissertationsthema und Ergebnis dieses Versuchs mitzuteilen.

### **§ 9 Abs. 1 PromO**

---

Ich versichere hiermit, dass die vorliegende Dissertation selbstständig und nur unter Verwendung der angegebenen Quellen verfasst wurde.

### **§ 9 Abs. 2 PromO**

---

Die Arbeit hat bisher noch nicht zu Prüfungszwecken gedient.

Darmstadt, 25. Oktober 2022

---

J. Gutiérrez-Jorquera





---

## **Abstract**

---

Abstract





---

# **Zusammenfassung**

---

Zusammenfassung





---

## Acknowledgements

---

Acknowledgements



---

# Contents

---

<b>List of Figures</b>	<b>xv</b>
<b>List of Tables</b>	<b>xvii</b>
<b>List of Abbreviations</b>	<b>xix</b>
<b>List of Symbols</b>	<b>xxi</b>
<b>1 Introduction</b>	<b>1</b>
1.1 Introduction and state of the art . . . . .	1
1.1.1 Combustion . . . . .	1
<b>2 Governing equations</b>	<b>5</b>
2.1 The low-Mach number equations for reactive flows . . . . .	5
2.1.1 The reactive Navier–Stokes equations . . . . .	5
2.1.2 The unsteady non-dimensional low-Mach equations . . . . .	9
2.2 The flame sheet approximation . . . . .	12
2.3 Boundary conditions . . . . .	14
<b>3 Numerical methods</b>	<b>15</b>
3.1 The Discontinuous Galerkin method . . . . .	15
3.1.1 Spatial discretization . . . . .	15
3.1.2 Discretization for a DG Method . . . . .	16
3.1.3 Temporal discretization . . . . .	21
3.2 Computational methodology . . . . .	22
3.2.1 Dogleg Method . . . . .	23
3.2.2 Termination criterion . . . . .	25
3.2.3 Solver safeguard . . . . .	25
3.2.4 Homotopy method . . . . .	25
3.2.5 Initialization of combustion applications . . . . .	27
<b>4 Results</b>	<b>31</b>
4.1 Single-component isothermal cases . . . . .	31
4.1.1 Lid-driven cavity flow . . . . .	31
4.1.2 Backward-facing step . . . . .	33
4.2 Single-component non-isothermal cases . . . . .	36
4.2.1 Heated backward-facing step . . . . .	36
4.2.2 Couette flow with vertical temperature gradient . . . . .	38
4.2.3 Differentially heated cavity problem . . . . .	42
4.2.4 Flow over a circular cylinder . . . . .	49
4.2.5 Rayleigh–Bénard Convection . . . . .	52

4.3	Multi-component non-isothermal cases . . . . .	59
4.3.1	Co-flow laminar diffusion flame . . . . .	59
4.3.2	Counterflow diffusion flame . . . . .	65
4.3.3	Chambered diffusion flame . . . . .	73
<b>5</b>	<b>Conclusion</b>	<b>75</b>
	<b>Bibliography</b>	<b>77</b>
	<b>Curriculum vitae</b>	<b>83</b>

---

# List of Figures

---

2.1	Temperature and fuel mass fraction profiles calculated in the center-line of a counter-flow flame configuration using finite chemistry (black) and the flame sheet approximation (green). . . . .	14
3.1	Behaviour of the homotopy method for the differentially heated cavity test case. The homotopy parameter $hp$ in this case is the Reynolds number. . . . .	26
3.2	Temperature profile calculated in the center-line of a counter-flow flame configuration for different smoothing parameters $\sigma$ . . . . .	29
4.1	Schematic representation of the Lid-Driven cavity flow. . . . .	32
4.2	Mesh and streamlines of the lid-driven cavity flow with $Re = 1000$ . . . . .	32
4.3	Calculated velocities along the centerlines of the cavity and reference values. Left plot shows the x-velocity for $x = 0.5$ . Right plot shows the y-velocity for $y = 0.5$ . . . . .	33
4.4	Schematic representation of the backward-facing step. Both primary and secondary vortices are shown. Sketch is not to scale. . . . .	34
4.5	Structured mesh used in all calculations. . . . .	35
4.6	Distribution of x-component of velocity in the backward-facing step configuration for a Reynolds number of 400. Solid lines correspond to results obtained with the XNSEC solver . . . . .	35
4.7	Detachment and reattachment lengths of the primary (left figure) and secondary (right figure) recirculation zones after the backward-facing step compared to the reference solution (Biswas et al., 2004). . . . .	36
4.8	Temperature profile and streamlines corresponding to the backward-facing Step configuration for $Re = 400$ and an expansion ratio of two. . . . .	37
4.9	Local friction factor and local Nusselt number along the bottom wall for $Re = 700$ and an expansion ratio of two. The solid lines corresponds to our solution and the marks to the reference (Hennink, 2022) . . . . .	38
4.10	Schematic representation of the Couette flow with temperature difference test case. . . . .	39
4.11	Solution of the Couette flow with vertical temperature gradient using a Power-Law. . . . .	40
4.12	Convergence study of the Couette-flow with temperature difference. A power-law is used for the transport parameters. . . . .	41
4.13	Schematic representation of the differentially heated cavity problem. . . . .	43
4.14	Streamlines of the heated cavity configuration with $\epsilon = 0.6$ . . . . .	45
4.15	Temperature profiles for the differentially heated square cavity along different vertical levels. Solid lines represent the XNSEC-solver solution and marks the benchmark solution. . . . .	45
4.16	Profiles of the x-velocity component along the vertical line $x = 0.5$ . Solid lines represent the XNSEC-solver solution and marks the benchmark solution. . . . .	46

4.17 Profiles of the y-velocity component along the horizontal line $y = 0.5$ . Solid lines represents the XSEC-solver solution and marks the benchmark solution.	46
4.18 Convergence study of the differentially heated cavity problem for $\text{Ra} = 10^3$ . . . . .	48
4.19 Nusselt numbers calculated with Equation (4.16) at the hot wall ( $\text{Nu}_h$ ) and the cold wall ( $\text{Nu}_c$ ) for different number of cells and polynomial order $k$ . The reference values from Vierendeels et al., 2003 are shown with dashed lines. . . . .	49
4.20 Schematic representation of the heated circular cylinder. . . . .	50
4.21 Temporal evolution of average Nusselt number, lift coefficient and drag coefficient of the heated cylinder . . . . .	52
4.22 Geometry of the Rayleigh-Bénard convection problem. Convection rolls are sketched . . . . .	53
4.23 Maximum x-velocity in the Rayleigh-Bénard convection configuration for different $a$ and $r$ . . . . .	54
4.24 Stability behaviour of the Rayleigh-Bénard convection with $\epsilon = 0.0001$ . . . . .	55
4.25 Critical Rayleigh number at different temperatures and different reference temperatures. . . . .	55
4.26 Temperature field and contours of a Rayleigh-Bénard convection roll . . . . .	57
4.27 Streamlines of a Rayleigh-Bénard convection roll . . . . .	57
4.28 Geometry of the Rayleigh-Bénard convection with pressure outlet boundary conditions. . . . .	58
4.29 Temperature, streamlines and vorticity of the Rayleigh-Bénard flow with pressure outlets. . . . .	59
4.30 Geometry of a coflowing flame configuration (not to scale). . . . .	60
4.31 Typical convergence history of a diffusion flame in the coflowing flame configuration. A mesh refinement was done at iteration 21. . . . .	62
4.32 Solution field of a coflow flame configuration. . . . .	64
4.33 Schematic representation of the counterflow configuration. . . . .	65
4.34 Nondimensional solution and derived fields of the counterflow flame configuration for case (a). . . . .	68
4.34 Solution and derived fields of the counterflow flame configuration with a strain of $34 \text{ s}^{-1}$ (continued). . . . .	69
4.35 Comparison of the axial velocity calculated with the XSEC-solver and the one-dimensional approximation. . . . .	70
4.36 Comparison of temperature and mass fraction fields obtained with BoSSS and the one-dimensional approximation. . . . .	71
4.37 Maximum value of the temperature for the counter diffusion flame configuration, for different mesh sizes in the x-direction and polynomial degrees. Values for $k = 1$ are not shown, because for this range of cell lengths the maximum temperature value was of the order of 50K higher than the ones depicted here.	72
4.38 Schematic representation of the chambered diffusion flame configuration. . . . .	73
4.39 Convergence study for the chambered diffusion flame configuration. . . . .	74

---

## List of Tables

---

2.1	Base parameters used in the one-step combustion model by Fernandez-tarrazo et al., 2006 . . . . .	9
4.1	Extrema of velocity components through the centerlines of the lid-driven cavity for $Re = 1000$ . Reference values obtained from Botella and Peyret, 1998 . . . . .	33
4.2	Runtime comparison of the DG-SIMPLE solver and the XNSEC-solver for the Couette flow with vertical temperature gradient . . . . .	42
4.3	Differentially heated cavity: Results of Nusselt number and Thermodynamic pressure . . . . .	47



---

---

## List of Abbreviations

---

$\mathbf{u}_{\text{ext}}$  Extension-velocity field



---

# List of Symbols

---

$\Omega$	Domain of interest, computational domain
$\partial\Omega$	Domain boundary
$\mathfrak{A}$	Bulk phase A
$\mathfrak{B}$	Bulk phase B
$s$	Bulk phase, species
$\Omega \setminus \mathfrak{I}$	Bulk
$\mathfrak{I}$	Interface
$w$	Singular surface velocity vector
$w$	Normal component of the singular surface velocity
$\mathbf{u}_{\mathfrak{I}}$	Material interface velocity vector
$\mathbf{n}_{\partial\Omega}$	Outer boundary normal vector
$\mathbf{n}_{\mathfrak{I}}$	Interface normal vector
$n$	Normal vector
$\tau$	Tangent vector
$P_{\mathfrak{I}}$	Interface projection tensor
$P$	Projection tensor
$\mathbf{u}$	Velocity vector
$p$	Pressure
$e_{\text{kin}}$	Kinetic energy
$e_{\sigma}$	Surface energy
$\psi$	General field/physical property
$\mathbf{f}$	Flux vector
$\mu$	Dynamic viscosity
$\nu$	Kinematic viscosity
$\sigma$	Surface tension coefficient
$\kappa$	Mean curvature
$\mathbf{D}$	Rate of deformation tensor
$\mathbf{S}$	Stress tensor
$\theta$	Apparent contact angle
$\theta_{\text{stat}}$	Static contact angle
$L$	Contact line
$l_{\text{cap}}$	Capillary length
$l_s$	Slip length
$\mathbf{n}_L$	Contact line normal vector
$U_L$	Contact line velocity
$\beta$	Coefficient of friction
$c_p$	Specific heat capacity of the mixture

$c_{p,k}$	Specific heat capacity of species $k$
$T$	Temperature
$T_{\text{sat}}$	Saturation temperature
$\mathbf{q}$	Heat flux vector
$c$	Specific heat capacity
$k$	Thermal conductivity
$\rho$	Density
$\dot{m}$	Mass transfer rate
$h_{\text{vap}}$	Enthalpy/(latent) heat of vaporization
$D$	Diffusion coefficient
$\nu_k$	Stoichiometric coefficient of species $k$
$A$	Aggregation map
$\mathcal{A}gg$	Aggregation mesh
$N_k$	Number of local DOF
$N$	Number of total DOF
$\mathbf{Op}$	Operator matrix
$k$	Total degree of the polynomial space
$\alpha$	Aggregation threshold
$\phi$	Basis function
$\mathbb{P}_k$	Broken polynomial space
$K$	Numerical cell
$K^{\mathbf{X}}$	Numerical cut-cell
$\mathbf{X}$	Cut
$\Delta t$	Time step size
$\Gamma_D$	Edge imposed with Dirichlet boundary condition
$\Gamma_{\text{int}}$	Internal edge
$\Gamma_N$	Edge imposed with Neumann boundary condition
$\Gamma$	Edge
$h$	Numerical mesh size
$\mathfrak{K}_{\text{cc}}$	Set of cut-cells
$\mathfrak{K}_{\text{far}}$	Set of far-field cells
$\mathfrak{K}_{\text{near}}$	Set of cut-cell neighbours
$\mathfrak{K}_h^{\mathbf{X}}$	Numerical cut-cell mesh
$\mathfrak{K}_h$	Numerical mesh
$\varphi$	Level-set function
$Edg$	Logical edge
$\mathbf{M}$	Mass matrix
$\mathbf{n}_{\Gamma}$	Edge normal field
$\mathbf{n}_{\mathfrak{I},\Gamma}$	Edge normal field including the interface normal vector
$\hat{F}$	Numerical flux
$\varphi^{\text{dg}}$	Level-set function represented by a DG field
$\varphi^{\text{co}}$	Constrained level-set function represented by a DG field
$\eta$	Penalty parameter
$\mathbb{V}_k^{\mathbf{X}}$	Sum of broken polynomial spaces
$\vartheta$	General test function

$q$	Test function for the continuity equation
$r$	Test function for the heat equation
$v$	Test function for the momentum equation
<b>ER</b>	Expansion ratio the backward-facing step
<b>Eo</b>	tvös number
<b>La</b>	Laplace number
<b>Pe</b>	Peclet number
<b>Fr</b>	Froude number
$\omega$	Oscillation frequency
$\lambda$	Wavelength
$k$	Wavenumber
<b>g</b>	Gravity vector
<b>h</b>	Channel heighth of the backward-facing step
$\hat{h}$	Convective heat transfer coefficient
$\lambda$	Heat conductivity
$h_k$	Specific enthalpy of $k$ species.
$Y_k$	Mass fraction of species $k$
$W$	Mean molecular weight of the mixture
$W_k$	Molecular weight of species $k$
$N$	Total number of species in the mixture
<b>Nu</b>	Nusselt number
<b>Nu<sub>loc</sub></b>	Nusselt number, local
$\omega_k$	Net rate of production of species $k$
<b>Pr</b>	Prandtl number
$p$	Pressure
<b>R</b>	Universal gas constant
<b>Re</b>	Reynolds number
<b>S</b>	Step heighth of the backward-facing step
$\tau$	Viscous tensor
$t$	Time
<b>u</b>	Velocity vector
$D$	Diffusion coefficient
<b>U</b>	Diffusion velocity vector



# 1 Introduction

---

## 1.1 Introduction and state of the art.

---

### 1.1.1 Combustion

---

**Premixed Flames(???)**

---

**Non-Premixed Flames**

---

**Droplet(?)**

---

High order discretization methods is a topic which has been gaining increasing attention in the last decades. An important exponent of them is the Discontinuous Galerkin (DG) method Cockburn et al., 2000. The DG method was initially developed and utilized for solving hyperbolic conservation laws, especially in the field of computational fluid dynamics (CFD), and has recently gained increased attention for incompressible CFD problems for structured and unstructured grids. Two main advantages stand out when compared with traditional methods such as the Finite Volume Method (FVM) or the Finite Difference Method (FDM): First, DG offers an arbitrary order of error convergence due to the polynomial local approximation of the solution field. A polynomial approximation of degree  $p$  provides a numerical discretization error of the order  $\mathcal{O}(h^{p+1})$  for sufficiently smooth solutions, where  $h$  is a characteristic grid length. Secondly, regardless of the desired order of accuracy, any given cell of the grid only requires information from its immediate neighbours, allowing for efficient parallelization with minimal communication overhead. In contrast, more traditional schemes, such as the FVM, are usually limited to  $\mathcal{O}(h^N)$  accuracy, with  $N \leq 2$  for unstructured grids. Even for structured grids  $N$  is practically limited to low values due to the increasing stencil size for increasing  $N$ . Advantageously the DG method offers the locality of low-order schemes and the accuracy per degree of freedom of spectral schemes.

In the context of CFD solvers, an important distinction is that between pressure-based and density-based solvers. Historically, pressure-based solvers have been used for incompressible flows, i.e. flows with divergence-free velocity fields. On the other hand, density-based (also called fully compressible) solvers should, in theory, be able to solve flows in all Mach number ranges. However, in practice, as the Mach number approaches zero, density-based solvers experience efficiency and accuracy problems. These issues are mainly attributed to the acoustic effects in the flow, which tends to generate very stiff systems. None of these approaches are directly applicable to flows with varying density in the low-Mach limit. Hennink et al., 2021 It is possible, however, to extend existing incompressible and compressible codes so that they are capable of dealing with low Mach numbers. Keshtiban et al., 2003 In this work a extension from an incompressible solver is presented.

There are numerous works in which the DG method has been used within the context of

incompressible flows. Shahbazi et al., 2007; Kummer, 2012; Klein et al., 2013; Rhebergen et al., 2013 However, there are not many publications in which the flow problem at low Mach numbers is addressed using a pressure-based solver. In the work by Klein et al. Klein et al., 2016 the low-Mach equations are solved in a DG Framework making use of a SIMPLE type scheme. The solution of a time-step involves an iterative process that requires multiple matrix assemblies and solutions. The obtained systems of equations are solved by means of fixed-point iterations, where relaxation factors are necessary to obtain convergence of the computations. In the work of Hennink et al. Hennink et al., 2021 a pressure-based solver for low-mach flows is presented. They solve the mass flux instead of the velocity as the primitive variable.

High order methods are very attractive for complex reacting fluid dynamical systems, where usually a high numerical resolution is necessary. Particularly for combustion problems, where large amounts of heat are released in rather small zones within the flow, the high number of elements required to resolve the resulting steep gradients could result in prohibitive calculation times even for simple problems. In particular the study of so-called diffusion flames – also known as non-premixed flames – requires special consideration. In a diffusion flame, the reactants are initially spatially separated. For this kind of system, mixing plays a crucial role because reactants need to be brought together to the flame zone in order to maintain combustion. Many practical applications of diffusion flames consider deflagration flames, Poinsot and Veynante, 2005 which are characterized by a small characteristic velocity compared to the speed of sound. The low-Mach approximation of the Navier–Stokes equations is often chosen for describing this kind of system. This approximation allows for the calculation of non-constant density flows (such as temperature dependent density), while neglecting acoustic effects, thus dramatically reducing the required temporal resolution. Müller, 1998

In addition to the compressibility effects mentioned above, the need to accurately and efficiently represent the chemical reactions governing the combustion problem poses a major challenge. Generally speaking, to study the combustion process a detailed chemistry description is preferable. However, this is often impractical as it can be very intensive computationally speaking. Stauch et al. investigated systems with detailed mechanism for methanol combustion, where 23 chemical species and 166 elementary reactions are involved, Stauch et al., 2006 and for n-heptane with 62 chemical species and 572 elementary reactions, and with detailed transport processes Stauch and Maas, 2007. Because of their high complexity the mentioned works are restricted to simple one- or two-dimensional configurations, and to a small number of grid elements. If one is interested in more complex geometries or more complicated flow systems, the use of detailed kinetics can be prohibitive. Simplified kinetic models have been developed to overcome this difficulty. In the work of Westbrook et al. Westbrook and Dryer, 1981 a one-step kinetic model is presented, where combustion is expressed as a single chemical reaction with a reaction rate given by an Arrhenius-type expression with constant parameters. Multi-step chemical reaction models have also been developed, such as the four-step mechanism for methane combustion by Peters, Peters, 1985 or the three-step mechanism by Peters and Williams. Peters and Williams, 1987 Furthermore, extensions of one-step models exist, such as the one presented by Fernandez-Tarrazo et al. Fernandez-tarrazo et al., 2006 for hydrocarbon combustion with air, where kinetic parameters are correlated to the equivalence ratio in order to better describe characteristic flame properties for premixed and non-premixed flames.

In the last decades several numerical investigations related to diffusion flames have been carried out. Burke and Schumann were the first ones to investigate the structure of diffusion flames by studying the flame jet problem. Burke and Schumann, 1928 By assuming an infinitely fast chemical reaction they managed to predict flame properties fairly accurately. In the work of

Smooke et al. Smooke et al., 1986 a numerical simulation for a two-dimensional axisymmetric laminar diffusion jet with detailed chemistry was conducted and solved with Newton-type methods. In order to obtain adequate initial estimates for this problem, the solution of the problem for an infinitely fast chemistry was solved first. This idea was used in several works such as that by Keyes and Smooke Keyes and Smooke, 1987 for a counter diffusion flame, by Smooke Smooke and Giovangigli, 1992 for a Tsuji-counterflow configuration and in the work by Dobbins et al. Dobbins and Smooke, 2010 for an axisymmetric laminar jet diffusion flame with time dependent boundary conditions. In the work of Paxion Paxion et al., 2001 unstructured multigrid solver for laminar flames with detailed chemistry is presented. A Krylov-Newton method was used for solving several flame configurations. A two-dimensional counter diffusion flame was calculated, and its results were compared with the one-dimensional self-similar solution of the equations.

The DG method has also been used for simulations of combustion, mainly within a fully compressible framework. In the work from Johnson et al. Johnson and Kercher, 2020 the compressible Navier-Stokes equations are solved using a nodal DG scheme for combustion with complex chemistry and transport parameters. An hp-adaptive method is also presented, and shown to be useful for solving the ordinary differential equations used for describing the unsteady behaviour of the system. Similarly in the work from Lv and Ihme Lv and Ihme, 2017 a DG solver for multi-component chemically reacting flows, which solves the fully compressible Navier-Stokes equation, is presented. A hybrid-flux formulation is used, where a conservative Riemann solver is used for shock treatment, and a double-flux formulation is used in smooth regions. They show its applicability for non-reacting and reacting flows, particularly for systems characterized by high Mach numbers. On the other hand, the solution of combustion problems using the DG method in an incompressible framework is a topic that has not received much attention in the literature. This fact is the motivation of the present paper.

The system of equations obtained from the discretization of highly nonlinear systems can be very difficult to solve. Fixed-point iteration schemes have been used as a linearization strategy, as done by Klein et al. Klein et al., 2016 A major drawback of this approach is the highly problem dependent choice of under-relaxation factors. A much more robust strategy is the use of Newton type methods. Shadid et al., 1997; Pawlowski et al., 2006 Here, a problem-dependent factor is not needed. There is however a trade-off, because the Jacobian matrix has to be calculated, which can be computationally expensive. This approach has been used for combustion problems in numerous works. Karaa et al. Karaa et al., 2003 studied the axisymmetric laminar jet diffusion flame and investigated the behaviour of a multi-grid solver when using different pre-conditioners with a damped Newton algorithm. Shen et al. Shen et al., 2006 investigated the use and efficiency of a Newton method coupled with the Bi-CGSTAB method for an axisymmetric laminar jet flame. They concluded that, in terms of computational cost, the steady-state solution is more efficiently obtained by directly solving the steady formulation of the equations, than by solving the transient Navier-Stokes equations until the steady state is reached.

It is well known that the Newton method shows the property of having quadratic convergence sufficiently close to the solution Deuflhard, 2011. However, if the initial solution guess is not adequate, the method converge to a solution slowly, or may not even converge at all. For some highly nonlinear problems this is a significant issue. The so-called globalized Newton methods are used to overcome this problem by effectively increasing the area of convergence of the method. A popular globalized Newton method is the Newton-Dogleg method, Pawlowski et al., 2008 which is based on a trust-region technique.

In the present work, a steady low-Mach pressure-based solver for the simulation of temperature dependent non-reactive and reactive flows using the Discontinuous Galerkin method is presented. To the best of our knowledge, this is the first time that a pressure-based solver is used together with the DG method for solving the reactive low-Mach equations using the Newton-Dogleg method in a fully coupled manner. We focus in this study on two-dimensional configurations, but the ideas presented could be extended to three-dimensional systems. The one-step combustion model presented by Fernandez-Tarrazo et al. Fernandez-tarrazo et al., 2006 is used for describing the chemical reactions. In the present work we consider only methane combustion, but the one-step model could be used for other hydrocarbons as well. We choose this chemical model to obtain physically correct results for a wide range of applications, while avoiding the use of complex chemistry models. The discrete system of equations is solved by a globalized Newton method, by means of the Dogleg approach. In addition to the Newton-Dogleg method, a homotopy strategy is presented, which was found to be useful for obtaining solutions of steady state calculations of highly nonlinear problems. In order to find appropriate initial values for Newton's method in combustion applications, the concept of flame sheet estimates (i.e. the solution for infinitely fast chemistry) is used. Several benchmark cases are presented that allow us to validate our implementation. First we solve the differentially heated cavity problem, with which we intend to validate our implementation of the low-Mach solver for non-constant density flows using the fully coupled solver. Later two flame configurations are calculated, namely the counter-diffusion flame and the chambered diffusion flame. (Matalon et al., 1980)

In the following, we consider a two-dimensional system. However, the methods shown in this work could be also used for three-dimensional problems.

They were first derived by Rehm and Baum (Rehm and Baum, 1978). A rigorous extension to combustion problems was done by Majda and Sethian (Majda and Sethian, 1985).

## 2 Governing equations

---

In this work we present the methodology used to simulate reactive fluids in the low-Mach regime using the DG method. In this chapter we intend to show the governing equations, which will be discretized in the following chapters. First, in Section 2.1 the equations for a flow in the low-Mach regime with finite reaction velocity are shown. A brief derivation of the set low-Mach equations is presented, which should also serve as a way of showing and justifying the assumptions made in this work. We restricted ourselves to a one-step chemical model, but the algorithm presented could also be used for more complex chemistry models. Subsequently, in Section 2.2 the governing equations are shown for the case of assuming an irreversible chemical model with an infinite reaction rate. This case is often called the Burke–Schumann limit. These equations are used as part of the algorithm to solve the finite reaction rate case.

---

### 2.1 The low-Mach number equations for reactive flows

---

Combustion processes can be modeled by a system of nonlinear partial differential equations, namely the balance equations for total mass, momentum, energy, and mass of individual species (usually expressed in terms of mass fractions). This system needs to be solved together with an equation of state and expressions for the transport properties as well as for the chemical reaction rates. The derivation of the governing equations for a reacting flow system can be found in the literature. (see, for example, (Kee et al., 2003), (Poinsot and Veynante, 2005)). In the following pages, the main ideas regarding the derivation of equations are presented. For a more detailed explanation, we refer to the cited works and the references therein.

---

#### 2.1.1 The reactive Navier–Stokes equations

---

Throughout this work, variables with a hat sign, e.g.  $\hat{\rho}$  represent dimensional variables, while those without it are nondimensional. We start the derivation of the low-Mach number equations with the Navier–Stokes equations, the energy equation (in its temperature form), and the species transport equations. Let us consider a reacting fluid mixture composed of  $N$  species. Let  $\hat{\mathbf{x}} = (\hat{x}, \hat{y}, \hat{z})$  and  $\hat{t}$  be the spatial vector and time. The primitive variables are the velocity field  $\hat{\mathbf{u}} = (\hat{u}, \hat{v}, \hat{w})$ , the pressure  $\hat{p}$ , the temperature  $\hat{T}$ , and the mass fractions  $Y_k$  of the  $N$  total

species. The set of governing equations to be solved is

$$\frac{\partial \hat{\rho}}{\partial \hat{t}} + \hat{\nabla} \cdot (\hat{\rho} \hat{\mathbf{u}}) = 0, \quad (2.1a)$$

$$\frac{\partial \hat{\rho} \hat{\mathbf{u}}}{\partial \hat{t}} + \hat{\nabla} \cdot (\hat{\rho} \hat{\mathbf{u}} \otimes \hat{\mathbf{u}}) = -\hat{\nabla} \hat{p} - \hat{\nabla} \cdot \hat{\tau} - \hat{\rho} \hat{\mathbf{g}}, \quad (2.1b)$$

$$\hat{\rho} \hat{c}_p \frac{\partial \hat{T}}{\partial \hat{t}} + \hat{\rho} \hat{c}_p \hat{\mathbf{u}} \cdot \hat{\nabla} \hat{T} = \frac{D\hat{p}}{Dt} - \hat{\nabla} \cdot \hat{\mathbf{q}} + \hat{\tau} : \hat{\nabla} \hat{\mathbf{u}} + \hat{\omega}_T \quad (2.1c)$$

$$\frac{\partial \hat{\rho} Y_k}{\partial \hat{t}} + \hat{\nabla} \cdot (\hat{\rho} \hat{\mathbf{u}} Y_k) = -\hat{\nabla} \cdot \hat{\mathbf{j}}_k + \hat{\omega}_k \quad (k = 1, \dots, N) \quad (2.1d)$$

This results in (in the general case)  $N + 5$  differential equations to be solved. In these equations,  $\hat{\rho}$  is the density of the mixture and  $\hat{\mathbf{g}}$  is the acceleration of gravity.  $\hat{\tau}$ ,  $\hat{\mathbf{q}}$  and  $\hat{\mathbf{j}}_k$  are the viscous tensor, the heat flux vector and the molecular mass flux vector of species  $k$ , respectively. Additionally,  $\hat{\omega}_T$  is the heat release due to combustion and  $\hat{\omega}_k$  is the reaction rate of species  $k$ . To close the system, expressions must be defined to link these variables with the primitive variables. They will be briefly shown and commented upon in the following paragraphs.

### Equation of state

Assuming that the fluid behaves ideally, the density can be calculated as

$$\hat{\rho} = \frac{\hat{p} \hat{W}_{avg}}{\mathcal{R} \hat{T}}. \quad (2.2)$$

Here,  $\hat{\mathcal{R}}$  is the universal gas constant of gases, and  $\hat{W}_{avg}$  is the average molecular weight of the fluid, defined as

$$\hat{W}_{avg} = \left( \sum_{k=1}^N \frac{Y_k}{\hat{W}_k} \right)^{-1} \quad (2.3)$$

with  $\hat{W}_k$  as the molecular weight of species  $k$ . For an ideal mixture, the specific heat capacity can be calculated as weighted averages of the specific heats of the species,

$$\hat{c}_p = \sum_{k=1}^N Y_k \hat{c}_{p,k}, \quad (2.4)$$

where  $\hat{c}_{p,k}$  corresponds to the specific heat capacity of the component  $k$ . The temperature dependence of  $\hat{c}_{p,k}$  can be accounted for by using NASA polynomials (Mcbride et al., 1993).

$$\hat{c}_{p,k} = \left( \hat{a}_1 + \hat{a}_2 \hat{T} + \hat{a}_3 \hat{T}^2 + \hat{a}_4 \hat{T}^3 + \hat{a}_5 \hat{T}^4 \right) \frac{\hat{\mathcal{R}}}{\hat{W}_k} \quad (2.5)$$

where  $\hat{a}_1, \hat{a}_2, \hat{a}_3, \hat{a}_4$  and  $\hat{a}_5$  are numerical coefficients supplied by the NASA database.

### Transport models

The viscous tensor  $\hat{\tau}$  is defined for a Newtonian fluid as

$$\hat{\tau} = -\hat{\mu} \left( \hat{\nabla} \hat{\mathbf{u}} + (\hat{\nabla} \hat{\mathbf{u}})^T \right) + \left( \frac{2}{3} \hat{\mu} - \hat{\kappa} \right) (\hat{\nabla} \cdot \hat{\mathbf{u}}) \mathbf{I} \quad (2.6)$$

Here,  $\hat{\mu}$  is the dynamic viscosity of the fluid, which is generally specific to the fluids and depends on its temperature and pressure. Furthermore,  $\hat{\kappa}$  corresponds to the bulk viscosity, which is usually negligible for fluids at low pressures (Bird et al., 1960).  $\hat{\kappa}$  will be taken equal to zero in the rest of this work.

The heat flux vector  $\hat{\mathbf{q}}$  is given by Fourier's law of heat conduction,

$$\hat{\mathbf{q}} = \hat{\lambda} \hat{\nabla} \hat{T}. \quad (2.7)$$

Here  $\hat{\lambda}$  corresponds to thermal conductivity, which, similar to the viscosity, is dependent on the particular fluid under study and its temperature and pressure.

The molecular mass flux vector  $\hat{\mathbf{j}}_k$  of species  $k$  is defined as  $\hat{\mathbf{j}}_k = \hat{\rho} \hat{\mathbf{U}}_k$ . Here  $\hat{\mathbf{U}}_k$  is the diffusion velocity of the component  $k$ . In general,  $\hat{\mathbf{U}}_k$  can be obtained by solving the Maxwell-Stefan equations.

$$\nabla X_p = \sum_{k=1}^N \frac{X_p X_k}{D_{pk}} (\mathbf{U}_k - \mathbf{U}_p) \quad p = 1, \dots, N. \quad (2.8)$$

Here  $D_{pk} = D_{kp}$  is the binary mass diffusion coefficient of species  $p$  in species  $k$ .  $X_p$  is the mole fraction of species  $k$  and is related to the mass fraction of  $k$  as  $X_k = Y_k \hat{W}/\hat{W}_k$ . The solution of the system (2.8) is often a difficult and costly task (Williams, 2000; Poinsot and Veynante, 2005), and often simplifications are made. It can be shown that for binary mixtures ( $N = 2$ ) and for mixtures containing multiple species ( $N > 2$ ) where all diffusion coefficients are equal, the system (2.8) reduces exactly to the well-known Fick's law.

$$\hat{\mathbf{j}}_k = -\hat{\rho} \hat{D}_k \nabla Y_k \quad (2.9)$$

This expression is only exact in the cases mentioned above. For a system where the heat capacities of each species are different, this expression is inconsistent. The variable  $\hat{D}_k$  corresponds in this case to the diffusion coefficient of species  $k$  in the mixture. An issue regarding the global mass conservation can be pointed out here. Recall that by definition the sum of the mass fractions must always be one ( $\sum_k^N Y_k = 1$ ). This is only true for the solution of Equation (2.1) if exact expressions for the diffusion velocities are used (Poinsot and Veynante, 2005). If some inexact expression is used (as for example Fick's law), the constraint for the sum of the mass fractions will not be fulfilled. This problem can be surpassed by solving the global mass conservation (continuity) equation Equation (2.1a) and only the equations for the first  $N - 1$  species Equation (2.1d). Therefore, all inconsistencies that originated from not using an exact species diffusion model are absorbed by  $Y_N$ . As pointed out in Poinsot and Veynante, 2005, this simplification should only be used if all  $N - 1$  species are strongly diluted in species  $N$ , such as the case of a flame in air, where the mass fraction of nitrogen is large. It can also be noted that this approach reduces in one the number of differential equations needed to be solved.

The temperature dependence of viscosity can be modeled by Sutherland's law (Sutherland, 1893)

$$\hat{\mu}(\hat{T}) = \hat{\mu}_{\text{suth}} \left( \frac{\hat{T}}{\hat{T}_{\text{suth}}} \right)^{1.5} \frac{\hat{T}_{\text{suth}} + \hat{S}}{\hat{T} + \hat{S}}. \quad (2.10)$$

Here  $\hat{\mu}_{\text{suth}}$  is the viscosity evaluated at a reference temperature  $\hat{T}_{\text{suth}}$ , and  $\hat{S}$  is a material dependent parameter. In all calculations in this work the value of  $\hat{S}$  for air is used,  $\hat{S} = 110.5$  K. Expressions for determining the thermal conductivity and diffusion coefficients as function of temperature can be obtained using similar expressions, as will be shown later in Section 2.1.2

---

## Chemical model

---

Consider a system composed of  $N$  species where  $M$  chemical reactions take place. Chemical reactions can be written in generalized form as follows.

$$\sum_{k=1}^N \nu'_{kj} \mathcal{M}_k \rightleftharpoons \sum_{k=1}^N \nu''_{kj} \mathcal{M}_k \quad \text{for } j = 1, \dots, M \quad (2.11)$$

where  $\nu'_{jk}$  and  $\nu''_{jk}$  are the molar stoichiometric coefficients of species  $k$  in the chemical reaction  $j$ , and  $\mathcal{M}_j$  represents the chemical component  $k$ .

The reaction rate of species  $k$  is  $\hat{\omega}_k$ , which accounts for the total amount of species  $k$  that appear or disappear due to  $M$  chemical reactions (c.f. Equations (2.11)). Its given by

$$\hat{\omega}_k = \hat{W}_k \sum_{j=1}^M \nu_{jk} \hat{\mathcal{Q}}_j. \quad (2.12)$$

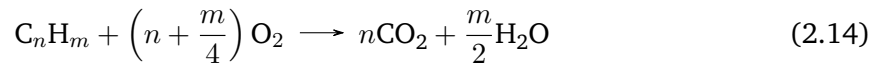
Here  $\nu_{kj} = \nu''_{kj} - \nu'_{kj}$ , and  $\mathcal{Q}_j$  is the rate of progress of the reaction  $j$ . They are usually modeled using Arrhenius-type expressions, as will be shown later.

The heat release  $\hat{\omega}_T$  that appears in the energy equation is related to the reaction rates according to

$$\hat{\omega}_T = - \sum_{k=1}^N \hat{h}_k \hat{\omega}_k = - \sum_{k=1}^N \Delta \hat{h}_k^0 \hat{\omega}_k - \sum_{k=1}^N \hat{h}_{ks} \hat{\omega}_k \quad (2.13)$$

Here, the specific enthalpy of  $k$ -th species  $\hat{h}_k$  is written in terms of its formation enthalpy  $\hat{h}_k^0$  and a sensible enthalpy  $\hat{h}_{ks} = \int_0^{\hat{T}} \hat{c}_{p,k} d\hat{T}$ . The second term on the right-hand side of Equation (2.13) is usually small and is exactly zero for a mixture where all the heat capacities of each component are equal (Poinsot and Veynante, 2005). It will be neglected in the rest of the analysis.

In this work, we use the one-step kinetic model for the combustion of hydrocarbons presented in Fernandez-tarrazo et al., 2006. The chemical reaction is represented by a single ( $M = 1$ ) exothermic global irreversible expression as



The rate of progress of the global reaction is modeled by an Arrhenius-type expression

$$\hat{\mathcal{Q}} = \hat{B} e^{-\hat{T}_a/\hat{T}} \left( \frac{\hat{\rho} Y_F}{\hat{W}_F} \right)^a \left( \frac{\hat{\rho} Y_O}{\hat{W}_O} \right)^b. \quad (2.15)$$

Here, the subscripts  $F$  and  $O$  refer to fuel and oxidizer, respectively. The parameter  $\hat{B}$  corresponds to the pre-exponential factor,  $\hat{T}_a$  is the activation temperature, and  $a$  and  $b$  are reaction orders. For a one-step reaction model, the reaction rate of the  $k$ -th component (Equation (2.12)) is

$$\hat{\omega}_k = \nu_k \hat{W}_k \hat{\mathcal{Q}}. \quad (2.16)$$

$\hat{B}$ (cm <sup>3</sup> /(mol s))	$\hat{T}_{a0}$ (K)	$\hat{Q}_0$ (MJ kmol <sup>-1</sup> )	$a$	$b$
$6.9 \times 10^{14}$	15 900	802.4	1	1

**Table 2.1:** Base parameters used in the one-step combustion model by Fernandez-tarrazo et al., 2006

With this definition, the heat release  $\hat{\omega}_T$  (Equation (2.13)) is

$$\hat{\omega}_T = -\hat{W}_F \hat{\omega}_F \hat{Q}^m = -\hat{\omega}_F \hat{Q}. \quad (2.17)$$

Here is  $\hat{Q}^m$  the molar heat of reaction of the one-step reaction and  $\hat{Q}$  is the mass heat of reaction.  $\hat{W}_F$  and  $\hat{\omega}_F$  are the molar mass of the fuel species and the reaction rate of the fuel species respectively.

Within the model from (Fernandez-tarrazo et al., 2006), several parameters are adjusted to represent characteristic features of premixed flames and diffusion flames. The parameters  $\hat{T}_a$  and  $\hat{Q}$  are defined as functions of the local equivalence ratio  $\phi$ , which is, in turn, defined in terms of the local mass fractions of fuel  $Y_F$  and oxidizer  $Y_O$  as

$$\phi = \frac{s Y_F^0}{Y_O^0} \frac{s Y_F - Y_O + Y_O^0}{s(Y_F^0 - Y_F) + Y_O}, \quad (2.18)$$

where  $Y_F^0$  and  $Y_O^0$  are the mass fractions of the fuel and oxidizer flows in their corresponding feed streams, and  $s$  is the mass stoichiometric ratio, defined as  $s = \nu_O \hat{W}_O / \nu_F \hat{W}_F$ . The activation energy and molar heat release depend on  $\phi$  as

$$\hat{T}_a(\phi) = \begin{cases} (1 + 8.250(\phi - 0.64)^2) \hat{T}_{a0} & \text{if } \phi \leq 0.64, \\ \hat{T}_{a0} & \text{if } 0.64 \leq \phi \leq 1.07, \\ (1 + 4.443(\phi - 1.07)^2) \hat{T}_{a0} & \text{if } \phi \geq 1.07, \end{cases} \quad (2.19)$$

$$\hat{Q}(\phi) = \begin{cases} \hat{Q}_0 & \text{if } \phi \leq 1 \\ (1 - \alpha(\phi - 1)) \hat{Q}_0 & \text{if } \phi > 1, \end{cases} \quad (2.20)$$

The parameter  $\alpha$  is a constant that depends on the hydrocarbon being considered. In particular  $\alpha = 0.21$  for the combustion of methane.

## 2.1.2 The unsteady non-dimensional low-Mach equations

In the present work, we use the low-Mach number equation approximation of the governing equations. The derivation of the equations can be found in (**mullerLowMachNumberAsymptoticsNavierStokes** Rehm and Baum, 1978; Majda and Sethian, 1985). We refer to these references for a detailed explanation on how the set of equations is derived. In the following, we restrict ourselves to show and comment on the main consequences of the low-Mach limit.

The low-Mach number limit approximation of the governing equations is used for flows where the Mach number (defined as  $\text{Ma} = \hat{u}_{\text{ref}}/\hat{c}$ , where  $\hat{u}_{\text{ref}}$  is a characteristic flow velocity and  $\hat{c}$  the speed of sound) is small, which is usually the case in typical laminar combustion systems. (Dobbins and Smooke, 2010). The low-Mach equations are obtained by using standard

asymptotic methods. One of the main results of the analysis is that for flows with a small Mach number, the pressure can be decomposed as

$$\hat{p}(\hat{\mathbf{x}}, \hat{t}) = \hat{p}_0(\hat{t}) + \hat{p}_2(\hat{\mathbf{x}}, \hat{t}). \quad (2.21)$$

The spatially uniform term  $\hat{p}_0(\hat{t})$  is called thermodynamic pressure, and only appears in the equation of state. It is constant in space, but can change in time. For an open system, the thermodynamic pressure is constant and equal to the ambient pressure, while for a closed system (e.g. a system completely bounded by walls) it changes in order to ensure mass conservation. On the other hand, the perturbational term  $\hat{p}_2(\hat{\mathbf{x}}, \hat{t})$  appears only in the momentum equations and plays a role similar to that of the pressure in the classical incompressible formulation. This perturbational term satisfies  $\hat{p}_2/\hat{p} \sim \mathcal{O}(\text{Ma})^2$ , (Dobbins and Smooke, 2010; Nonaka et al., 2018) showing that under these assumptions, the equation of state is satisfied only to  $\mathcal{O}(\text{Ma}^2)$  (cf. Equation (2.2))

Effectively, the low-Mach limit of the Navier-Stokes equations allows for the calculation of systems where big density variations due to temperature differences are present, thus not restricting ourselves to approximations such as the Boussinesq approximation for buoyancy-driven flow. In addition, this approximation truncates the mechanism of pressure wave propagation which is a natural feature of the compressible Navier-Stokes equations. In doing this, we are no longer restricted to choosing small timesteps to be able to resolve wave phenomena, and the maximum allowed timestep is greatly increased. From now on we will drop the sub-index of the hydrodynamic pressure  $\hat{p}_2$  and we will refer to it simply as  $\hat{p}$ , further emphasizing the similarity in its role to the pressure of the incompressible formula.

In this work we use a non-dimensional formulation of the governing equations. We define the non-dimensional quantities.

$$\begin{aligned} \rho &= \frac{\hat{\rho}}{\hat{\rho}_{\text{ref}}}, & p &= \frac{\hat{p}}{\hat{p}_{\text{ref}}}, & \mathbf{u} &= \frac{\hat{\mathbf{u}}}{\hat{u}_{\text{ref}}}, & T &= \frac{\hat{T}}{\hat{T}_{\text{ref}}}, & c_p &= \frac{\hat{c}_p}{\hat{c}_{p,\text{ref}}}, & W_k &= \frac{\hat{W}_k}{\hat{W}_{\text{ref}}} \\ \mu &= \frac{\hat{\mu}}{\hat{\mu}_{\text{ref}}}, & D_k &= \frac{\hat{D}_k}{\hat{D}_{k,\text{ref}}}, & k &= \frac{\hat{k}}{\hat{k}_{\text{ref}}}, & \nabla &= \frac{\hat{\nabla}}{\hat{L}_{\text{ref}}}, & t &= \frac{\hat{t}}{\hat{t}_{\text{ref}}}, & \mathbf{g} &= \frac{\hat{\mathbf{g}}}{\hat{g}_{\text{ref}}}, & Q &= \frac{\hat{Q}}{\hat{Q}_0} \end{aligned}$$

Here  $\hat{u}_{\text{ref}}$ ,  $\hat{L}_{\text{ref}}$ ,  $\hat{p}_{\text{ref}}$ ,  $\hat{t}_{\text{ref}}$ , and  $\hat{T}_{\text{ref}}$  are the reference velocity, length, pressure, time, and temperature, respectively, and are equal to some characteristic value for the particular configuration studied. Furthermore,  $\hat{g}_{\text{ref}}$  is the magnitude of the gravitational acceleration and  $\hat{W}_{\text{ref}}$  is the reference molecular weight. The reference transport properties  $\hat{\mu}_{\text{ref}}$ ,  $\hat{k}_{\text{ref}}$ ,  $\hat{D}_{k,\text{ref}}$  and the reference heat capacity of the mixture and  $\hat{c}_{p,\text{ref}}$  are evaluated at the reference temperature  $\hat{T}_{\text{ref}}$ . Similarly, the reference density must satisfy the equation of state, thus  $\hat{\rho}_{\text{ref}} = \hat{p}_{\text{ref}} / (\hat{R} \hat{T}_{\text{ref}} \hat{W}_{\text{ref}})$ . By introducing these definitions into the governing equations (Equations (2.1a) to (2.1d)) the reactive set of non-dimensional low-Mach number equations is obtained. The system of differential equations to be solved reads as follows.

$$\frac{\partial \rho}{\partial t} + \nabla \cdot (\rho \mathbf{u}) = 0, \quad (2.22a)$$

$$\frac{\partial \rho \mathbf{u}}{\partial t} + \nabla \cdot (\rho \mathbf{u} \otimes \mathbf{u}) = -\nabla p + \frac{1}{\text{Re}} \nabla \cdot \mu \left( \nabla \mathbf{u} + \nabla \mathbf{u}^T - \frac{2}{3} (\nabla \cdot \mathbf{u}) \mathbf{I} \right) - \frac{1}{\text{Fr}^2} \rho \mathbf{g}, \quad (2.22b)$$

$$\frac{\partial \rho T}{\partial t} + \nabla \cdot (\rho \mathbf{u} T) = \frac{1}{\text{Re} \text{Pr}} \nabla \cdot \left( \frac{k}{c_p} \nabla T \right) + \text{H Da} \frac{Q \mathcal{Q}}{c_p}, \quad (2.22c)$$

$$\frac{\partial \rho Y_k}{\partial t} + \nabla \cdot (\rho \mathbf{u} Y_k) = \frac{1}{\text{Re} \text{Pr} \text{Le}_k} \nabla \cdot (\rho D \nabla Y_k) + \text{Da} \nu_k W_k \mathcal{Q}. \quad (k = 1, \dots, N-1) \quad (2.22d)$$

Note that we assumed that the spatial gradients of the mixture heat capacity are small, allowing us to introduce it in the derivative of the diffusive term of Equation (2.22c). Furthermore, using the fact that the sum of the mass fractions must always be one, the mass fraction of the last species  $N$  can be calculated with

$$Y_N = 1 - \sum_{k=1}^{N-1} Y_k. \quad (2.23)$$

The  $N$ -th component mass fraction  $Y_N$  is calculated using Equation (2.23). This system is solved for the primitive variables velocity  $\mathbf{u} = (u_x, u_y)$ , pressure  $p$ , temperature  $T$  and mass fractions  $\mathbf{Y} = (Y_1, \dots, Y_N)$ . We note that the form of the low-Mach equations is very similar to the Navier-Stokes equations. The greatest difference is in the decomposition of the pressure, as mentioned above. This similarity is beneficial, as it allows the use of similar techniques to solve the PDE system to those used for the completely incompressible case (Keshtiban et al., 2003).

Six non-dimensional factors arise from the non-dimensionalization process:

$$\begin{aligned} \text{Re} &= \frac{\hat{\rho}_{\text{ref}} \hat{u}_{\text{ref}} \hat{L}_{\text{ref}}}{\hat{\mu}_{\text{ref}}}, & \text{Fr} &= \frac{\hat{u}_{\text{ref}}}{\sqrt{\hat{g}_{\text{ref}} \hat{L}_{\text{ref}}}}, & \text{Pr} &= \frac{\hat{c}_{p,\text{ref}} \hat{\mu}_{\text{ref}}}{\hat{k}_{\text{ref}}}, \\ \text{Le}_k &= \frac{\hat{k}_{\text{ref}}}{\hat{\rho}_{\text{ref}} \hat{D}_{k,\text{ref}} \hat{c}_{p,\text{ref}}}, & \text{Da} &= \frac{\hat{B} \hat{L}_{\text{ref}} \hat{\rho}_{\text{ref}}}{\hat{M}_{\text{ref}} \hat{u}_{\text{ref}}}, & \text{H} &= \frac{\hat{Q}_0}{\hat{c}_{p,\text{ref}} \hat{T}_{\text{ref}}} \end{aligned}$$

The first three equations define the Reynolds, Froude and Prandtl number respectively.  $\text{Le}_k$  is the Lewis number of species  $k$ . Finally Da and H are the Damköhler number and the non-dimensional heat release respectively. The non-dimensional progress of the global reaction reads as follows.

$$\mathcal{Q}(T, \mathbf{Y}) = \left( \frac{\rho Y_F}{M_F} \right) \left( \frac{\rho Y_O}{M_O} \right) \exp \left( \frac{-T_a}{T} \right), \quad (2.24)$$

where  $T_a = \hat{T}_a / \hat{T}_{\text{ref}}$ . Furthermore, the non-dimensional heat release is

$$Q(\phi) = \begin{cases} 1 & \text{if } \phi \leq 1 \\ (1 - \alpha(\phi - 1)) & \text{if } \phi > 1, \end{cases} \quad (2.25)$$

with  $\phi$  evaluated according to Equation (2.18). In the low-Mach limit, the ideal gas equation depends on the thermodynamic pressure, temperature and mass fractions. It reads in its non-dimensional form

$$\rho(p_0, T, \mathbf{Y}) = \frac{p_0}{T \sum_{k=1}^N \frac{Y_k}{W_k}}. \quad (2.26)$$

As mentioned above, the thermodynamic pressure of a closed system is a parameter that has to be determined (for an open system is equal to the atmospheric pressure). Defining the initial mass of the fluid inside the closed system as  $m_0$ , and by integrating Equation (2.26) on the whole domain  $\Omega$ , one obtains

$$p_0(T, \mathbf{Y}) = \frac{m_0}{\int_{\Omega} \frac{W_{\text{avg}}}{T} dV}, \quad (2.27)$$

TODO: porque tengo escrito aca la cosa con Wavg??? Similarly, the non-dimensional specific heat capacity of the mixture  $c_p$  is calculated as

$$c_p(T, \mathbf{Y}) = \sum_{k=1}^N Y_k c_{p,\alpha}(T), \quad (2.28)$$

and the non-dimensional viscosity as

$$\mu(T) = T^{\frac{3}{2}} \frac{1 + \hat{S}}{\hat{T}_{\text{ref}} T + \hat{S}}. \quad (2.29)$$

As mentioned before, the model for the transport parameters can be simplified by assuming constant values for the Prandtl and Lewis numbers. (Smoke and Giovangigli, 1991) and we can write  $\mu(T) = k/c_p(T) = \rho D_k(T)$ .

## 2.2 The flame sheet approximation

Here we introduce the concept of the flame sheet approximation, which is used in our solution algorithm for solving the finite reaction rate system given by Equations (2.1a), (2.1b), (2.22c) and (2.22d). We follow the ideas proposed in the work from Keyes and Smooke, 1987. Assuming that all species have the same constant heat capacity  $c_p$  and mass diffusion coefficient  $D_k = D$ , that the Lewis number is unity for all species, and that combustion can be described by a single-step chemical reaction, it is possible to obtain an equation for a scalar without source terms, taking a linear combination of the energy Equation (2.22c) and mass fraction Equation (2.22d). A commonly used scalar is the mixture fraction  $z$ , which per definition is equal to unity in the fuel feed stream, and equal to zero in the oxidizer feed stream. Thus, the system of Equations (2.1a), (2.1b), (2.22c) and (2.22d) can be simplified to solving the low-Mach Navier-Stokes equations together with an equation for the passive scalar  $z$ :

$$\frac{\partial \rho}{\partial t} + \nabla \cdot (\rho \mathbf{u}) = 0, \quad (2.30a)$$

$$\frac{\partial \rho \mathbf{u}}{\partial t} + \nabla \cdot (\rho \mathbf{u} \otimes \mathbf{u}) = -\nabla p + \frac{1}{\text{Re}} \nabla \cdot \mu \left( \nabla \mathbf{u} + \nabla \mathbf{u}^T - \frac{2}{3} (\nabla \cdot \mathbf{u}) \mathbf{I} \right) - \frac{1}{\text{Fr}^2} \rho \mathbf{g}, \quad (2.30b)$$

$$\frac{\partial \rho z}{\partial t} + \nabla \cdot (\rho \mathbf{u} z) = \frac{1}{\text{Re} \text{Pr}} \nabla \cdot (\rho D \nabla z), \quad (2.30c)$$

which are solved together with the equation of state and expressions for the transport parameters. Note that the system is not closed, because  $\rho$ ,  $\mu$  and  $\rho D$  are still functions of temperature and mass fractions. These fields can be related to the mixture fraction using the concept of the Burke-Schumann flame structure. (Burke and Schumann, 1928) In the case of an infinitely fast chemical reaction, fuel and oxidizer cannot co-exist. On one side of this sheet only oxidizer is found, and on the other side only fuel. The exact position of the flame sheet can be determined by finding the location of points where both reactant mass fractions  $Y_F$  and  $Y_O$  meet in stoichiometric proportions, that is, the points where the mixture fraction  $z = z_{st}$ , with

$$z_{st} = \frac{Y_O^0}{Y_O^0 + s Y_F^0}, \quad (2.31)$$

where  $Y_O^0$  is the mass fraction of oxidizer in the oxidizer inlet stream, and  $Y_F^0$  is the mass fraction of fuel in the fuel inlet stream. The Burke-Schumann solution provides analytical expressions for temperature and mass fraction fields on either side of the flame sheet as function of the mixture fraction  $z$  (see for example the textbook from Poinsot and Veynante, 2005 or the work from Keyes and Smooke, 1987).

$$T(z) = \begin{cases} zT_F^0 + (1-z)T_O^0 + \frac{QY_F^0}{c_p}z_{st}\frac{1-z}{1-z_{st}} & \text{if } z \geq z_{st} \\ zT_F^0 + (1-z)T_O^0 + \frac{QY_F^0}{c_p}z & \text{if } z < z_{st} \end{cases} \quad (2.32)$$

The mass fraction field of fuel and oxidizer species at either side of the flame are given by:

$$Y_F(z) = \begin{cases} Y_F^0\frac{z - z_{st}}{1 - z_{st}} & \text{if } z \geq z_{st} \\ 0 & \text{if } z < z_{st} \end{cases} \quad (2.33)$$

$$Y_O(z) = \begin{cases} 0 & \text{if } z \geq z_{st} \\ Y_O^0\left(1 - \frac{z}{z_{st}}\right) & \text{if } z < z_{st} \end{cases} \quad (2.34)$$

and finally, the mass fraction field of product species  $P$  is:

$$Y_P(z) = \begin{cases} Y_O^0\frac{W_P\nu_P}{W_O\nu_O}(1-z) & \text{if } z \geq z_{st} \\ Y_F^0\frac{W_P\nu_P}{W_F\nu_F}z & \text{if } z < z_{st} \end{cases} \quad (2.35)$$

Once the mixture fraction field  $z$  is obtained, the temperature and mass fraction fields are uniquely defined by Equations (2.32) to (2.35), which are used to evaluate the density and the transport properties. This coupling between variables and the associated nonlinear system leads to the need for an iterative solution scheme.

The main idea of introducing this additional system (Equations (2.30a) to (2.30c)) is to find an approximate solution to the system where a finite reaction-rate is used (Equations (2.22a) to (2.22d)). In Figure 2.1 temperature and fuel mass fraction fields across the center-line of a counterflow flame configuration is shown. Clearly, both solutions are very similar, differing only in the area near the flame. However, this similarity is only valid under the assumptions made to derive Equation (2.30c). In the case that the Lewis number is not equal to one, or that the heat capacities are not equal for each species, the finite-rate solution will differ slightly from that obtained with the infinite-reaction rate.

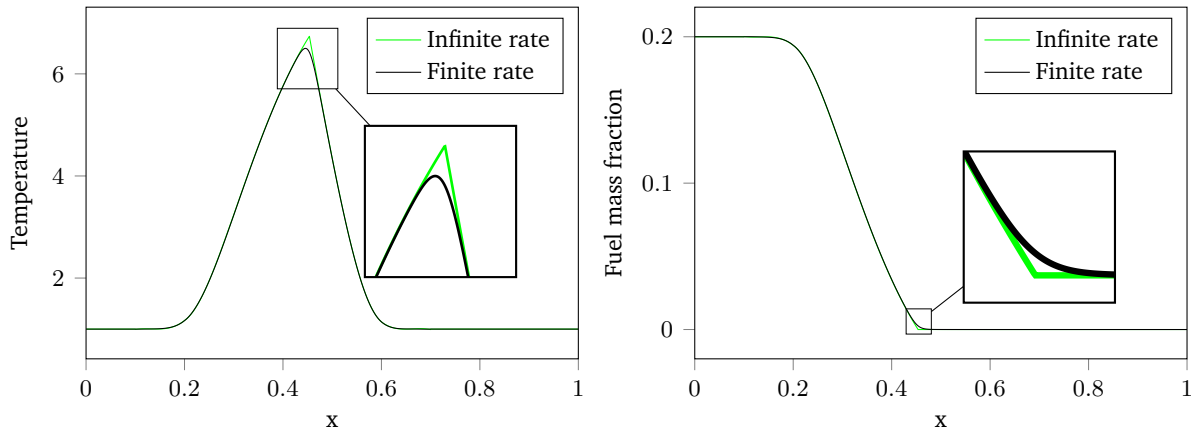


**Figure 2.1:** Temperature and fuel mass fraction profiles calculated in the center-line of a counter-flow flame configuration using finite chemistry (black) and the flame sheet approximation (green).

## 2.3 Boundary conditions

The following boundary conditions are imposed for the resolution of the finite reaction rate system (Equations (2.22a) to (2.22d)) and for the flame sheet problem (Equations (2.30a) to (2.30c)).

$$\Gamma_D : \quad \mathbf{u} = \mathbf{u}_D, \quad T = T_D, \quad Y_k = Y_{k,D}, \quad z = z_D, \quad (2.36a)$$

$$\Gamma_{DW} : \quad \mathbf{u} = \mathbf{u}_D, \quad \nabla T \cdot \mathbf{n}_{\partial\Omega} = 0, \quad \nabla Y_k \cdot \mathbf{n}_{\partial\Omega} = 0, \quad \nabla z \cdot \mathbf{n}_{\partial\Omega} = 0, \quad (2.36b)$$

$$\begin{aligned} \Gamma_N : \quad & \left( -p\mathbf{I} + \left( \frac{\mu}{Re} (\nabla \mathbf{u} + (\nabla \mathbf{u})^T) - \frac{2}{3}\mu(\nabla \cdot \mathbf{u})\mathbf{I} \right) \right) \cdot \mathbf{n}_{\partial\Omega} = 0, \\ & \nabla T \cdot \mathbf{n}_{\partial\Omega} = 0, \quad \nabla Y_k \cdot \mathbf{n}_{\partial\Omega} = 0, \quad \nabla z \cdot \mathbf{n}_{\partial\Omega} = 0, \end{aligned} \quad (2.36c)$$

$$\begin{aligned} \Gamma_{ND} : \quad & \left( -p\mathbf{I} + \left( \frac{\mu}{Re} (\nabla \mathbf{u} + (\nabla \mathbf{u})^T) - \frac{2}{3}\mu(\nabla \cdot \mathbf{u})\mathbf{I} \right) \right) \cdot \mathbf{n}_{\partial\Omega} = 0, \\ & T = T_D, \quad Y_k = Y_{k,D}, \quad z = z_D \end{aligned} \quad (2.36d)$$

$$\Gamma_P : \quad \mathbf{u}(\mathbf{x}) = \mathbf{u}(\mathbf{x}'), \quad T(\mathbf{x}) = T(\mathbf{x}'), \quad Y_k(\mathbf{x}) = Y_k(\mathbf{x}'), \quad z(\mathbf{x}) = z(\mathbf{x}'), \quad (2.36e)$$

where  $k$  denotes the index from mass fractions  $k = (1, \dots, N - 1)$ . The boundary  $\Gamma_D$  represents conditions for inlets and walls, with velocity, temperature, mass fractions and mixture fraction defined as Dirichlet boundary conditions. Boundaries  $\Gamma_{DW}$  are used to represent adiabatic walls, where velocity is given as a Dirichlet boundary condition, but with the gradients perpendicular to the wall of the transported scalars set to zero. The boundary  $\Gamma_N$  represent an outflow of the domain with homogeneous Neumann condition for all scalars. The boundary  $\Gamma_{ND}$  also represents an outlet boundary condition, but with Dirichlet boundary conditions for the scalars. Finally the boundaries  $\Gamma_P$  are periodic boundaries, where  $\mathbf{x}$  and  $\mathbf{x}'$  are periodic pairs in the domain.

# 3 Numerical methods

---

## 3.1 The Discontinuous Galerkin method

---

### 3.1.1 Spatial discretization

---

We start by introducing some standard definitions and notation in the context of DG methods: Kummer, 2017 Kikker et al., 2020 We define a computational domain  $\Omega \subset \mathbb{R}^2$  with a polygonal and simply connected boundary  $\partial\Omega$ . Our numerical grid is then defined by the set of non-overlapping elements  $\mathcal{K} = \{K_1, \dots, K_N\}$  with a characteristic mesh size  $h$ , so that  $\Omega$  is the union of all elements, i.e.  $\Omega = \bigcup_{i=1}^N K_i$ . We define  $\Gamma = \bigcup_j \partial K_j$  as the union of all edges (internal edges and boundary edges) and  $\Gamma_I = \Gamma \setminus \partial\Omega$  as the union of all interior edges. For each edge of  $\Gamma$  a normal field  $\mathbf{n}_\Gamma$  is defined. Particularly on  $\partial\Omega$  is defined as an outer normal and  $\mathbf{n}_\Gamma = \mathbf{n}_{\partial\Omega}$ . For each field  $\mathbf{u} \in C^0(\Omega \setminus \Gamma_I)$  we define  $\mathbf{u}^-$  and  $\mathbf{u}^+$ , which describe the information in the interior and exterior sides of the cell:

$$\mathbf{u}^- = \lim_{\xi \searrow 0} \mathbf{u}(\mathbf{x} - \xi \mathbf{n}_\Gamma) \quad \text{for } \mathbf{x} \in \Gamma \quad (3.1)$$

$$\mathbf{u}^+ = \lim_{\xi \searrow 0} \mathbf{u}(\mathbf{x} + \xi \mathbf{n}_\Gamma) \quad \text{for } \mathbf{x} \in \Gamma_I \quad (3.2)$$

The jump and mean values of  $\mathbf{u}$  on inner edges  $\Gamma_I$  are defined as:

$$[\![\mathbf{u}]\!] = \mathbf{u}^+ - \mathbf{u}^- \quad (3.3)$$

$$\{\mathbf{u}\} = \frac{1}{2} (\mathbf{u}^- + \mathbf{u}^+) . \quad (3.4)$$

while the jump and mean values on boundary edges  $\partial\Omega$  are:

$$[\![\mathbf{u}]\!] = \mathbf{u}^- \quad (3.5)$$

$$\{\mathbf{u}\} = \mathbf{u}^- . \quad (3.6)$$

We define the broken polynomial space of total degree  $k$  as

$$\mathbb{P}_k(\mathcal{K}_h) = \{f \in L^2(\Omega) ; \forall K \in \mathcal{K} : f|_K \text{ is polynomial and } \deg(f|_K) \leq k\}. \quad (3.7)$$

Additionally for  $u \in \mathcal{C}^1(\Omega \setminus \Gamma)$  the broken gradient  $\nabla_h u$  is defined as:

$$\nabla_h u = \begin{cases} 0 & \text{on } \Gamma \\ \nabla u & \text{elsewhere} \end{cases} \quad (3.8)$$

The broken divergence  $\nabla_h \cdot u$  is defined analogously. Finally, we define the function space for test and trial functions for  $D_v$  dependent variables:

$$\mathbb{V}_\mathbf{k} = \prod_{i=1}^{D_v} \mathbb{P}_{k_i}(K_h) \quad (3.9)$$

where  $\mathbf{k} = (k_1, \dots, k_{D_v})$ .

### 3.1.2 Discretization for a DG Method

As an introductory example, following **hesthaven\_nodal\_2008**, we are considering the discretization of a general conservation law with a non-linear flux function  $\mathbf{f}(\psi)$  for a scalar quantity  $\psi = \psi(\mathbf{x}, t)$  in  $\Omega$  and suitable Dirichlet boundary condition on  $\partial\Omega = \partial\Omega_D$  and a compatible initial condition  $\psi_0$ . The problem statement reads

$$\frac{\partial\psi}{\partial t} + \nabla \cdot \mathbf{f}(\psi) = 0, \quad \mathbf{x} \in \Omega, \quad (3.10a)$$

$$\psi = \psi_D, \quad \mathbf{x} \in \partial\Omega_D, \quad (3.10b)$$

$$\psi(\mathbf{x}, 0) = \psi_0(\mathbf{x}), \quad \mathbf{x} \in \Omega. \quad (3.10c)$$

The goal is to find an approximate solution  $\tilde{\psi} = \tilde{\psi}(\mathbf{x}, t)$  to  $\psi$  that fulfils the problem (3.10). Therefore, the problem domain  $\Omega$  is discretized by a numerical mesh  $\mathfrak{K}_h$  and for each numerical cell  $K_j$  we introduce the approximation by a local polynomial basis  $\phi_j = (\phi_{j,l})_{l=1,\dots,N_k} \in \mathbb{P}_k(\{K_j\})$  with a cell-local support  $\text{supp}(\phi_j) = \bar{K}_j$  as

$$\psi_j(\mathbf{x}, t) = \sum_{l=1}^{N_k} \tilde{\psi}_{j,l}(t) \phi_{j,l}(\mathbf{x}) = \tilde{\psi}_j(t) \cdot \phi_j(\mathbf{x}), \quad \mathbf{x} \in K_j, \quad (3.11)$$

where the coefficients  $\tilde{\psi}_j = (\tilde{\psi}_{j,l})_{l=1,\dots,N_k}$  denote the unknowns or degrees of freedom (DOF) of the local solution in cell  $K_j$ . In this work a modal polynomial basis is used, which fulfils the orthogonality condition

$$\int_{K_j} \phi_{j,m} \phi_{j,n} \, dV = \delta_{mn} \quad (3.12)$$

with the Kronecker delta  $\delta_{mn}$ . Inserting the local approximation (3.11) into the conservation law (3.10a) results in a cell-wise residual

$$R_j(\mathbf{x}, t) = \frac{\partial\psi_j}{\partial t} + \nabla \cdot \mathbf{f}(\psi_j), \quad \mathbf{x} \in K_j. \quad (3.13)$$

For a Galerkin method, the residual (3.13) is minimized with respect to the same space as the ansatz functions, i.e.  $\mathbb{P}_k(\{K_j\})$ . Thus, we demand for the test functions  $\vartheta_{j,l} = \phi_{j,l}$  in each cell  $K_j \in \mathfrak{K}_h$  that

$$\int_{K_j} R_j \vartheta_{j,l} \, dV = \int_{K_j} \frac{\partial\psi_j}{\partial t} \phi_{j,l} + \nabla \cdot \mathbf{f}(\psi_j) \phi_{j,l} \, dV \stackrel{!}{=} 0, \quad \forall \phi_{j,l}. \quad (3.14)$$

So, for each cell we end up with a linear system of  $N_k$  equations. However so far, no approximate global solution  $\psi \in \Omega$  can be regained from the minimization in (3.14). The global solution is assumed to be a piecewise polynomial approximation

$$\psi(\mathbf{x}, t) \approx \psi(\mathbf{x}, t) = \bigoplus_{j=1}^J \psi_j(\mathbf{x}, t) = \sum_{j=1}^J \sum_{l=1}^{N_k} \tilde{\psi}_{j,l}(t) \phi_{j,l}(\mathbf{x}) \in \mathbb{P}_k(\mathfrak{K}_h) \quad (3.15)$$

defined as the direct sum of the  $J$  local solutions  $\psi_j$  in (3.11). Here,  $\tilde{\psi}_{j,l}$ , with  $j = 1, \dots, J$  and  $l = 1, \dots, N_k$ , denote the total DOF, with  $N = J \cdot N_k$ , of the global approximate solution  $\psi$ . In

order to formulate a global DG method, the spatial term on the right-hand side of equation (3.14) is rewritten in terms of boundary edge integrals  $\forall K_j \in \mathcal{K}_h$  using partial integration

$$\int_{K_j} \frac{\partial \psi_j}{\partial t} \phi_{j,l} \, dV - \int_{K_j} \mathbf{f}(\psi_j) \cdot \nabla_h \phi_{j,l} \, dV + \oint_{\partial K_j} (\mathbf{f}(\psi_j) \cdot \mathbf{n}_j) \phi_{j,l} \, dS = 0, \quad \forall \phi_{j,l}, \quad (3.16)$$

where  $\mathbf{n}_j$  represents the local outward pointing normal for cell  $K_j$ . Note that on the internal edges  $\Gamma_{\text{int}}$  the value of  $\mathbf{f}(\psi_j)$  is multiply defined. Therefore, a numerical flux  $\hat{F}$  is introduced

$$\hat{F}(\psi_j^{\text{in}}, \psi_j^{\text{out}}, \mathbf{n}_\Gamma) \approx \mathbf{f}(\psi_j) \cdot \mathbf{n}_j, \quad (3.17)$$

that uniquely defines the resulting value of both neighbouring values, i.e.  $\psi_j^{\text{in}}$  and  $\psi_j^{\text{out}}$  at internal edges  $\Gamma_{\text{int}}$ . Summing over all cells  $K_j$ , the global minimization problem for  $\psi(\mathbf{x}, t), \mathbf{x} \in \Omega$  reads: Find  $\psi \in \mathbb{P}_k(\mathcal{K}_h)$ , such that  $\forall \vartheta = \phi \in \mathbb{P}_k(\mathcal{K}_h)$

$$\int_{\Omega} \frac{\partial \psi}{\partial t} \phi \, dV - \int_{\Omega} \mathbf{f}(\psi) \cdot \nabla_h \phi \, dV + \oint_{\Gamma} \hat{F}(\psi^{\text{in}}, \psi^{\text{out}}, \mathbf{n}_\Gamma) [\phi] \, dS = 0, \quad (3.18)$$

where at  $\Gamma_D$  the outer value  $\psi^{\text{out}} = \psi_D$  is given by the Dirichlet boundary condition (3.10b). In order to fully discretize the initial boundary value problem (3.10), one further needs to discretize the temporal term. This issue is skipped at this point and is discussed in Section ???. Thus, the current form of (3.18) is referred to as the semi-discrete weak formulation of (3.10).

Considering the spatial discretization, the numerical flux  $\hat{F}$  needs to satisfy certain mathematical and physical properties to ensure stability and convergence of the DG method. In this work the stability is defined in the continuous setting via the energy estimate

$$\|\psi(\mathbf{x}, t)\|_\Omega^2 \leq \|\psi(\mathbf{x}, 0)\|_\Omega^2, \quad \forall t \geq 0, \quad (3.19)$$

where homogenous Dirichlet conditions are assumed. Thus, stability is given, if the energy  $\|\psi(\mathbf{x}, t)\|_\Omega^2$  only decreases in the absence of an inflow. Two properties need to be fulfilled in order to proof that the discrete problem (3.18) satisfies the discrete equivalent of the energy estimate in (3.19). The numerical flux  $\hat{F}$  is required to be a function that is Lipschitz continuous and monotonic, see [di\\_pietro\\_mathematical\\_2012](#) for the proof. Furthermore, it is obvious that the DG method needs to regain a unique approximate solution to the underlying problem. Thus,  $\hat{F}$  satisfies the following consistency property

$$\hat{F}(a, a, \mathbf{n}) = \mathbf{f}(a) \cdot \mathbf{n}, \quad \forall a \in \mathbb{R}. \quad (3.20)$$

A direct consequence of (3.20) is that the weak formulation (3.18) is directly fulfilled for  $\psi = \psi$ . Since considering a general conservation law in its conservative form, one further requires that  $\hat{F}$  regains the global conservation property, i.e. the total amount of  $\psi$  only changes due to fluxes across the domain boundary  $\partial\Omega$ , by satisfying

$$\hat{F}(a, b, \mathbf{n}) = -\hat{F}(a, b, -\mathbf{n}), \quad \forall a, b \in \mathbb{R}. \quad (3.21)$$

The specific form of a suitable numerical flux  $\hat{F}$  is presented in Section ??, where the spatial discretization of the two-phase flow problem is discussed.

Note that the system (3.18) can be written in a shorten matrix formulation as

$$\mathbf{M} \frac{d\tilde{\psi}}{dt} + \mathbf{Op}(\tilde{\psi}) = \mathbf{b}, \quad (3.22)$$

where the sought-after coefficients are given as the solution vector  $\tilde{\psi} = \{\tilde{\psi}_{1,1}, \tilde{\psi}_{1,2}, \dots, \tilde{\psi}_{j,n}, \dots, \tilde{\psi}_{J,N_k}\} \in \mathbb{R}^N$ . The mass matrix  $\mathbf{M} \in \mathbb{R}^{N \times N}$  has a block-diagonal structure with

$$\mathbf{M} = \begin{bmatrix} \mathbf{M}_1 & 0 & \cdots & 0 \\ 0 & \mathbf{M}_2 & \cdots & 0 \\ \vdots & \vdots & \ddots & \vdots \\ 0 & 0 & \cdots & \mathbf{M}_J \end{bmatrix}, \quad (3.23)$$

where the cell-local mass matrix  $\mathbf{M}_j$  is defined by

$$(\mathbf{M}_j)_{m,n} = \int_{K_j} \phi_{j,m} \phi_{j,n} \, dV = \int_{K_j} \phi_j \otimes \phi_j \, dV. \quad (3.24)$$

The cell-local Operator matrix  $\mathbf{Op}_j$  is given by

$$(\mathbf{Op}_j)_{m,n} = - \int_{K_j} \mathbf{f}(\tilde{\psi}_{j,n} \phi_{j,n}) \cdot \nabla_h \phi_{j,m} \, dV + \oint_{\partial K_j} \hat{F}(\tilde{\psi}_{j,n}, \tilde{\psi}_{j^*,n}, \mathbf{n}_j) \phi_{j,m} \, dS, \quad (3.25)$$

where  $j^*$  denotes the index of a neighbouring cell to  $K_j$ . Like the mass matrix, the operator matrix exhibits a block-diagonal structure, but including secondary diagonals due to the coupling with neighbouring cells over the numerical fluxes  $\hat{F}$ . The right-hand side  $\mathbf{b}$  incorporates the given Dirichlet boundary condition value  $\psi_D$ .

### Discontinuous Galerkin discretization of the finite reaction rate problem

We start by presenting the DG discretization of the finite reaction system defined by ??–2.22d. We define  $\mathbf{Y}' = (Y_1, \dots, Y_{N-1})$  as the vector containing the first  $(n_s - 1)$  mass fractions and  $\mathbf{s} = (s_1, \dots, s_{N-1})$  as the vector containing the test functions for the first  $(n_s - 1)$  mass fraction equations. The discretized form of ???? and Equations (2.22c) and (2.22d) is obtained by multiplying each equation by a test function, integrating it over an element  $K$ , applying integration by parts and finally using an adequate numerical flux for each term. Note that the convective and diffusive terms of the temperature scalars  $T$ , mass fraction  $Y_\alpha$  and mixture fraction  $z$  have the same form, so they share the same expression in their discretized form. In order to ensure the validity of the Ladyzenskaja-Babuška-Brezzi (or inf-sup) condition, Babuška, 1973 we use a mixed order formulation, where polynomials of order  $k$  for velocity, temperature and mass fractions, and of degree  $k' = k - 1$  for pressure are used. Finally the discretized problem can be written as: find the numerical solution  $(p_h, \mathbf{u}_h, T_h, \mathbf{Y}'_h) \in \mathbb{V}_k$  such that for all test functions  $(q_h, \mathbf{v}_h, r_h, \mathbf{s}_h) \in \mathbb{V}_k$  we have:

$$\mathcal{B}^1(q_h) = \mathcal{C}(\mathbf{u}_h, q_h, \rho(T_h, \mathbf{Y}_h)) , , \quad (3.26a)$$

$$\begin{aligned} \mathcal{B}^2(\mathbf{v}_h) = & \mathcal{U}^C(\mathbf{u}_h, \mathbf{u}_h, \mathbf{v}_h, \rho(T_h, \mathbf{Y}_h)) + \mathcal{U}^P(p_h, \mathbf{v}_h) + \frac{1}{\text{Re}} \mathcal{U}^D(\mathbf{u}_h, \mathbf{v}_h, \mu(T_h)) \\ & + \frac{1}{\text{Fr}^2} \mathcal{U}^S(\rho(T_h, \mathbf{Y}_h), \mathbf{v}_h) , \end{aligned} \quad (3.26b)$$

$$\begin{aligned} \mathcal{B}^3(r_h) = & \mathcal{S}^C(\mathbf{u}_h, T_h, r_h, \rho(T_h, \mathbf{Y}_h)) + \frac{1}{\text{Re} \, \text{Pr}} \mathcal{S}^D(T_h, r_h, k/c_p(T_h)) \\ & + \text{H Da} \, \mathcal{S}^S(r_h, Q(T_h, \mathbf{Y}_h), \omega(T_h, \mathbf{Y}_h), c_p(T_h, \mathbf{Y}_h)) , \end{aligned} \quad (3.26c)$$

$$\begin{aligned} \mathcal{B}^3(s_{\alpha h}) = & \mathcal{S}^C(\mathbf{u}_h, Y_{\alpha h}, s_{\alpha h}, \rho(T_h, \mathbf{Y}_h)) + \frac{1}{\text{Re} \, \text{Pr} \, \text{Le}_\alpha} \mathcal{S}^D(Y_{\alpha h}, s_{\alpha h}, \rho D_\alpha(T_h)) \\ & + \text{Da} \mathcal{M}_\alpha^S(s_{\alpha h}, \omega(T_h, \mathbf{Y}_h)) . \end{aligned} \quad (3.26d)$$

where the index  $\alpha$  takes values  $\alpha = 1, \dots, (n_s - 1)$ . The  $n_s$ -th component mass fraction  $Y_{n_s}$  is calculated using Equation (2.23).

---

### Discontinuous Galerkin discretization of the flame sheet problem

---

Discretizing the flame sheet problem given by Equations (2.30a) to (2.30c) proceeds in a similar way. Due to the similarity of the mass fraction equation and the mixture fraction equation the discretization is analogous. Again, we use a mixed order formulation of polynomials of degree  $k$  for velocity and mixture fraction, and of degree  $k - 1$  for pressure. The resulting problem reads: find the numerical solution  $(p_h, \mathbf{u}_h, z_h) \in \mathbb{V}_k$  such that for all test functions  $(q_h, \mathbf{v}_h, r_h) \in \mathbb{V}_k$  we have:

$$\mathcal{B}^1(q_h) = \mathcal{C}(\mathbf{u}_h, q_h, \rho(z_h)), \quad (3.27a)$$

$$\begin{aligned} \mathcal{B}^2(\mathbf{v}_h) &= \mathcal{U}^C(\mathbf{w}_h, \mathbf{u}_h, \mathbf{v}_h, \rho(z_h)) + \mathcal{U}^P(p_h, \mathbf{v}_h) + \frac{1}{\text{Re}} \mathcal{U}^D(\mathbf{u}_h, \mathbf{v}_h, \mu(z_h)) \\ &\quad + \frac{1}{\text{Fr}^2} \mathcal{U}^S(\rho(z), \mathbf{v}_h), \end{aligned} \quad (3.27b)$$

$$\mathcal{B}^3(r_h) = \mathcal{S}^C(\mathbf{u}_h, z_h, r_h, \rho(z_h)) + \frac{1}{\text{Re} \text{Pr}} \mathcal{S}^D(z_h, r_h, \rho D(z_h)). \quad (3.27c)$$

Note that density and transport parameters are dependent on the mixture fraction  $z$ . The evaluation of those parameters is done as mentioned in ?? and solved iteratively using a Newton-Dogleg type method as shown later in Section 3.2.1

---

### Definitions of nonlinear forms

---

We show in the following the nonlinear forms used in this work. Regarding the choice of fluxes, we follow the "best practices" known in literature for the incompressible Navier-Stokes equation. It is known Pietro and Ern, 2012; Girault et al., 2004 that central difference fluxes for the pressure gradient and velocity divergence, combined with a coercive form for the viscous terms, e.g. symmetric interior penalty, gives a stable discretization for the Stokes equation. Furthermore, it is known that for all kinds of convective terms, a numerical flux which transports information in characteristic direction, e.g. Upwind, Lax-Friedrichs or Local-Lax-Friedrichs, must be used. We opted for the last one in our implementation, as it offers a good compromise between accuracy and stability.

**Continuity equation** We use a central difference flux for the discretization of the continuity equation:

$$\mathcal{C}(\mathbf{u}, q, \rho) = \oint_{\Gamma_l \cup \Gamma_N \cup \Gamma_{ND} \cup \Gamma_P} \{\rho \mathbf{u}\} \cdot \mathbf{n}_\Gamma \llbracket q \rrbracket \, dS - \int_\Omega \rho \mathbf{u} \cdot \nabla_h q \, dV. \quad (3.28)$$

The density in Equation (3.28) is evaluated as a function of the temperature and mass fractions using the equation of state (Equation (2.26)). The term  $\mathcal{B}^1$  on the right hand sides of Equation (3.26a) and Equation (3.27a) contains the Dirichlet boundary conditions:

$$\mathcal{B}^1(q) = - \oint_{\Gamma_D \cup \Gamma_{DW}} q (\rho_D \mathbf{u}_D \cdot \mathbf{n}_\Gamma) \cdot dS \quad (3.29)$$

The density at the boundary  $\rho_D$  is evaluated with Equation (2.26) using the corresponding Dirichlet values of temperature and mass fractions.

**Momentum equations** The convective term of the momentum equations is discretized using a Lax-Friedrichs flux

$$\mathcal{U}^C(\mathbf{w}, \mathbf{u}, \mathbf{v}, \rho) = \oint_{\Gamma} \left( \{\rho \mathbf{u} \otimes \mathbf{w}\} \mathbf{n}_{\Gamma} + \frac{\gamma_1}{2} [\![\mathbf{u}]\!] \right) \cdot [\![\mathbf{v}]\!] \, dS - \int_{\Omega} (\rho \mathbf{u} \otimes \mathbf{w}) : \nabla_h \mathbf{v} \, dV. \quad (3.30)$$

The Lax-Friedrichs parameter  $\gamma_1$  is calculated as Klein et al., 2016

$$\gamma_1 = \max \left\{ 2\overline{\rho^+} |\overline{\mathbf{u}^+} \cdot \mathbf{n}^+|, 2\overline{\rho^-} |\overline{\mathbf{u}^-} \cdot \mathbf{n}^-| \right\}, \quad (3.31)$$

where  $\overline{\rho_h^{\pm}}$  and  $\overline{\mathbf{u}^{\pm}}$  are the mean values of  $\rho^{\pm}$  and  $\mathbf{u}^{\pm}$  in  $K^{\pm}$ , respectively.  
The pressure term is discretized by using a central difference flux

$$\mathcal{U}^P(p, \mathbf{v}) = \oint_{\Gamma \setminus \Gamma_N \setminus \Gamma_{ND}} \{p\} ([\![\mathbf{v}]\!] \cdot \mathbf{n}) \, dS - \int_{\Omega} p \nabla_h \mathbf{v} \, dV. \quad (3.32)$$

The diffusive term of the momentum equations is discretized using an Symmetric Interior Penalty (SIP) formulation Shahbazi, 2005

$$\begin{aligned} \mathcal{U}^D(\mathbf{u}, \mathbf{v}, \mu) = & \int_{\Omega} \left( \mu \left( (\nabla_h \mathbf{u}) + (\nabla_h \mathbf{u})^T - \frac{2}{3} (\nabla_h \cdot \mathbf{u}) \mathbf{I} \right) \right) : \nabla_h \mathbf{v} \, dV \\ & - \oint_{\Gamma \setminus \Gamma_N \setminus \Gamma_{ND}} \left( \left\{ \mu (\nabla_h \mathbf{u} + \nabla_h \mathbf{u}^T - \frac{2}{3} (\nabla_h \cdot \mathbf{u}) \mathbf{I}) \right\} \mathbf{n}_{\Gamma} \right) \cdot [\![\mathbf{v}]\!] \, dS \\ & - \oint_{\Gamma \setminus \Gamma_N \setminus \Gamma_{ND}} \left( \left\{ \mu (\nabla_h \mathbf{v} + \nabla_h \mathbf{v}^T - \frac{2}{3} (\nabla_h \cdot \mathbf{v}) \mathbf{I}) \right\} \mathbf{n}_{\Gamma} \right) \cdot [\![\mathbf{u}]\!] \, dS \\ & + \oint_{\Gamma \setminus \Gamma_N \setminus \Gamma_{ND}} \eta \mu_{max} [\![\mathbf{u}]\!] [\![\mathbf{v}]\!] \, dS. \end{aligned} \quad (3.33)$$

The viscosity  $\mu$  is evaluated as a function of temperature according to Equation (2.29) and  $\mu_{max} = \max(\mu^+, \mu^-)$ . Additionally  $\eta$  is the penalty term of the SIP formulation, which has to be chosen big enough to ensure coercivity of the form, but also as small as possible in order to not increase the condition number of the problem. The estimation of the penalty term is based on an expression of the form

$$\eta = \eta_0 \frac{A(\partial K)}{V(K)}, \quad (3.34)$$

where for a two-dimensional problem  $A$  is the perimeter and  $V$  the area of the element. Parameter  $\eta_0$  is a safety factor and is set  $\eta_0 = 4$  in all calculations. Further information on the determination of the penalty term can be found in **hillewaertDevelopmentDiscontinuousGalerkin2013b**. The source term arising due to body forces is:

$$\mathcal{U}^S(\rho, \mathbf{v}) = \int_{\Omega} \rho \frac{\mathbf{g}}{\|\mathbf{g}\|} \cdot \mathbf{v} \, dV. \quad (3.35)$$

The right hand sides of Equation (3.26b) and Equation (3.27b) contain the information from Dirichlet boundary conditions:

$$\mathcal{B}^2(\mathbf{v}) = - \oint_{\Gamma_D} \left( (\rho \mathbf{u}_D \otimes \mathbf{u}_D) \mathbf{n}_{\Gamma} + \frac{\gamma_1}{2} \mathbf{u}_D \right) \cdot \mathbf{v} \, dS + \oint_{\Gamma_D} \mu_D \mathbf{u}_D \cdot (\nabla_h \mathbf{v} \mathbf{n}_{\Gamma} + \nabla_h \mathbf{v}^T \mathbf{n}_{\Gamma} - \eta \mathbf{v}) \, dS. \quad (3.36)$$

The Dirichlet viscosity value  $\mu_D$  is calculated from Equation (2.29) using the Dirichlet values of the temperature at the boundary.

**Scalar equations** Since the convective and diffusive term for the temperature, mass fractions and mixture fraction share a similar form, we summarize here their discretized expressions in terms of an arbitrary scalar  $X$  (corresponding to  $T$  in the energy equation,  $Y_\alpha$  in the equation for species  $\alpha$  and  $z$  for the mixture fraction equation) and transport parameter  $\xi$  (i.e.  $k/c_p$  in the energy equation, and  $(\rho D)$  for the mass fraction and mixture fraction equations). The convective term of the scalars is discretized using a Lax-Friedrichs flux

$$\mathcal{S}^C(\mathbf{u}, X, r, \rho) = \oint_{\Gamma} \left( \{\rho \mathbf{u} X\} \cdot \mathbf{n} + \frac{\gamma_2}{2} [X] \right) [r] \, dS - \int_{\Omega} (\rho \mathbf{u} X \cdot \nabla_h r) \, dV. \quad (3.37)$$

The Lax-Friedrichs parameter  $\gamma_2$  is calculated as Klein et al., 2016

$$\gamma_2 = \max \left\{ \overline{\rho^+} |\overline{\mathbf{u}^+} \cdot \mathbf{n}^+|, \overline{\rho^-} |\overline{\mathbf{u}^-} \cdot \mathbf{n}^-| \right\}. \quad (3.38)$$

The diffusion term of scalars is discretized again with a SIP formulation:

$$\begin{aligned} \mathcal{S}^D(X, r, \xi) &= \int_{\Omega} (\xi \nabla_h X \cdot \nabla_h r) \, dV \\ &- \oint_{\Gamma \setminus \Gamma_N \setminus \Gamma_{ND}} (\{\xi \nabla_h X\} \cdot \mathbf{n} [r] + \{\xi \nabla_h r\} \cdot \mathbf{n} [X] - \eta \xi_{\max} [X] [r]) \, dS. \end{aligned} \quad (3.39)$$

The transport parameter  $\xi$  is calculated as a function of temperature using Equation (2.29) and  $\xi_{\max} = \max(\xi^+, \xi^-)$ . The boundary condition term of the corresponding scalar equation is:

$$\mathcal{B}^3(r) = - \oint_{\Gamma_D \cup \Gamma_{ND}} \left( (\rho_D \mathbf{u}_D X_D) \cdot \mathbf{n}_\Gamma + \frac{\gamma_2}{2} X_D \right) r \, dS + \oint_{\Gamma_D \cup \Gamma_{ND}} \xi_D X_D (\nabla_h r \cdot \mathbf{n}_\Gamma - \eta r) \, dS. \quad (3.40)$$

Here,  $X_D$  is the Dirichlet value of the scalar  $X$  on boundaries and  $\xi_D$  is the corresponding transport parameter calculated, which is calculated with Equation (2.29) using the Dirichlet values of the temperature at the boundary. Finally, the volumetric source term of the energy and mass fraction equations are defined as follows:

$$\mathcal{S}^S(r, Q, \omega, c_p) = \int_{\Omega} \frac{Q\omega}{c_p} r \, dV, \quad (3.41)$$

$$\mathcal{M}_\alpha^S(s_\alpha, \omega) = \int_{\Omega} \nu_\alpha M_\alpha \omega s_\alpha \, dV. \quad (3.42)$$

The heat release  $Q$  is calculated with Equation (2.25), the reaction rate  $\omega$  is evaluated using Equation (2.24) and the mixture heat capacity with Equation (2.28).

### 3.1.3 Temporal discretization

Blabla second order backward difference scheme

$$\left( \frac{\partial \rho}{\partial t} \right)^n = \frac{1}{2\Delta t} (3\rho^n - 2\rho^{n-1}\rho^{n-2}) \quad (3.43)$$

## 3.2 Computational methodology

The presented solver is embedded in the *BoSSS* (Bounded Support Spectral Solver) code, which is under development at the chair of fluid dynamics of the Technical University of Darmstadt, and is available under <https://github.com/FDYdarmstadt/BoSSS>. *BoSSS* is a general framework for the discretization of conservation laws using the DG method and uses a modal DG approach with orthonormal Legendre polynomials as basis functions. The *BoSSS* code features a variety of applications in the context of computational fluid dynamics, such as a solver for multiphase flows with a sharp interface approach, Kummer, 2017 an incompressible Immersed Boundary Method solver for particle laden flows,Krause and Kummer, 2017 a solver for viscoelastic fluid flows,Kikker et al., 2020 and a solver for compressible flows, Geisenhofer et al., 2019 among others.

The variational problem for the finite chemistry rate case described by Equations (3.26a) to (3.26d) and for the flame sheet problem, Equations (3.27a) to (3.27c), are linearised and solved using a Newton method with a Dogleg-type globalization Pawłowski et al., 2006; Pawłowski et al., 2008. The *BoSSS* framework provides an efficient algorithm for the evaluation of the Jacobian based on perturbations of the forms presented in the last section. The relatively large linear system of equations for each Newton iteration is solved by means of the in *BoSSS* integrated orthonormalization multigrid algorithm Kummer et al., 2021, which at the lowest multigrid levels makes use of the sparse direct solver PARDISO, originally developed by Schenk et al. Schenk et al., 2000; Schenk and Gärtner, 2002; Schenk and Gärtner, 2004, from the “Intel(R) Parallel Studio XE 2018 Update 3 Cluster Edition for Windows” library collection to solve the linear system.

*BoSSS* also features a method for solving highly nonlinear problems with a homotopy strategy. Further details on the used Newton method solver, the homotopy strategy and its implementation are given in the next sections, which are adapted from Kikker et al., 2020 and are included for the sake of completeness. For information on the mentioned orthonormalization multigrid algorithm we refer the interested reader to the work of Kummer et al., 2021.

From this point on, the solver presented in this work will be called XNSEC (eXtended Navier-Stokes for Combustion). The term *extended* refers to the framework on which the solver is built, which focuses on applications for multi-phase flows using a sharp interface approach using a level-set method. This point will be briefly discussed in the section

### Calculation of the Jacobian matrix

We start by introducing a few new elements to be able to describe the implemented Newton method. The discussion for the variational problem using the mixture fraction variable (Equations (3.27a) to (3.27c)) is completely analogous, and will not be mentioned in this discussions. Find  $\mathbf{U}_h \in \mathbb{V}_k$

$$\mathcal{N}(\mathbf{U}_h, \mathbf{V}_h) = 0 \quad \forall \mathbf{V}_h \in \mathbb{V}_k, \quad (3.44)$$

for  $\mathbf{U}_h = (p_h, \mathbf{u}_h, T_h, \mathbf{Y}'_h)$  and  $\mathbf{V}_h = (q_h, \mathbf{v}_h, r_h, \mathbf{s}_h)$ . We assume a basis  $\underline{\Phi} = (\Phi_1, \dots, \Phi_L)$  of  $\mathbb{V}_k$ , written as a row vector, with  $L := \dim(\mathbb{V}_k)$ . Then  $\mathbf{U}_h$  can be represented as  $\mathbf{U}_h = \underline{\Phi} \cdot \mathbf{U}$ . The nonlinear problem (3.44) can then be written as

$$\mathcal{A}(\mathbf{U}) = 0, \quad (3.45)$$

with the nonlinear function  $\mathbb{R}^L \ni \mathbf{U} \mapsto \mathcal{A}(\mathbf{U}) \in \mathbb{R}^L$ . The  $i$ -th component of  $\mathcal{A}(\mathbf{U})$ , can be defined by  $\mathcal{N}(-, -)$  through the relation  $[\mathcal{A}(\mathbf{U})]_i = \mathcal{N}(\underline{\Phi} \cdot \mathbf{U}, \Phi_i)$ .

The formulation of the Newton method requires the Jacobian matrix  $\partial\mathcal{A}$  of  $\mathcal{A}$ , defined as

$$\partial\mathcal{A}_{ij}(\mathbf{U}) := \frac{\partial\mathcal{A}_i}{\partial U_j}(\mathbf{U}). \quad (3.46)$$

Its computation is quite straightforward, but lengthy. The *BoSSS* code is capable of evaluating the Jacobian matrix automatically from the expressions given in Section 3.1.1. We note that one could write  $\mathcal{A}(\mathbf{U})$  as

$$[\mathcal{A}(\mathbf{U})]_i = \mathcal{N}(\mathbf{U}_h, \Phi_i) = \int_{\Omega_h} N_1(\mathbf{x}, \mathbf{U}_h, \nabla \mathbf{U}_h) \cdot \Phi_i + N_2(\mathbf{x}, \mathbf{U}_h, \nabla \mathbf{U}_h) \cdot \nabla \Phi_i dV + \oint_{\Gamma} \dots dS. \quad (3.47)$$

The edge integral, which is left out in Equation (3.47), can be written in analogous fashion as the volume integral, i.e. as a sum over four nonlinear functions, multiplied by  $\Phi_i^+$ ,  $\Phi_i^-$ ,  $\nabla \Phi_i^+$  and  $\nabla \Phi_i^-$ , respectively. These functions themselves may depend on  $\mathbf{x}$ ,  $\mathbf{U}_h^+$ ,  $\mathbf{U}_h^-$ ,  $\nabla \mathbf{U}_h^+$  and  $\nabla \mathbf{U}_h^-$ . For sake of compactness, this part is skipped. Realizing that  $\frac{\partial \mathbf{U}_h}{\partial U_j} = \Phi_j$  and by application of the chain rule, one derives

$$\partial\mathcal{A}_{ij}(\mathbf{U}) = \int_{\Omega_h} (\partial_{\mathbf{U}_h} N_1(\mathbf{x}, \mathbf{U}_h, \nabla \mathbf{U}_h) \Phi_j + \partial_{\nabla \mathbf{U}_h} N_1(\mathbf{x}, \mathbf{U}_h, \nabla \mathbf{U}_h) \nabla \Phi_j) \cdot \Phi_i + \dots dV + \oint_{\Gamma} \dots dS. \quad (3.48)$$

All skipped terms in Equation (3.48) can be derived in an analogous fashion as the contributions for  $N_1$ . In the *BoSSS* code, derivatives  $\partial_{\mathbf{U}_h} N_1(\dots)$  and  $\partial_{\nabla \mathbf{U}_h} N_1(\dots)$  are approximated by a finite difference, using a perturbation by  $\sqrt{\text{eps}}$  in the respective argument, where  $\text{eps} = 2.22044604925031 \cdot 10^{-16}$  is the floating point accuracy for double precision.

The notation introduced here allows us to describe the Newton-Dogleg method used in this work. We note however that this globalization strategy is still not sufficient to ensure convergence for some of the test cases presented, namely for high Rayleigh numbers for the differentially heated cavity problem. For those cases we use a homotopy strategy, where we start with a low homotopy-parameter, a parameter for which the solution of the problem is not hard to find, which is gradually and carefully increased until convergence for the desired value of the homotopy-parameter is reached (cf. Section 3.2.4).

### 3.2.1 Dogleg Method

We consider a linearization of Equation (3.45) around  $\mathbf{U}_n$ ,

$$\mathcal{A}(\mathbf{U}_n) + \partial\mathcal{A}(\mathbf{U}_n) \underbrace{(\mathbf{U}_{n+1} - \mathbf{U}_n)}_{=: \mathbf{s}'_n} = 0. \quad (3.49)$$

By repeatedly solving this system one obtains a standard Newton scheme for Equation (3.45), yielding a sequence of approximate solutions  $\mathbf{U}_0, \mathbf{U}_1, \mathbf{U}_2, \dots$  obtained from an initial guess  $\mathbf{U}_0$  through the iteration scheme  $\mathbf{U}_{n+1} = \mathbf{U}_n + \mathbf{s}'_n$ . In the classical un-damped Newton method, the correction step  $\mathbf{s}'_n$  is set to be the whole Newton-step, i.e  $\mathbf{s}'_n = \mathbf{s}_n$  with

$$\mathbf{s}_n := -\partial\mathcal{A}(\mathbf{U}_n)^{-1} \mathcal{A}(\mathbf{U}_n), \quad (3.50)$$

which is computed using a direct solver. Unfortunately, convergence of the Newton method for any starting value  $\mathbf{U}_0$  is not guaranteed. In order to increase robustness when the distance between  $\mathbf{U}_0$  and the exact solution  $\mathbf{U}$  is large, we employ a globalization approach, presented by

Pawlowski et al. Pawlowski et al., 2006; Pawlowski et al., 2008, known as the Dogleg-method, or Newton-Dogleg method. Here, we intend to give only the central ideas of method and refer to the original works for further details. Obviously, the exact solution of Equation (3.45) is also a minimum of the functional

$$f(\mathbf{U}) := \frac{1}{2} \|\mathcal{A}(\mathbf{U})\|_2^2. \quad (3.51)$$

One observes that  $\nabla f(\mathbf{U}) = \partial\mathcal{A}(\mathbf{U})^T \mathcal{A}(\mathbf{U})$ . For  $\mathbf{U}_n$ , the approximate Cauchy point with respect to the 2-norm, is defined as the minimizer  $\mathbf{g}_n$  of  $\|\mathcal{A}(\mathbf{U}_n) + \partial\mathcal{A}(\mathbf{U}_n)\mathbf{g}_n\|_2$  in the direction of steepest decent, i.e.  $\mathbf{g}_n = \lambda \nabla f(\mathbf{U}_n)$ ,  $\lambda \in \mathbb{R}$ . Substituting  $\mathbf{w} := -\partial\mathcal{A}(\mathbf{U}_n) \nabla f(\mathbf{U}_n)$ ,  $\mathbf{g}_n$  is given by

$$\mathbf{g}_n = \frac{\mathcal{A}(\mathbf{U}_n) \cdot \mathbf{w}}{\mathbf{w} \cdot \mathbf{w}} \nabla f(\mathbf{U}_n). \quad (3.52)$$

For the Newton-Dogleg method, the correction step  $\mathbf{s}'_n$  is chosen along the so-called Dogleg curve, which is the piece-wise linear curve from the origin to  $\mathbf{g}_n$  and further to  $\mathbf{s}_n$ . The selection of  $\mathbf{s}'_n$  on this curve is determined by the trust-region diameter  $\delta > 0$ :

- If  $\|\mathbf{s}_n\|_2 \leq \delta$ ,  $\mathbf{s}'_n = \mathbf{s}_n$ .
- If  $\|\mathbf{g}_n\|_2 \leq \delta$  and  $\|\mathbf{s}_n\|_2 > \delta$ ,  $\mathbf{s}'_n$  is chosen on the linear interpolation from  $\mathbf{g}_n$  to  $\mathbf{s}_n$  so that  $\|\mathbf{s}'_n\|_2 = \delta$ : For the ansatz  $\mathbf{s}'_n = \tau \mathbf{s}_n + (1 - \tau) \mathbf{g}_n$ , the interpolation factor  $\tau$  is given as  $\tau = (a^2 - c + \sqrt{(a^2 + b^2 - 2c)\delta^2 - a^2b^2 + c^2})/(a^2 + b^2 - 2c)$  with  $a = \|\mathbf{g}_n\|_2$ ,  $b = \|\mathbf{s}_n\|_2$  and  $c = \mathbf{g}_n \cdot \mathbf{s}_n$ .
- If  $\|\mathbf{g}_n\|_2 > \delta$ ,  $\mathbf{g}_n = (\delta/\|\mathbf{g}_n\|_2)\mathbf{g}_n$ .

The choice and adaptation of the trust region diameter  $\delta$  throughout the Newton-Dogleg procedure follows a sophisticated heuristic, mainly based on comparing the actual residual reduction  $\text{ared}_n := \|\mathcal{A}(\mathbf{U}_n)\|_2 - \|\mathcal{A}(\mathbf{U}_n + \mathbf{s}'_n)\|_2$  with the predicted residual reduction  $\text{pred}_n := \|\mathcal{A}(\mathbf{U}_n)\|_2 - \|\mathcal{A}(\mathbf{U}_n) + \partial\mathcal{A}(\mathbf{U}_n)\mathbf{s}'_n\|_2$ ; For the direct solver used in this work  $\text{pred}_n$  simplifies to  $\text{pred}_n := \|\mathcal{A}(\mathbf{U}_n)\|_2$ . We replicate the algorithm here, for the sake of completeness:

- (1) Set  $n = 0$ ,  $\delta_n = \min(10^{10}, \max(2 \cdot 10^{-6}, \|\mathbf{s}_0\|_2))$ .
- (2) Compute the Newton step  $\mathbf{s}_n$  and the Cauchy point  $\mathbf{g}_n$  and find  $\mathbf{s}'_n$  on the Dogleg curve with respect to the recent  $\delta_n$ .
- (3) While  $\text{ared}_n \leq \text{pred}_n$  do: Update trust region diameter  $\delta_n \leftarrow 0.5 \delta_n$  and re-compute  $\mathbf{s}'_n$ . If  $\delta_n < 10^{-6}$  terminate abnormally and mark the computation as failed.
- (4) If the convergence criterion (see below) is fulfilled, terminate and mark the computation as success.
- (5) Perform a final update of the trust region: Set

$$\delta_{n+1} = \begin{cases} \max(10^{-6}, \|\mathbf{s}_n\|_2) & \text{if } \text{ared}_n/\text{pred}_n < 0.1 \text{ and } \|\mathbf{s}_n\|_2 \delta_n \\ \max(10^{-6}, 0.25 \cdot \delta_n) & \text{else, if } \text{ared}_n/\text{pred}_n < 0.1 \\ \min(10^{10}, 4 \cdot \delta_n) & \text{else, if } \text{ared}_n/\text{pred}_n > 0.75 \\ \delta_n & \text{otherwise} \end{cases}$$

Set  $\mathbf{U}_{n+1} = \mathbf{U}_n + \mathbf{s}'_n$ , update  $n \leftarrow n + 1$  and return to step (2).

All constants used in the algorithm above have been taken from the work of Pawlowski et al. Pawlowski et al., 2006 For a detailed description of the underlying ideas we also refer to these works, which in turn are based on algorithms from Dennis and Schnabel's textbook. Dennis and Schnabel, 1996

### 3.2.2 Termination criterion

A simple approach to determine that a Newton-Dogleg loop can be terminated is to check whether the residual norm has fallen below a certain threshold, i.e.  $\|\mathcal{A}(U_n)\| \leq \text{tol}$ . A universal choice for the tolerance is indeed difficult, especially for investigations of convergence properties (cf. Section 4.2.3 and Section 4.3.3). If it is chosen too low, the algorithm may never terminate, because of dominating numerical round-off errors. On the other hand, if it is chosen too high, the error of the premature termination may dominate the error of the spatial discretization and one cannot take the full advantage of the high-order method. Therefore the goal is to continue the Newton-Dogleg method until the lowest possible limit dictated by floating point accuracy is reached. To identify the limit in a robust way, we first define the residual-norm skyline as

$$\text{sr}_n := \min_{j \leq n} \|\mathcal{A}(\mathbf{U}_j)\| \quad (3.53)$$

and, for  $n \geq 2$ , the averaged reduction factor

$$\text{arf}_n := \frac{1}{2} \left( \frac{\text{sr}_{n-2}}{\max\{\text{sr}_{n-1}, 10^{-100}\}} + \frac{\text{sr}_{n-1}}{\max\{\text{sr}_n, 10^{-100}\}} \right). \quad (3.54)$$

The Newton-Dogleg method is terminated if

$$n \geq 2 \text{ and } \text{sr}_n \leq 10^{-5} + 10^{-5} \|\mathbf{U}_n\|_2 \text{ and } \text{arf}_n < 1.5. \quad (3.55)$$

For the computations in this work, this choice guarantees that the nonlinear system is solved as accurately as possible. It secures that the numerical error is dominated by the error of the spatial or temporal discretization and not by the termination criterion of the Newton-Dogleg method. The skyline approach ensures robustness against oscillations close to the lower limit.

### 3.2.3 Solver safeguard

/// 'safeguard' for solvers to avoid unphysical solutions during the solution procedure; /// An example would be to avoid e.g. negative densities, which might even cause NaNs, /// during the solver run for implicit, nonlinear equations.

### 3.2.4 Homotopy method

Although the Newton-Dogleg method works well for a variety of cases, we experienced convergence problems for some of the test cases presented in next section. In particular, for the differentially heated cavity test case, the method was not successful on finding a convergent solution for a Rayleigh number  $Ra \geq 10^5$  within 60 Newton iterations. In such cases we used a homotopy strategy, which is loosely based on ideas from the textbook of Deuflhard, Deuflhard, 2011 Chapter 5.

We start by identifying a parameter that makes the solution of the nonlinear problem difficult to solve. In the following we will refer to this variable as the homotopy parameter. The main

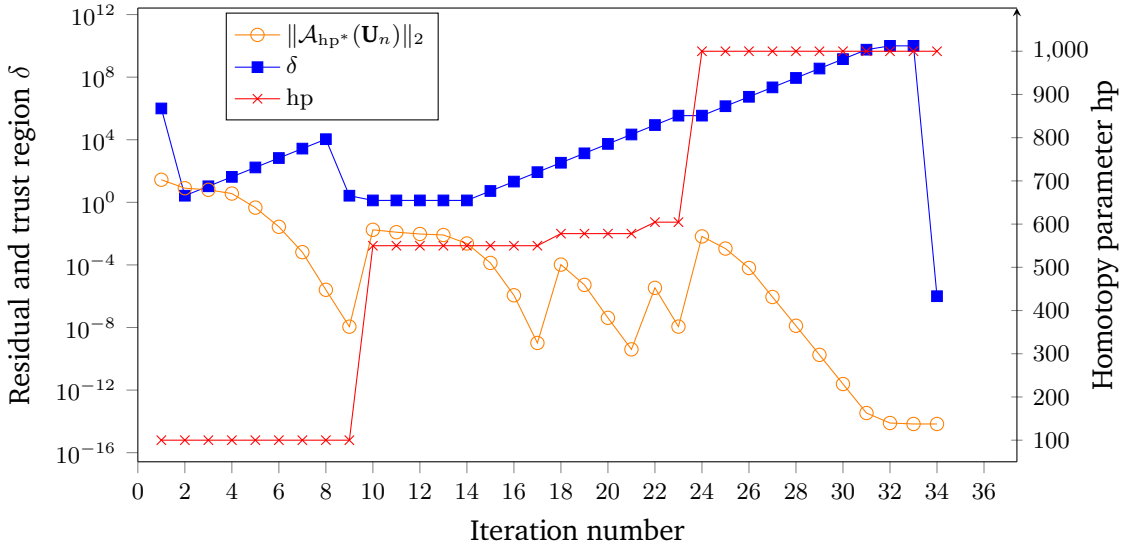


**Figure 3.1:** Behaviour of the homotopy method for the differentially heated cavity test case. The homotopy parameter  $hp$  in this case is the Reynolds number.

idea of the homotopy strategy consists of solving a series of simpler problems, starting with a parameter where the problem is easy to solve, and carefully increasing it until the desired value is reached. Let  $Hp$  denote the value of the homotopy parameter for which a solution is being sought. Let

$$\mathcal{A}_{hp^*}(\mathbf{U}) = 0 \quad (3.56)$$

be the discretized system for a certain intermediate homotopy-parameter  $hp^*$ , between 0 and the ‘target’ homotopy-parameter  $Hp$ , i.e.  $0 \leq hp^* \leq Hp$ . Furthermore, let  $\mathbf{U}_{hp,\epsilon}$  be an approximate solution to the problem (3.56) with  $hp^* = hp$ , up to a tolerance  $\epsilon$ , i.e.

$$\|\mathcal{A}_{hp}(\mathbf{U}_{hp,\epsilon})\|_2 \leq \epsilon. \quad (3.57)$$

For the sake of clarity when discussing the algorithm which follows below, we distinguish between the intermediate homotopy-parameter  $hp$  for which we assume to already have found an acceptable solution and the next homotopy-parameter  $hp^*$  that we are currently trying to find a solution for. For any  $hp^* > hp$  we set  $\epsilon = 10^{-5} \|\mathcal{A}_{hp^*}(\mathbf{U}_{hp,\epsilon})\|_2$ , i.e. we aim for a residual norm reduction of at least five orders of magnitude with respect to the initial residual norm. If  $hp^* = Hp$ , the termination criterion presented in section 3.2.2 is applied. An approximate solution for the target homotopy-parameter is found by the following recipe:

- (1) Set  $hp = 0$ , i.e. start by obtaining an (approximate) solution  $\mathbf{U}_{0,\epsilon}$ .
- (2) Search for a an increased homotopy-parameter  $hp^*$ : Find the minimal  $i \geq 0$  so that for  $hp^* = \frac{1}{2^i}(Hp - hp) + hp$  one has  $\|\mathcal{A}_{hp^*}(\mathbf{U}_{hp,\epsilon})\|_2 \leq \delta_{\max} \|\mathcal{A}_{hp}(\mathbf{U}_{hp,\epsilon})\|_2$ . Here,  $\delta_{\max}$  is the maximal allowed increase of the residual for an increased homotopy-parameter  $hp^*$ ;  $\delta_{\max}$  is adapted in the following steps, as an initial guess we use  $\delta_{\max} = 10^6$ .
- (3) Use the Newton-Dogleg method to compute an approximate solution to the problem (3.56), for the homotopy-parameter  $hp^*$ , using the solution  $\mathbf{U}_{hp,\epsilon}$  as an initial guess.

- If the Newton-Dogleg method did not converge successfully within ten steps, the homotopy-parameter increase from  $hp$  to  $hp^*$  was probably too large. Set  $\delta_{\max} \leftarrow 0.2\delta_{\max}$  and go to step (2).
- If the Newton-Dogleg method reached its convergence criterion and if the target homotopy-parameter is reached, i.e.  $hp^* = Hp$ , the algorithm has successfully found an approximate solution for  $\mathcal{A}_{Hp}(\mathbf{U}) = 0$  and can terminate.
- Otherwise, if the Newton-Dogleg method converged successfully, but is below the target homotopy-parameter: Accept the solution and set  $hp \leftarrow hp^*$ . If the Newton-Dogleg method took less than three iterations to reach the convergence criterion, set  $\delta_{\max} \leftarrow 8\delta_{\max}$ . Return to step (2).

An exemplary run of the method is shown in Figure 3.1. The homotopy parameter  $hp$  in this particular case is the Reynolds number. The homotopy-parameter  $hp$  was increased for iterations 10, 18, 22 and 24, causing an increase of the residuals  $\|\mathcal{A}_{hp^*}(\mathbf{U}_n)\|_2$ , leading to a convergent solution after 34 Newton iterations. The presented algorithm offers a robust method for finding steady-state solutions of highly nonlinear systems.

### 3.2.5 Initialization of combustion applications

Cases involving combustion are initialized with the solution of the flame sheet problem, Equations (3.27a) to (3.27c). This idea has been already employed in various works. Smooke et al., 1986; Smooke and Giovangigli, 1992 The reason for the use of this pre-step is twofold:

- Solving **????** and Equations (2.22c) and (2.22d) using a Newton-type method requires adequate starting estimates in order to converge. Using the flame sheet solution as initial estimate improves the convergence properties of the method.
- The system of **????** and Equations (2.22c) and (2.22d) possesses multiple solutions. One is the pure mixing (frozen) solution, where no chemical reaction has taken place, and the other one is the ignited solution, where the flame is present. Using the flame sheet solution as initial estimate ensures that the path taken by Newton's algorithm will tend towards the ignited solution.

It should be noted regarding the solution of the flame sheet problem (cf. Section 2.2) that the sharp change in the primitive variables around  $z = z_{st}$  is problematic in certain scenarios. In particular, the non-smoothness of the derived variables could lead to Gibbs phenomenon-type problems. This inconvenient can be remedied by using a regularized form of the equations. The smoothing function  $\mathcal{H}$  is defined as

$$\mathcal{H}(z) \approx \frac{1}{2}(1 + \tanh(\frac{z - z_{st}}{\sigma})), \quad (3.58)$$

This function is useful for creating a smooth transition between two functions, since it returns values close to -1 for  $z \ll z_{st}$  and values close to 1 for  $z \gg z_{st}$ . The sharpness of the transition at the point  $z = z_{st}$  is dictated by the parameter  $\sigma$ . In Figure 3.2 the effect of the smoothing factor  $\sigma$  on calculations of a flame in a counter-flow configuration are shown. It can be clearly observed how for increasing  $\sigma$  the solution becomes smoother. Using Equation (3.58) the

temperature and mass fraction fields can be written as

$$T(z) = zT_F^0 + (1-z)T_O^0 + \frac{QY_F^0}{c_p} z_{st} \frac{1-z}{1-z_{st}} \mathcal{H}(z) + \frac{QY_F^0}{c_p} z (1 - \mathcal{H}(z)), \quad (3.59a)$$

$$Y_F(z) = Y_F^0 \frac{z - z_{st}}{1 - z_{st}} \mathcal{H}(z), \quad (3.59b)$$

$$Y_O(z) = Y_O^0 \frac{z_{st} - z}{z_{st}} (1 - \mathcal{H}(z)), \quad (3.59c)$$

$$Y_P(z) = Y_O^0 \frac{M_P \nu_P}{M_O \nu_O} (1 - z) \mathcal{H}(z) + Y_F^0 \frac{M_P \nu_P}{M_F \nu_F} z (1 - \mathcal{H}(z)), \quad (3.59d)$$

$$Y_N(z) = (1 - Y_F^0)z + (1 - Y_O^0)(1 - z). \quad (3.59e)$$

The use of this regularized form of the equations results in practice on a spreading of the flame front, which eases the numerical calculation (Braack et al., 1997).

Some remarks regarding the use of the infinite reaction-rate solution (also called flame-sheet solution in the following) as initial condition for a finite-rate problem should be done. Although for the solution of the infinite reaction rate system the mixture heat capacity has been assumed to be constant, it remains an adequate estimate for the finite reaction-rate problem, where the heat capacity is a function of temperature and local concentration. In a similar fashion, the assumption of unity Lewis number in the flame sheet system delivers a solution that slightly deviates from the solution of the finite chemistry rate problem with non-unity Lewis numbers. Nevertheless, this small deviation does not preclude the use of the flame sheet solution as an adequate initial estimate for Newton's method.

One problem that arises when using the flame sheet estimate is the selection of a suitable  $c_p$ , since the flame temperature - and therefore all other solution fields - are highly dependent on the selection of the heat capacity. Xu and Smooke, 1993 suggests estimating it simply on the basis of experimental measurements, or also by selecting some representative value.

It should also be noted that `crefq:heatReleaseOneStep` yields unphysical values of  $\hat{Q}$  for large values of  $\phi$ . This problem can be avoided by setting an upper boundary value for  $\phi$  in Equation (2.20) (we use  $\phi = 1.2$ ). In practice however, this should not have a significant effect, because the unphysical values of  $\hat{Q}$  appear at zones where the reaction rate  $\hat{\omega}$  is very close to zero, making the factor  $\hat{Q}\hat{\omega}$  in the temperature equation negligible. Nevertheless, setting an upper bound for  $\phi$  is helpful to avoid possible numerical instabilities.

## Adaptive Mesh Refinement

The area where the chemical reaction takes place is usually a thin region whose thickness is defined by the availability of reactants.

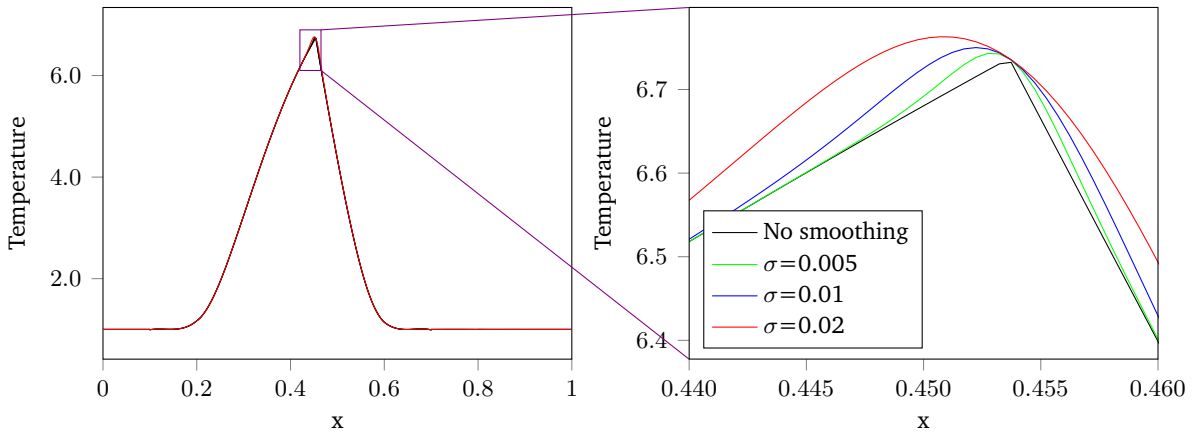


**Figure 3.2:** Temperature profile calculated in the center-line of a counter-flow flame configuration for different smoothing parameters  $\sigma$ .



## 4 Results

---

The following sections show a comprehensive solver validation using various test cases presented in increasing levels of complexity. The tests also allow to highlight some of the benefits of the DG-method. In Section 4.1 the applicability of the solver is analyzed for isothermal single-component systems. Later in Section 4.2 several single-component non-isothermal configurations are studied. Finally, in Section 4.3 test cases for multicomponent non-isothermal systems are presented, with a particular emphasis on systems where combustion is present.

All calculations shown here were performed on a cluster with the following specifications.

- **CPU** 4x8 cores (Intel(R) Xeon(R) CPU E5-4627 v2)
- **CPU vector extension** Intel® AVX
- **CPU speed** basis 3.30 GHz, turbo 3.6 GHz
- **memory** 512 GByte (DDR3-1600)

Unless otherwise stated, all calculations use the termination criteria presented in Section 3.2.2. Some of the results presented in the next sections has been published (Gutiérrez-Jorquera and Kummer, 2022).

---

### 4.1 Single-component isothermal cases

---

The XNSEC-solver presented in the previous chapter is validated first for single-component isothermal cases. In these cases, only the continuity and momentum equations are solved. The energy equation and the species concentration equations are replaced by the conditions  $T = 1.0$  and  $Y_0 = 1.0$  in the entire domain. This means that the physical properties of the flow (density and viscosity) are constant and that the flow is fully incompressible because the density does not show a thermodynamic or hydrodynamic dependence.

---

#### 4.1.1 Lid-driven cavity flow

---

The lid-driven cavity flow is a classically used test problem for the validation of Navier-Stokes solvers. The system configuration is shown in Figure 4.1. It consists simply of a two-dimensional square cavity enclosed by walls whose upper boundary moves at constant velocity, causing the fluid to move. Benchmark results can be found widely in the literature for different Reynolds numbers. In this section, the results obtained with the XNSEC-Solver are compared with those published by Botella and Peyret, 1998.

The problem is defined in the domain  $\Omega = [0, 1] \times [0, 1]$ . The system is solved for the velocity vector  $\mathbf{u} = (u, v)$  and the pressure  $p$ . All boundary conditions are Dirichlet-type, particularly with  $\mathbf{u} = (-1, 0)$  for the boundary at  $y = 1$  and  $\mathbf{u} = (0, 0)$  for all other sides. The gravity vector is set to  $\mathbf{g} = (0, 0)$ . A Cartesian mesh with extra refinement at both upper corners is used,

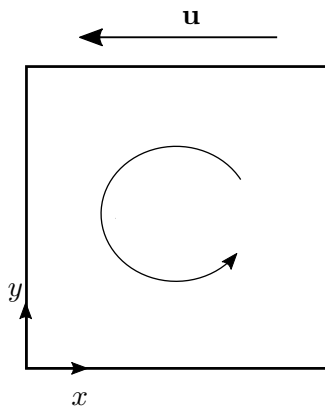


**Figure 4.1:** Schematic representation of the Lid-Driven cavity flow.

and is shown in Figure 4.2. The refinement was done to better represent the complex effects that take place in the corners. The streamline plot presented in Figure 4.2 shows the different vortex structures typical of this kind of system, where in addition to the main vortex of the cavity, smaller structures appear in the corners.

The lid-driven cavity was calculated for a Reynolds number  $\text{Re} = 1000$ . For the calculations presented here, the polynomial degree is set to  $k = 4$  and  $k' = 3$ . A regular Cartesian mesh with  $16 \times 16$  elements is used with extra refinement in the corners. In Figure 4.3 a comparison of the calculated velocity with the DG-Solver and the velocities provided by the benchmark is shown. Clearly, very good agreement is obtained, even by using a relatively coarse mesh (the benchmark result uses a grid with  $160 \times 160$  elements).

A more rigorous comparison of results is presented in Table 4.1, where the extreme values of the velocity components calculated through the centerline of the cavity are compared with the results presented by Botella and Peyret, 1998. Different mesh resolutions were used for this comparison, particularly meshes with  $16 \times 16$ ,  $32 \times 32$ ,  $64 \times 64$ ,  $128 \times 128$  and  $256 \times 256$  elements, each with extra refinement at the corners. It can be clearly seen how for the finest mesh the results obtained with the DG-solver are extremely close to the reference, seeing a difference only at the fifth digit after the decimal point for the velocity components, and no

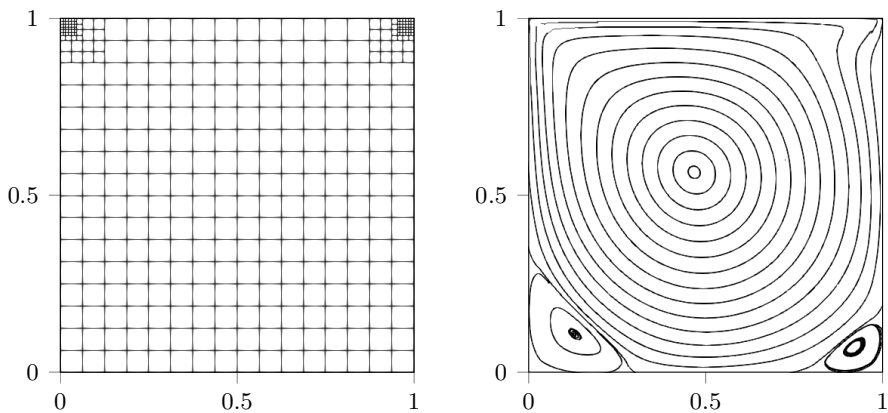


**Figure 4.2:** Mesh and streamlines of the lid-driven cavity flow with  $\text{Re} = 1000$

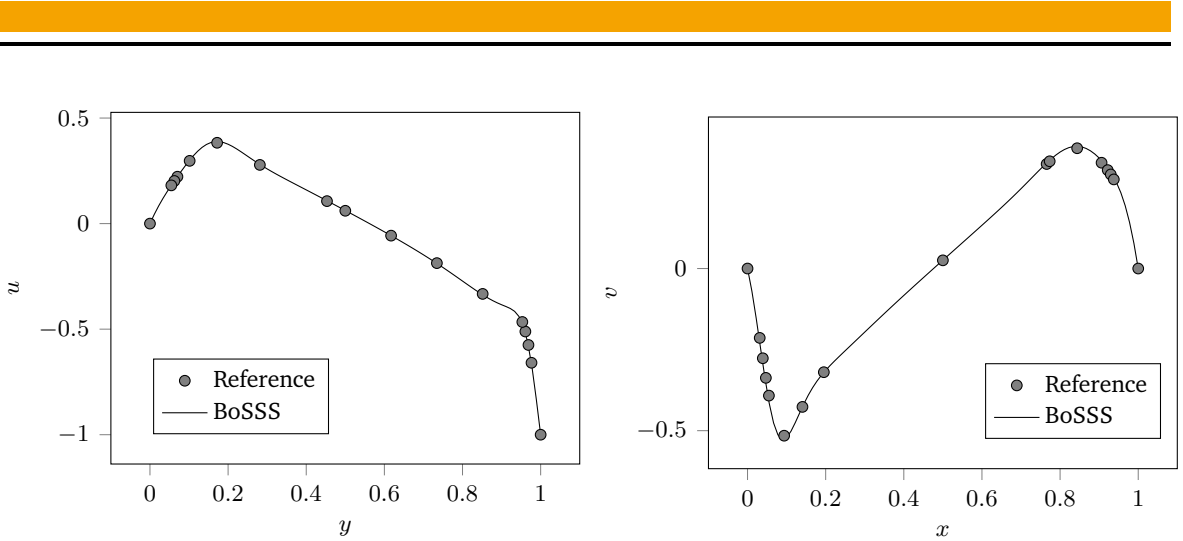


**Figure 4.3:** Calculated velocities along the centerlines of the cavity and reference values. Left plot shows the x-velocity for  $x = 0.5$ . Right plot shows the y-velocity for  $y = 0.5$

Mesh	$u_{\max}$	$y_{\max}$	$v_{\max}$	$x_{\max}$	$v_{\min}$	$x_{\min}$
$16 \times 16$	0.3852327	0.1820	0.3737295	0.8221	-0.5056627	0.0941
$32 \times 32$	0.3872588	0.1821	0.3760675	0.8227	-0.5080496	0.0943
$64 \times 64$	0.3897104	0.1748	0.3774796	0.8408	-0.5248360	0.0937
$128 \times 128$	0.3886452	0.1720	0.3770127	0.8422	-0.5271487	0.0907
$256 \times 256$	0.3885661	0.1717	0.3769403	0.8422	-0.5270653	0.0907
Reference	0.3885698	0.1717	0.3769447	0.8422	-0.5270771	0.0908

**Table 4.1:** Extrema of velocity components through the centerlines of the lid-driven cavity for  $\text{Re} = 1000$ . Reference values obtained from Botella and Peyret, 1998

difference for the spatial coordinates where the extrema are. It can also be appreciated that the results obtained with the coarser meshes are still very close to those of the reference. It is worth mentioning that this comparison only considering number of elements could be considered unfair, since the reference uses another method for solving the governing equations. One of the advantages of the DG method is that choosing higher-order polynomials allows more information to be packed into each cell. A better comparison would be achieved by comparing results based on the number of degrees of freedom(dofs) used in the simulation, as will be done later in section

#### 4.1.2 Backward-facing step

The backward-facing step problem is another classical configuration widely used for validation of incompressible CFD codes. It has been widely studied theoretically, experimentally, and numerically by many authors in the last decades (see, for example, Armaly et al., 1983; Barkley et al., 2000; Biswas et al., 2004). In Figure 4.4 a schematic representation of the problem is shown. It consists of a channel flow (usually considered fully developed) that is subjected to a sudden change in geometry that causes separation and reattachment phenomena. For these reasons, this case can be considered more challenging than the one presented in the previous section, since special care of the mesh used has to be taken in order to capture accurately all complex phenomena taking place.

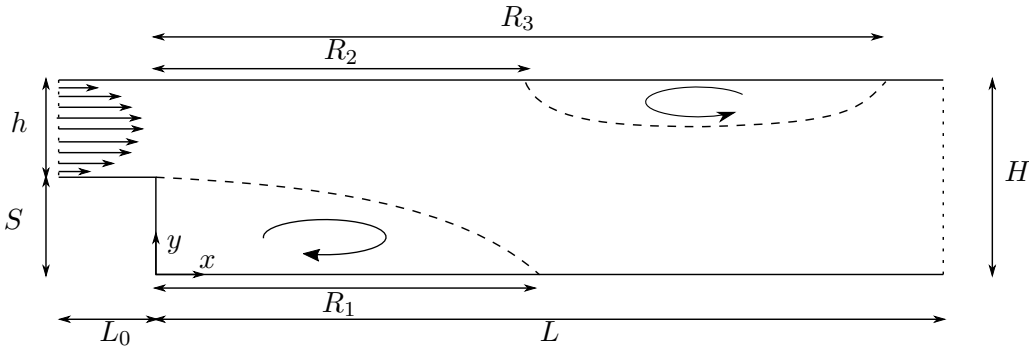


**Figure 4.4:** Schematic representation of the backward-facing step. Both primary and secondary vortices are shown. Sketch is not to scale.

Although the backward-facing step problem is known to be inherently three-dimensional, it has been shown that it can be studied as a two-dimensional configuration along the symmetry plane for moderate Reynolds numbers. For the range of Reynolds numbers used in the calculations presented here, the two-dimensional assumption is justified (Barkley et al., 2000; Biswas et al., 2004). The origin of the coordinate system is set in the bottom part of the step. The step height  $S$  and channel height  $h$  characterize the system. Results in the literature are often reported as a function of the expansion ratio, defined as  $ER = (h + S)/h$ .

A series of simulations were performed with the objective of reproducing the results reported by Biswas et al., 2004, where the backward-facing step was calculated for Reynolds numbers up to 400 and for an expansion ratio of 1.9423. In particular, the reported lengths of deattachment and reattachment are used as a means of comparison with the results from the XNSEC-solver.

The Reynolds number for the backward-facing step configuration is defined in the literature in many forms. Here, the definition based on the step height  $\hat{S}$  and the mean inlet velocity  $\hat{U}_{\text{mean}}$  is adopted as the reference length and velocity, resulting in

$$\text{Re} = \frac{\hat{S}\hat{U}_{\text{mean}}}{\hat{\nu}}. \quad (4.1)$$

The boundary at  $x = -L_0$  is an inlet boundary condition, where a parabolic profile is defined with

$$u(y) = -6 \frac{(y - S)(y - (h + S))}{h^2} \quad (4.2)$$

The system is isothermal, and the fluid is assumed to be air. The step length is set  $S = 1$  and  $h = 1.061$ . To minimize the effects of the outlet boundary condition on the part of interest in the system, the length  $L$  of the domain is set to  $L = 70S$ . All other boundaries are fixed walls. From prior calculations, the effect of the domain length before the step was found to have almost no impact on the results and is set to  $L_0 = S$ . Preliminary calculations showed that the calculated reattachment and detachment lengths are highly sensitive to the mesh resolution. For all calculations in this section, a structured grid with 88400 elements is used. To better resolve the complex structures that occur in this configuration, smaller elements are used in the vicinity of the step, as seen in Figure 4.5. A polynomial degree of three was chosen for both velocity components and two for pressure.

The backward-facing step configuration exhibits varying behavior as the number of Reynolds changes. For small Reynolds numbers, a single vortex, usually called the primary vortex, appears in the vicinity of the step. Furthermore, as the Reynolds number increases, a second vortex

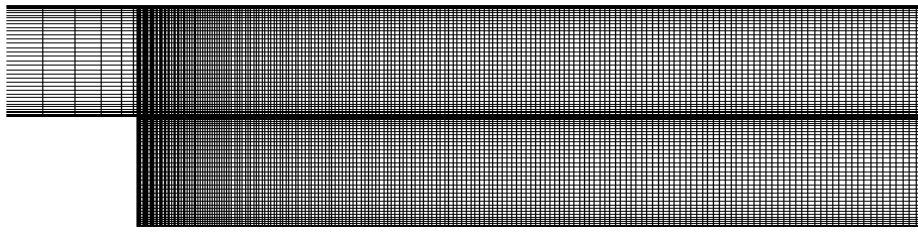


**Figure 4.5:** Structured mesh used in all calculations.

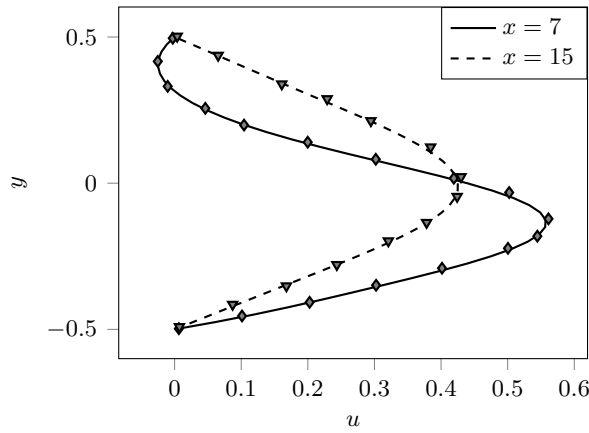


**Figure 4.6:** Distribution of  $x$ -component of velocity in the backward-facing step configuration for a Reynolds number of 400. Solid lines correspond to results obtained with the XNSEC solver

eventually appears on the top wall, as shown schematically in Figure 4.4. The detachment and reattachment lengths of the vortices are values that are usually reported in the literature. It is possible to determine the detachment position by finding the point along the wall where the velocity gradient normal to the wall acquires a value equal to zero.

Figure 4.7 shows the detachment and reattachment lengths of the primary and secondary vortices obtained with the XNSEC solver for different Reynolds numbers, which are also compared with the results presented in the reference paper from Biswas et al., 2004. Cubic splines have been used to accurately locate this point. It can be seen that the results for the detachment lengths of the primary vortex  $R_1$  are in very good agreement with those of the reference. In the case of the secondary vortex, it is possible to see a very minimal deviation for the lengths of the reattachment  $R_3$ , hinting at a possible spatial underresolution far away from the step. It is interesting to note that, despite the fact that the reference does not report the existence of a secondary vortex for  $Re = 200$ , it was possible to observe it with the XNSEC-solver. The results allow us to conclude that it is possible to study flows with complex behavior for low- to moderate Reynolds numbers, at least in the isothermal case. In the next section, a non-isothermal case of this configuration will be studied.

It is worth mentioning that the evaluation of the global order of accuracy of the solver using the two incompressible test cases presented in this section is problematic due to the presence of singularities, specifically at the corners at the coordinates  $\mathbf{x} = (0, 1)$  and  $\mathbf{x} = (1, 1)$  of the Lid-driven cavity (where the pressure is not finite according to Botella and Peyret, 1998), and at the corner of the step  $\mathbf{x} = (0, S)$  of the backward-facing step. The accuracy of the solver will

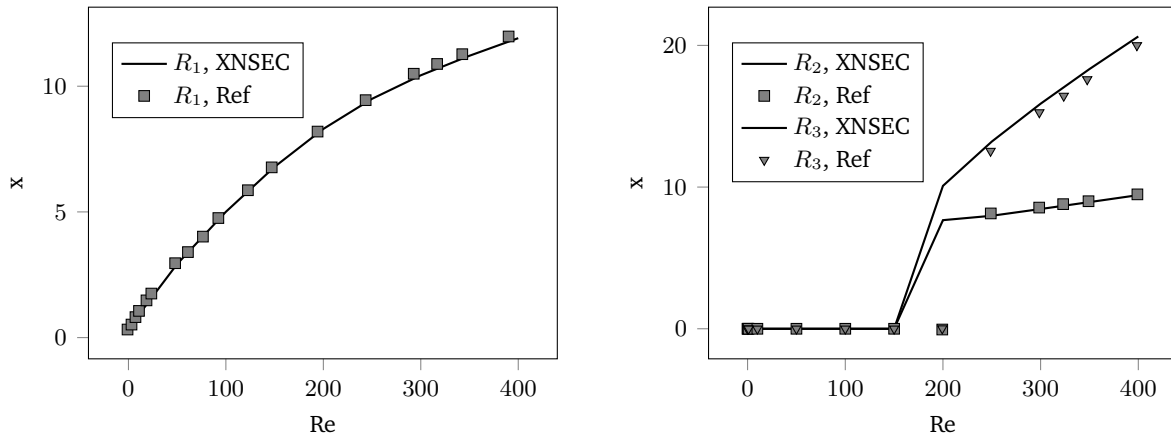


**Figure 4.7:** Detachment and reattachment lengths of the primary (left figure) and secondary (right figure) recirculation zones after the backward-facing step compared to the reference solution (Biswas et al., 2004).

be assessed later in Section 4.2.2 making use of a analytical solution and Section 4.2.3 using a solution obtained with a high spatial resolution.

## 4.2 Single-component non-isothermal cases

For the test cases presented in this section, the equations for continuity, momentum and energy are solved. All systems are assumed to be single-component, thus  $N = 1$  and  $Y_0 = 1.0$ . The tests shown in this section shall serve as a throughout validation of the XNSEC-solver spatial and temporal discretization for low-Mach variable density flows.

First in Section 4.2.1 an extension of the backward-facing step configuration for a non-isothermal system is shown, and benchmark values are compared to references. Later in Section 4.2.2 a Couette flow configuration that presents a temperature gradient in the vertical direction is studied and compared to an analytical solution. Additionally the numerical accuracy of the solver is shown and compared to calculations using a SIMPLE-type algorithm. Later in Section 4.2.3 a heated square cavity configuration is studied to assess the solver's ability to simulate steady state flow configurations of variable density in closed systems. In Section 4.2.4 the flow over a heated cylinder is studied, which serves as a test for unsteady calculations of non-isothermal systems. Finally in Section 4.2.5 a classical Rayleigh-Bénard convection system is treated, showing the behaviour of the solver for instable systems.

### 4.2.1 Heated backward-facing step

As an extension to the previous casem the backward-facing step configuration in a non-isothermal configuration is studied, where the bottom wall is heated to a constant temperature.

In this section the configuration for a heated backward-facing step proposed in Xie and Xi, 2016 is solved. The fluid entering the system has a temperature equal to  $\hat{T}_0 = 283$  K and the bottom wall is set to a constant temperature of  $\hat{T}_1 = 313$  K. The inlet temperature is used as the reference temperature, obtaining  $T_0 = 1.0$  and  $T_1 = 1.106$ . In the work of Xie and Xi, 2016 results are reported for the local Nusselt numbers and the local friction coefficients  $f_d$  along

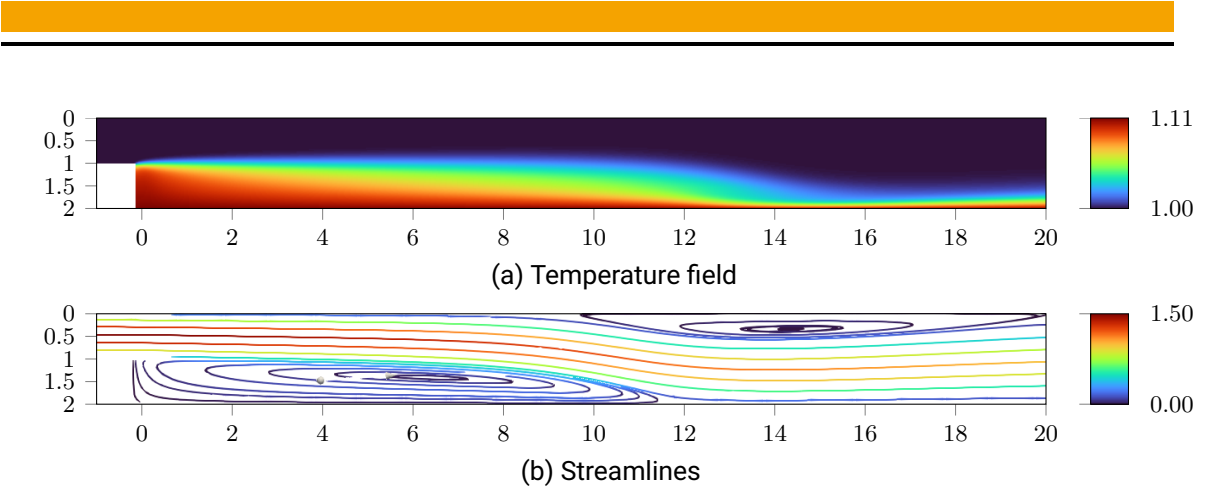


**Figure 4.8:** Temperature profile and streamlines corresponding to the backward-facing Step configuration for  $\text{Re} = 400$  and an expansion ratio of two.

the bottom wall ( $y = 0$ ) for different expansion ratios and Reynolds numbers. By combining the definition of the Nusselt number ( $\text{Nu} = \hat{h}\hat{L}/\hat{\lambda}$ ), Newton's law of cooling ( $\dot{\mathbf{q}} = \hat{h}(\hat{T}_0 - \hat{T}_1)$ ), and Fourier's law of heat conduction ( $\dot{\mathbf{q}} = \hat{\lambda}\hat{\nabla}\hat{T}$ ) a expression for the local Nusselt number is obtained.

$$\text{Nu}_{\text{loc}} = \frac{\hat{L}}{\hat{T}_0 - \hat{T}_1} \hat{\nabla}\hat{T} \cdot \hat{\mathbf{n}} \quad (4.3)$$

where  $\hat{L}$  is the reference length.  $\hat{L} = \hat{S}$  is chosen to be consistent with the definition of the Reynolds number of the reference. Furthermore, the local friction factor can be written as

$$f_d = \frac{8\hat{\nu}}{(\hat{U}_{\text{mean}})^2} \hat{\nabla}\hat{u} \cdot \hat{\mathbf{n}} \quad (4.4)$$

Simulations were conducted for different Reynolds numbers and expansion ratios. In Figure 4.8 the temperature field and the streamlines corresponding to a calculation with  $\text{Re} = 700$  are shown. Here, the apparition of the secondary vortex is seen in the top wall. Note that only a small part of the computational domain is shown. Far away from the step, a lightly skewed parabolic velocity profile is obtained, which is influenced by the density variations on the vertical direction.

For this range of temperature differences, the temperature profile is just influenced by conductive effects, since no appreciable natural convection phenomena appears. For larger temperature differences, Rayleigh-Bénard type instabilities would appear in the flow. This type of system will be treated later in Section 4.2.5.

It should be noted here that the results obtained using the XNSEC-solver are substantially different from those reported by Xie and Xi, 2016, and will not be shown here. However, in the work of Hennink, 2022 the same is also reported, stating that with his method it was not possible to reproduce the results presented by Xie and Xi, 2016.

In Figure 4.9 the local friction factor and local Nusselt number along the wall  $y = 0$  are plotted for  $\text{Re} = 700$  and  $\text{ER} = 2$ . Comparing the results from the XNSEC-solver with those reported in Hennink, 2022 a very good agreement can be observed. With this test it is possible to confirm that the XNSEC solver is able to deal with complex systems where heat transfer is present. However, for the range of temperature differences involved in this case, the variation of physical parameters such as density, viscosity and thermal conductivity with respect to

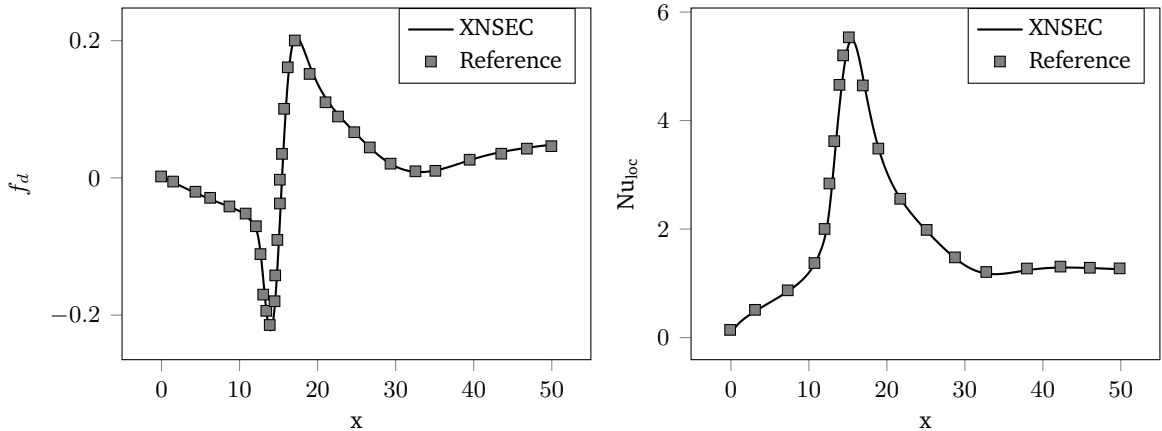


**Figure 4.9:** Local friction factor and local Nusselt number along the bottom wall for  $\text{Re} = 700$  and an expansion ratio of two. The solid lines corresponds to our solution and the marks to the reference (Hennink, 2022)

temperature has no appreciable influence on the simulated flow fields. The next two test-cases will show how the XNSEC-solver is able to simulate low-Mach number flows with a considerable temperature difference.

#### 4.2.2 Couette flow with vertical temperature gradient

As a further test case for the low-Mach solver, a Couette flow with a vertical temperature gradient is considered. This configuration was already studied in Klein et al., 2016, where the SIMPLE algorithm was used in an DG framework for the solution of the governing equations. In this section, the results from said publication are reproduced by using the XNSEC-solver, which features a fully coupled algorithm, in contrast to the SIMPLE solver, which solves the system in a segregated way. Additionally, it will be shown how the implemented solver performs in relation to the SIMPLE based solver in terms of runtime.

#### Set-up

In Figure 4.10 a schematic representation of the test case is shown. The domain is chosen as  $\Omega = [0, 1] \times [0, 1]$ , and Dirichlet boundary conditions are used for all boundaries. The upper wall corresponds to a moving wall ( $u = 1$ ) with a fixed temperature  $T = T_h$ . The bottom wall is static ( $u = 0$ ) and has a constant temperature  $T = T_c$ . Additionally, the system is subjected to a gravitational field, where the gravity vector only has a component in the  $y$  direction. Under these conditions, the  $x$ -component of velocity, pressure, and temperature are only dependent on the  $y$  coordinate, that is,  $u = u(y)$ ,  $T = T(y)$  and  $p = p(y)$ . The governing equations

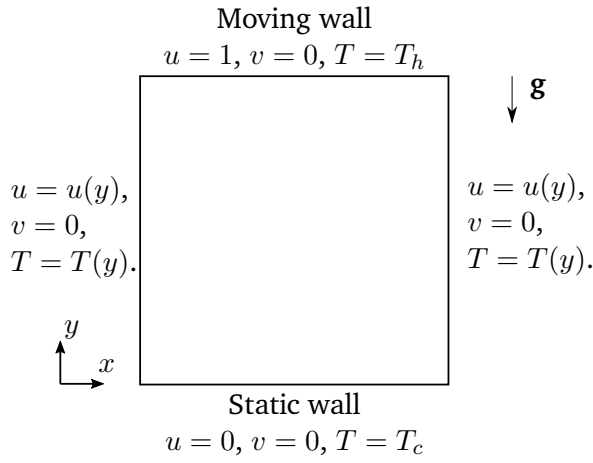


**Figure 4.10:** Schematic representation of the Couette flow with temperature difference test case.

(Equation (2.1)) reduce to

$$\frac{1}{\text{Re}} \frac{\partial}{\partial y} \left( \mu \frac{\partial u}{\partial y} \right) = 0, \quad (4.5a)$$

$$\frac{\partial p}{\partial y} = -\frac{\rho}{\text{Fr}^2}, \quad (4.5b)$$

$$\frac{1}{\text{Re} \text{Pr}} \frac{\partial}{\partial y} \left( \lambda \frac{\partial T}{\partial y} \right) = 0. \quad (4.5c)$$

By assuming a temperature dependence of the transport properties according to a Power Law ( $\mu = \lambda = T^{2/3}$ ) it is possible to find an analytical solution for this problem.

$$u(y) = C_1 + C_2 \left( y + \frac{T_c^{5/3}}{T_h^{5/3} - T_c^{5/3}} \right)^{3/5}, \quad (4.6a)$$

$$p(y) = -\frac{5p_0}{2\text{Fr}^2} \frac{\left( y \left( T_h^{5/3} - T_c^{5/3} \right) + T_c^{5/3} \right)^{2/5}}{\left( T_h^{5/3} - T_c^{5/3} \right)} + C, \quad (4.6b)$$

$$T(y) = \left( C_3 - \frac{5}{3} C_4 y \right)^{3/5}. \quad (4.6c)$$

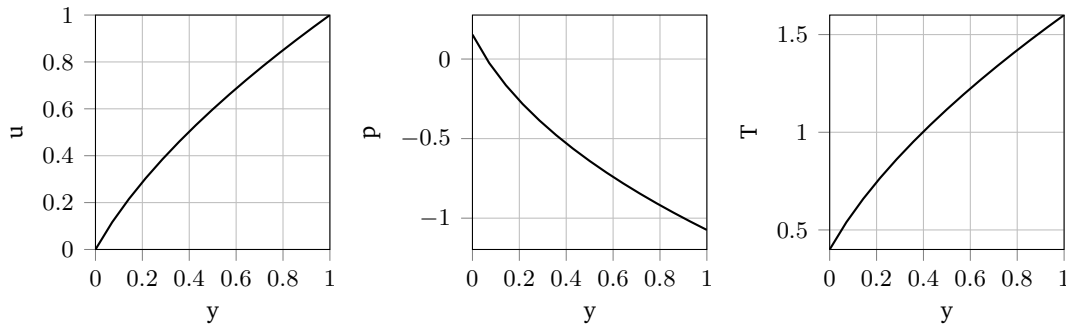


**Figure 4.11:** Solution of the Couette flow with vertical temperature gradient using a Power-Law.

Where the constants  $C_1$ ,  $C_2$ ,  $C_3$  and  $C_4$  are determined using the boundary conditions on the upper and lower walls and are given by

$$C_1 = \frac{\left(\frac{T_c^{5/3}}{T_h^{5/3} - T_c^{5/3}}\right)^{3/5}}{\left(\frac{T_c^{5/3}}{T_h^{5/3} - T_c^{5/3}}\right)^{3/5} - \left(\frac{T_h^{5/3}}{T_h^{5/3} - T_c^{5/3}}\right)^{3/5}} \quad (4.7a)$$

$$C_2 = \frac{1}{\left(\frac{T_h^{5/3}}{T_h^{5/3} - T_c^{5/3}}\right)^{3/5} - \left(\frac{T_c^{5/3}}{T_h^{5/3} - T_c^{5/3}}\right)^{3/5}} \quad (4.7b)$$

$$C_3 = T_c^{5/3}, \quad (4.7c)$$

$$C_4 = \frac{3}{5} \left( T_c^{5/3} - T_h^{5/3} \right) \quad (4.7d)$$

and  $C$  is a real-valued constant determined by an arbitrary zero level for the pressure. The dimensionless parameters are set as  $\text{Re} = 10$  and  $\text{Pr} = 0.71$ ,  $T_h = 1.6$ , and  $T_c = 0.4$  for all calculations. The system is considered open and  $p_0 = 1.0$ . The Froude number is calculated as

$$\text{Fr} = \left( \frac{2\text{Pr}(T_h - T_c)}{(T_h + T_c)} \right)^{1/2}. \quad (4.8)$$

A derivation for Equation (4.8) will be given in Section 4.2.3. In Figure 4.11 the solutions for the velocity, pressure and temperature are shown. The results are for a mesh with  $26 \times 26$  elements and a polynomial degree of three for  $u$  and  $T$ , and a polynomial degree of two for  $p$ . The vertical velocity  $v$  is zero everywhere.

### **h-convergence study**

The convergence properties of the DG method for this nonisothermal system were studied using the analytical solution described before. The domain is discretized and solved in uniform Cartesian meshes with  $16 \times 16$ ,  $32 \times 32$ ,  $64 \times 64$  and  $128 \times 128$  elements. The polynomial degrees for the velocity and temperature are changed from one to four and for the pressure from zero to three. The convergence criterion described in Section 3.2.2 was used for all calculations. The analytical solutions given by Equation (4.6) are used as Dirichlet boundary conditions on

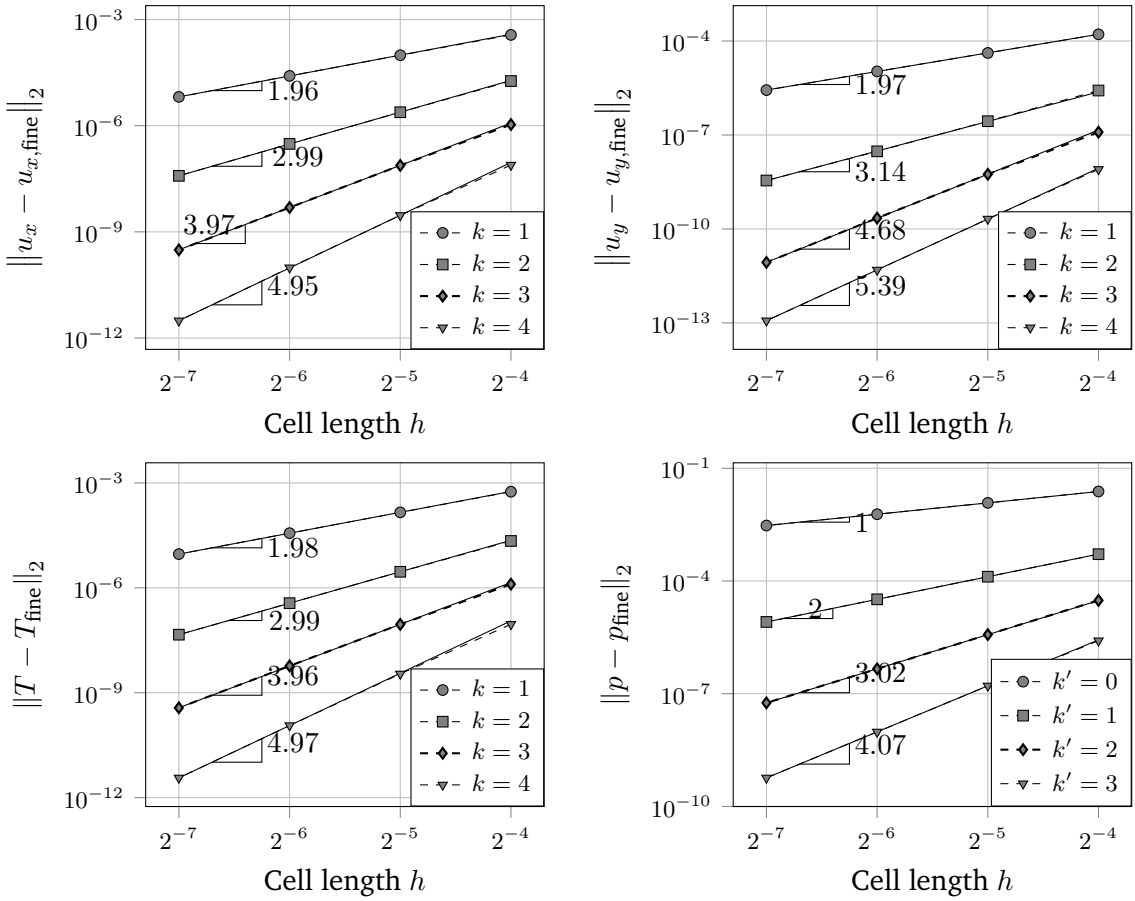


**Figure 4.12:** Convergence study of the Couette-flow with temperature difference. A power-law is used for the transport parameters.

all the boundaries of the domain. The global error is calculated against the analytical solution using a  $L^2$  norm. In Figure 4.12 the results of the h-convergence study are shown. Recall that, for increasing polynomial order, the expected order of convergence is given by the slope of the line curve when cell length and errors are presented in a log-log plot. Due to the mixed-order formulation used, the slopes should be equal to  $k$  for the pressure and equal to  $k + 1$  for all other variables. It is observed that the expected convergence rates are reached for all variables.

### Comparison with SIMPLE

As mentioned before, a solver for solving low-Mach number flows based on the SIMPLE algorithm (presented in Klein et al., 2016) has already been developed and implemented within the BoSSS framework. Although the solver was validated and shown to be useful for a wide variety of test cases, there were also disadvantages inherent to the SIMPLE algorithm. For example, within the solution algorithm, Picard-type iterations are used to search for a solution. This usually requires some prior knowledge from the user in order to select suitable relaxation factor values that provide stability to the algorithm, but at the same time do not slow down the computation substantially. The intention of this subsection is to show a comparison of

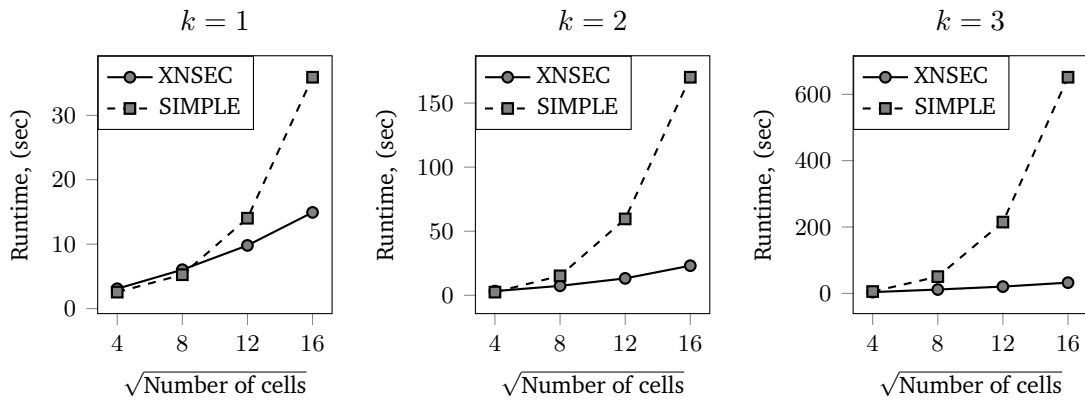


**Table 4.2:** Runtime comparison of the DG-SIMPLE solver and the XNSEC-solver for the Couette flow with vertical temperature gradient

runtimes of the calculation of the Couette flow with vertical temperature gradient between the DG-SIMPLE algorithm (Klein et al., 2016) and the XNSEC-solver. Calculations were performed on uniform Cartesian meshes with  $16 \times 16$ ,  $32 \times 32$ ,  $64 \times 64$  and  $128 \times 128$  elements, and with varying polynomial degrees between one and three for the velocity and temperature, and between zero and two for the pressure. All calculations were initialized with a zero velocity and pressure field, and with a temperature equal to one in the whole domain. The calculations were performed single-core and the convergence criteria is set to  $10^{-8}$  for both solvers. The under-relaxation factors for the SIMPLE algorithm were set for all calculations to 0.8, 0.5 and 1.0 for the velocity, pressure and temperature, respectively.

In figure Table 4.2 a comparison of the runtimes from both solvers is shown. It is clearly appreciated how the runtimes of the SIMPLE algorithm are higher for almost all of the cases studied. Obviously the under-relaxation parameters of the SIMPLE algorithm have an influence on the calculation times and an appropriate selection of them could decrease the runtimes. This is a clear disadvantage because the selection of adequate factors is highly problem dependent and requires some previous expertise from the user. On the other hand, the globalized Newton method used by the XNSEC-solver avoid this problem by using a more sophisticated method and heuristics in order to find a better path to the solution.

### 4.2.3 Differentially heated cavity problem

The differentially heated cavity problem is a classical benchmark case that is often used to assess the ability of numerical codes to simulate variable density flows (Pailiere et al., 2000; Vierendeels et al., 2003; Tyliszczak, 2014). The test case has the particularity that deals with a closed system, where the thermodynamic pressure  $p_0$  is a parameter that must be adjusted so that the mass is conserved. The thermodynamic pressure  $p_0$  determines the density field, which in turn appears in the momentum equation and the energy equation, making it necessary to use an adequate algorithm to solve the system. This point presents a special difficulty for the solution, since the calculation of  $p_0$  requires knowledge of the temperature field on the whole computational domain, inducing a global coupling of the variables.

The system is a fully enclosed two-dimensional square cavity filled with fluid. A sketch of the problem is shown in Figure 4.13. The left and right walls of the cavity have constant

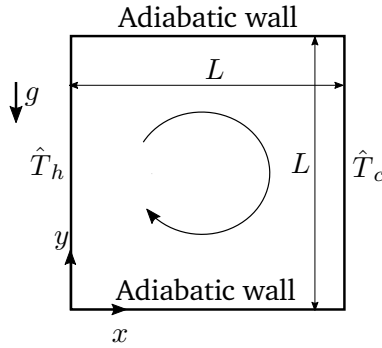


**Figure 4.13:** Schematic representation of the differentially heated cavity problem.

temperatures  $\hat{T}_h$  and  $\hat{T}_c$ , respectively, with  $\hat{T}_h > \hat{T}_c$ , and the top and bottom walls are adiabatic. A gravity field induces fluid movement because of density differences caused by the difference in temperature between the hot and cold walls. The natural convection phenomenon is characterized by the Rayleigh number, defined as

$$\text{Ra} = \text{Pr} \frac{\hat{g} \hat{\rho}_{\text{ref}}^2 (\hat{T}_h - \hat{T}_c) \hat{L}_{\text{ref}}^3}{\hat{T}_{\text{ref}} \hat{\mu}_{\text{ref}}^2}, \quad (4.9)$$

For small values of Ra, conduction dominates the heat transfer process, and a boundary layer covers the entire domain. On the other hand, large values of Ra represent a flow dominated by convection. When the number Ra increases, a thinner boundary layer is formed. Following Vierendeels et al., 2003, a reference velocity for buoyancy-driven flows can be defined as

$$\hat{u}_{\text{ref}} = \frac{\sqrt{\text{Ra}} \hat{\mu}_{\text{ref}}}{\hat{\rho}_{\text{ref}} \hat{L}_{\text{ref}}}. \quad (4.10)$$

The Rayleigh number is then related to the Reynolds number according to

$$\text{Re} = \sqrt{\text{Ra}}. \quad (4.11)$$

Thus, it is sufficient to select a Re number in the simulation, fixing the value of the Ra number. The driving temperature difference  $(\hat{T}_h - \hat{T}_c)$  appearing in Equation (4.9) can be represented as a non-dimensional parameter:

$$\varepsilon = \frac{\hat{T}_h - \hat{T}_c}{2 \hat{T}_{\text{ref}}}. \quad (4.12)$$

Using these definitions, the Froude number can be calculated as

$$\text{Fr} = \sqrt{\text{Pr} 2 \varepsilon}. \quad (4.13)$$

The results of the XNSEC solver are compared with those of the reference solution for  $\hat{T}_{\text{ref}} = 600\text{K}$  and  $\varepsilon = 0.6$ . All calculations assume a constant Prandtl number equal to 0.71. The dependence of viscosity and heat conductivity on temperature is calculated using Sutherland's law (Equation (2.29)). The non-dimensional length of the cavity is  $L = 1$ . The non-dimensional temperatures  $T_h$  and  $T_c$  are set to 1.6 and 0.4, respectively. The non-dimensional equation of state (Equation (2.26)) depends only on the temperature and reduces to

$$\rho = \frac{p_0}{T}. \quad (4.14)$$

The thermodynamic pressure  $p_0$  in a closed system must be adjusted to ensure mass conservation. For a closed system is given by

$$p_0 = \frac{\int_{\Omega} \rho_0 dV}{\int_{\Omega} \frac{1}{T} dV} = \frac{m_0}{\int_{\Omega} \frac{1}{T} dV}, \quad (4.15)$$

where  $\Omega$  represents the complete closed domain. The initial mass of the system  $m_0$  is constant and is set  $m_0 = 1.0$ . Note that the thermodynamic pressure is a parameter with a dependence on the temperature of the entire domain. This makes necessary the use of an iterative solution algorithm, so that the solution obtained respects the conservation of mass. Within the solution algorithm of the XNSEC-solver, Equation (4.15) is used to update the value of the thermodynamic pressure after each Newton iteration. The average Nusselt number is defined for a given wall  $\Gamma$  as

$$\text{Nu}_{\Gamma} = \frac{1}{T_h - T_c} \int_{\Gamma} k \frac{\partial T}{\partial x} dy. \quad (4.16)$$

---

### Comparison of results with the benchmark solution

---

Here a comparison of the results obtained with the XNSEC-solver and the results presented in the work of Vierendeels et al., 2003 is made. They solved the fully compressible Navier-Stokes equations on a stretched grid with  $1024 \times 1024$  using a finite-volume method with quadratic convergence, providing very accurate results that can be used as reference. The benchmark results are presented for  $\text{Ra} = \{10^2, 10^3, 10^4, 10^5, 10^6, 10^7\}$ . In this range of Rayleigh numbers, the problem has a steady-state solution. The cavity is represented by the domain  $[0, 1] \times [0, 1]$ . For all calculations in this subsection, the simulations are done with a polynomial degree of four for both velocity components and temperature and three for the pressure. The mesh is in an equidistant  $128 \times 128$  mesh.

Preliminary calculations showed that for cases up to  $\text{Ra} = 10^5$  the solution of the system using Newton's method presented in Section 3.2.1 is possible without further modifications, while for higher values the algorithm couldn't find a solution and stagnates after certain number of iterations. The homotopy strategy mentioned in Section 3.2 is used to overcome this problem and obtain solutions for higher Rayleigh numbers. Here, the Reynolds number is selected as the homotopy parameter and continuously increased until the desired value is reached.

In Figures 4.15 to 4.17 the temperature and velocity profiles across the cavity for different Rayleigh numbers are shown. The profiles calculated with the XNSEC-solver agree closely to the benchmark solution. As expected, an increase of the acceleration of the fluid in the vicinity of the walls for increasing Rayleigh numbers is observed.

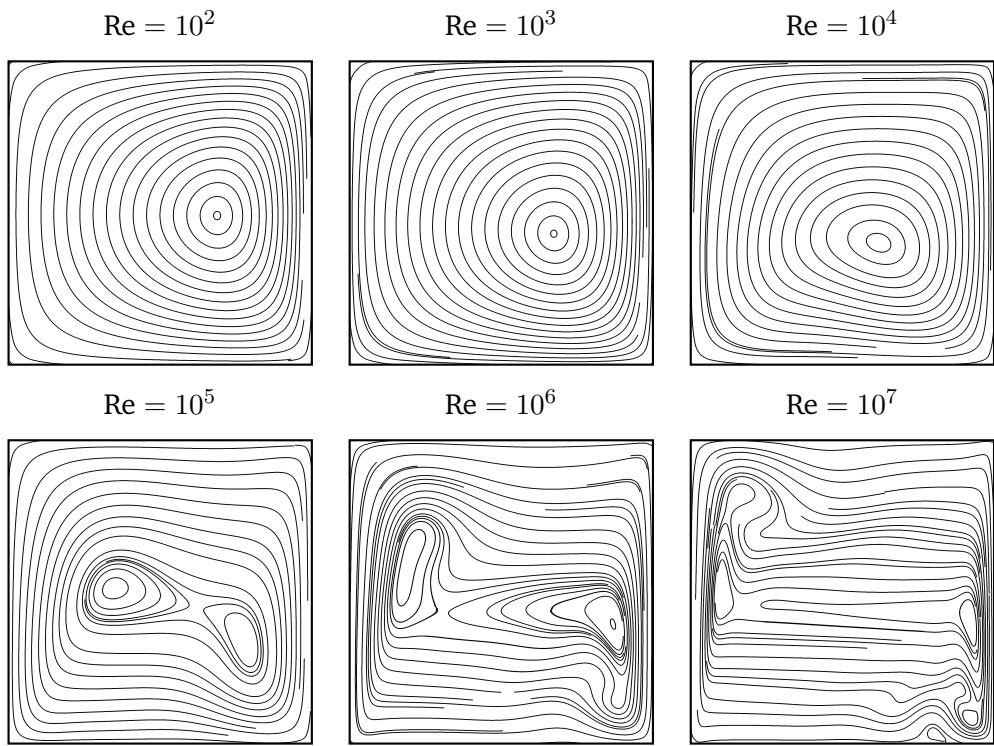


**Figure 4.14:** Streamlines of the heated cavity configuration with  $\epsilon = 0.6$ .

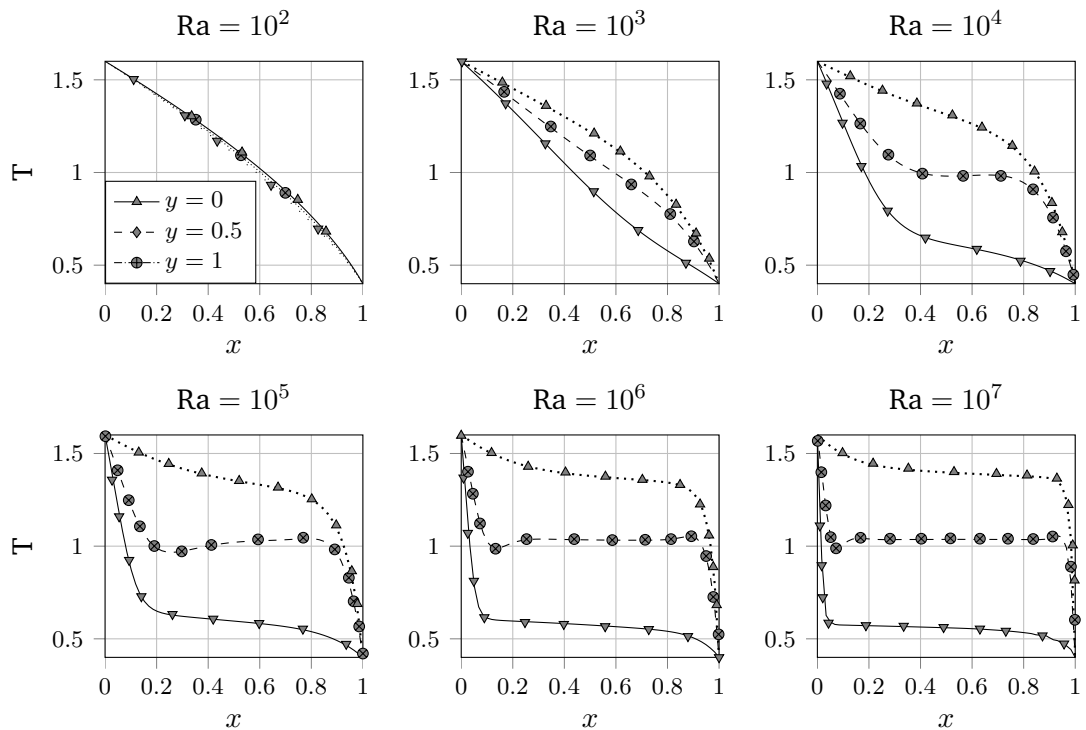


**Figure 4.15:** Temperature profiles for the differentially heated square cavity along different vertical levels. Solid lines represent the XNSEC-solver solution and marks the benchmark solution.

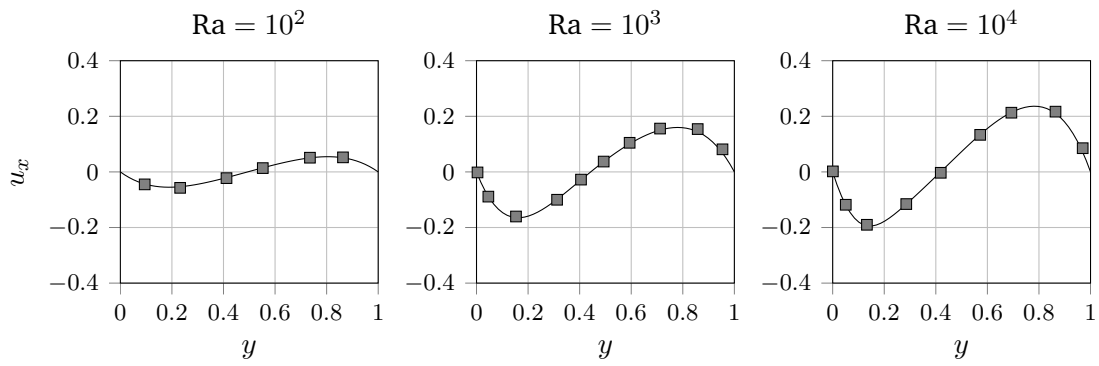


**Figure 4.16:** Profiles of the x-velocity component along the vertical line  $x = 0.5$ . Solid lines represent the XNSEC-solver solution and marks the benchmark solution.

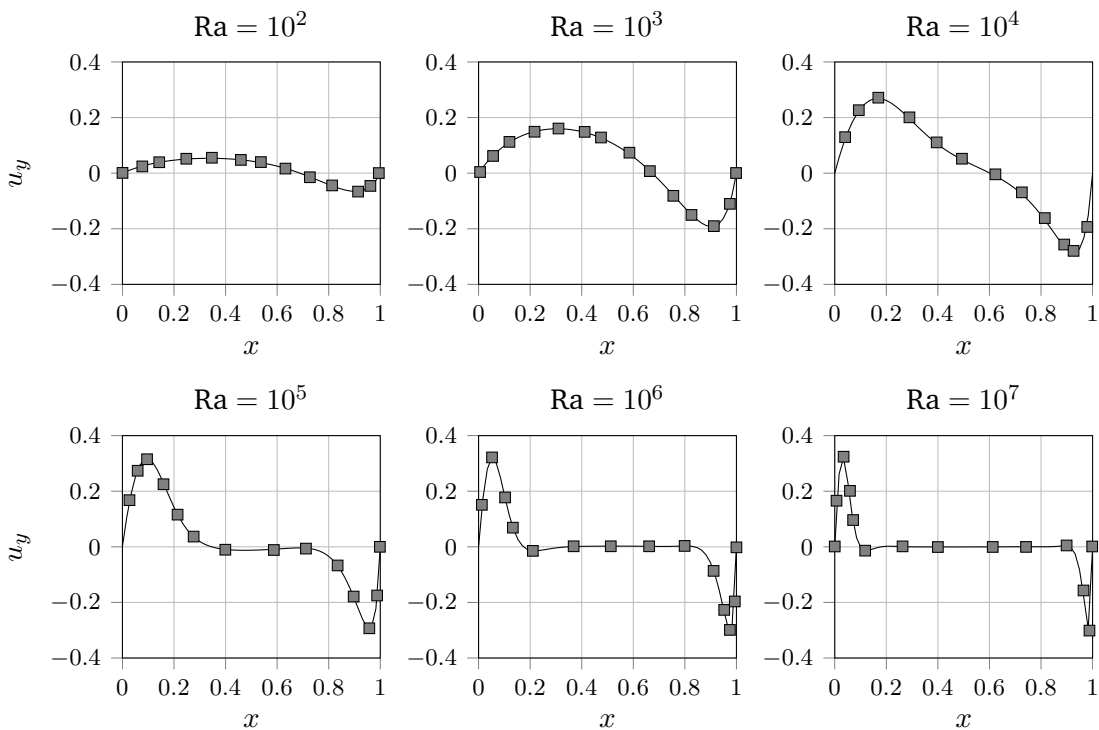


**Figure 4.17:** Profiles of the y-velocity component along the horizontal line  $y = 0.5$ . Solid lines represents the XNSEC-solver solution and marks the benchmark solution.

Rayleigh	$p_0$	$p_{0,\text{ref}}$	$\text{Nu}_h$	$\text{Nu}_c$	$\text{Nu}_{\text{ref}}$
$10^2$	0.9574	0.9573	0.9787	0.9787	0.9787
$10^3$	0.9381	0.9381	1.1077	1.1077	1.1077
$10^4$	0.9146	0.9146	2.2180	2.2174	2.2180
$10^5$	0.9220	0.9220	4.4801	4.4796	4.4800
$10^6$	0.9245	0.9245	8.6866	8.6791	8.6870
$10^7$	0.9225	0.9226	16.2411	16.1700	16.2400

**Table 4.3:** Comparison of calculated Nusselt numbers of the hot and cold wall and Thermodynamic pressure  $p_0$  reported values by Vierendeels et al., 2003 for the differentially heated cavity.

A comparison of the thermodynamic pressure and the Nusselt numbers to the benchmark solution was also made. The results are shown in Table 4.3. The thermodynamic pressure is obtained from Equation (4.15), and the average Nusselt number is calculated with Equation (4.16). The results obtained with the XSEC-solver agree very well with the reference results, as can be seen for the thermodynamic pressure, which differs at most in the fourth decimal place. Note that the average Nusselt number of the heated wall ( $\text{Nu}_h$ ) and the Nusselt number of the cold wall ( $\text{Nu}_c$ ) are different. As the Rayleigh number grows, this discrepancy becomes larger, hinting that, at such Rayleigh numbers, the mesh used is not refined enough to adequately represent the thin boundary layer and more complex flow structures appearing in high-Rayleigh number cases. While for an energy conservative system  $\text{Nu}_h$  and  $\text{Nu}_c$  should be equal, for the DG-formulation this is not the case, since conservation is only ensured locally and the global values can differ. This discrepancy can be seen as a measure of the discretization error of the DG formulation and should decrease as the mesh resolution increases. This point will be discussed in the next section.

### Convergence study

An  $h$ -convergence study of the XSEC solver was conducted using the heated cavity configuration. Calculations were performed for polynomial degrees  $k = 1, 2, 3, 4$  and equidistant regular meshes with, respectively,  $8 \times 8$ ,  $16 \times 16$ ,  $32 \times 32$ ,  $64 \times 64$ ,  $128 \times 128$  and  $256 \times 256$  elements. The  $L^2$ -Norm was used to calculate errors against the solution in the finest mesh. The results of the  $h$ -convergence study for varying polynomial orders  $k$  are shown in Figure 4.18. It is observed how the convergence rates scale approximately as  $k + 1$ . Interestingly, for  $k = 2$  the rates are higher than expected. On the other hand, some degeneration is observed in convergence rates for  $k = 4$ . This strange behavior can be explained if one considers that the heated cavity presents a singular behavior at the corners -similar to the problem previously exposed for the lid-driven cavity -, which causes global pollution in the convergence behavior of the algorithm.

As discussed in the previous section, the difference in the average values of the Nusselt number on the hot wall  $\text{Nu}_h$  and the cold wall  $\text{Nu}_c$  is a direct consequence of the spatial discretization error and should decrease for finer meshes. In Figure 4.19 the convergence behavior of the Nusselt number is presented for different polynomial degrees  $k$ , different number of elements and for two different Ra numbers. As expected, it can be observed that this discrepancy is smaller when a larger number of elements is used. It can also be seen that  $\text{Nu}_h$  reaches the expected solution of cells for a much smaller number of elements. This can

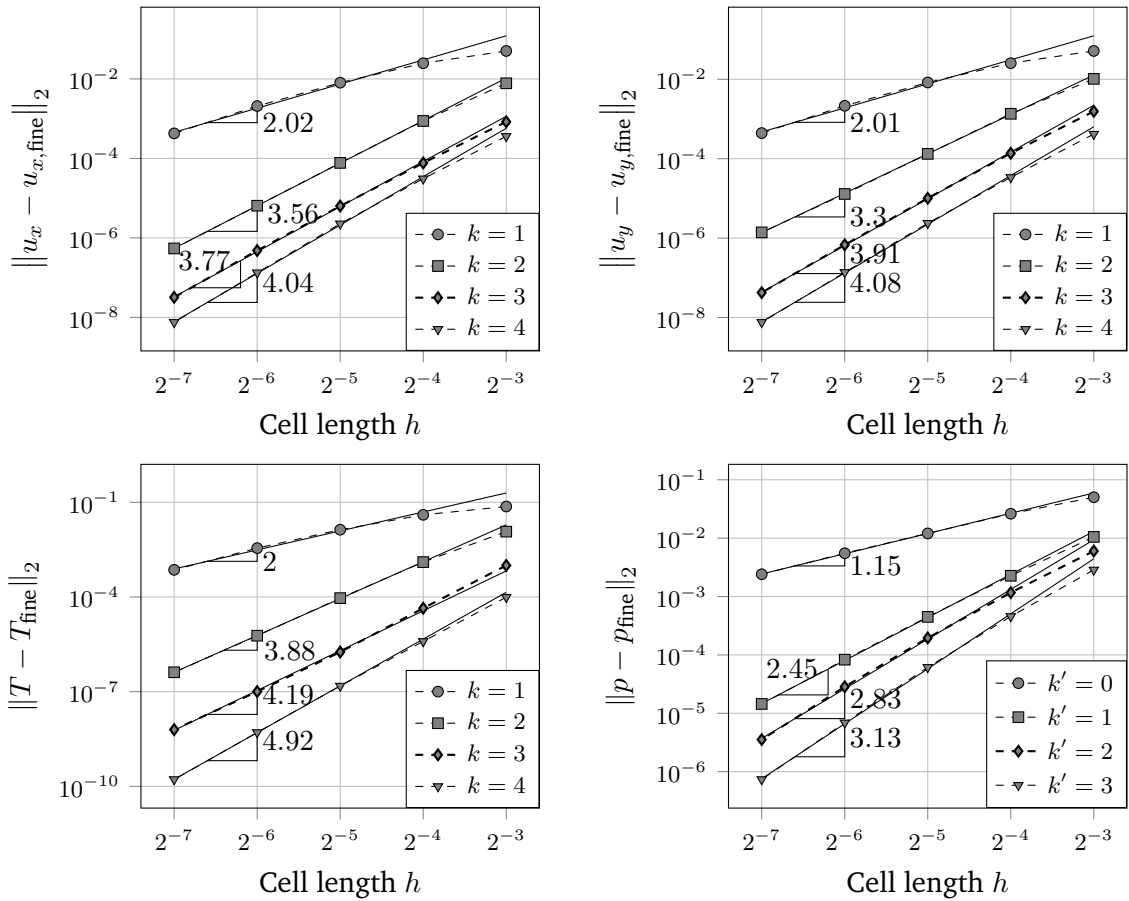


**Figure 4.18:** Convergence study of the differentially heated cavity problem for  $\text{Ra} = 10^3$ .

be explained if one thinks that more complex phenomena take place near the cold wall (see Figure 4.14), which makes necessary a finer mesh resolution in that area.

The results presented in this section allow us to conclude that the implemented solver is capable of dealing with flows with variable densities, and in particular in closed spaces. Additionally, it was observed that even for this complex test, convergence properties close to those expected from the DG-method are obtained. In this section only systems with a steady state solution were treated. In the next section the ability of the solver to compute flows with varying densities in non-steady state will be shown.

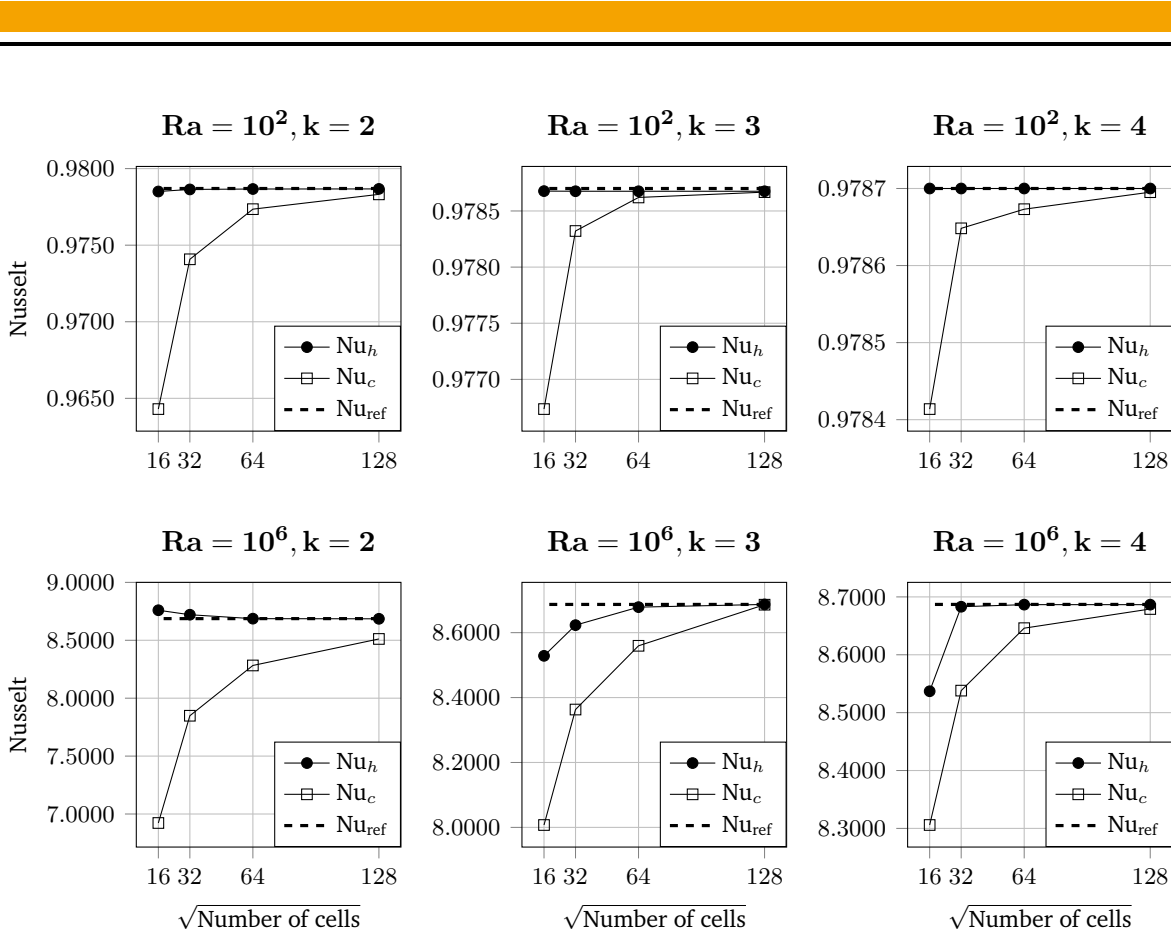


**Figure 4.19:** Nusselt numbers calculated with Equation (4.16) at the hot wall ( $\text{Nu}_h$ ) and the cold wall ( $\text{Nu}_c$ ) for different number of cells and polynomial order  $k$ . The reference values from Vierendeels et al., 2003 are shown with dashed lines.

#### 4.2.4 Flow over a circular cylinder

A further test case of the XNSEC solver is the simulation of flow over a circular cylinder. The results shown section are based on the work by Miao, 2022

The simulation of a 2D flow over an obstacle exhibits different flow states depending on the Reynolds number. For low Reynolds numbers the flow is laminar and stationary. When the Reynolds number reaches a critical value, the flow becomes non-stationary and eventually turbulent. In particular, for  $50 \leq \text{Re} \leq 160$  the behavior of the fluid is laminar with an unstationary periodic character, and the well-known vortex shedding phenomenon appears (Sharma and Eswaran, 2004). In this section the ability of the XNSEC-solver for dealing with isothermal and non-isothermal unsteady flow will be assessed.

#### Set-up

Figure 4.20 shows the geometry of the problem. In the center of the domain is located a heated cylinder of diameter  $d = 1$ , which is subjected to a flow of constant velocity magnitude. The size of the computational domain is chosen as  $D = 59d$ , which is large enough so that the outlet boundary conditions have no influence on the solution. The left half of the boundaries of the

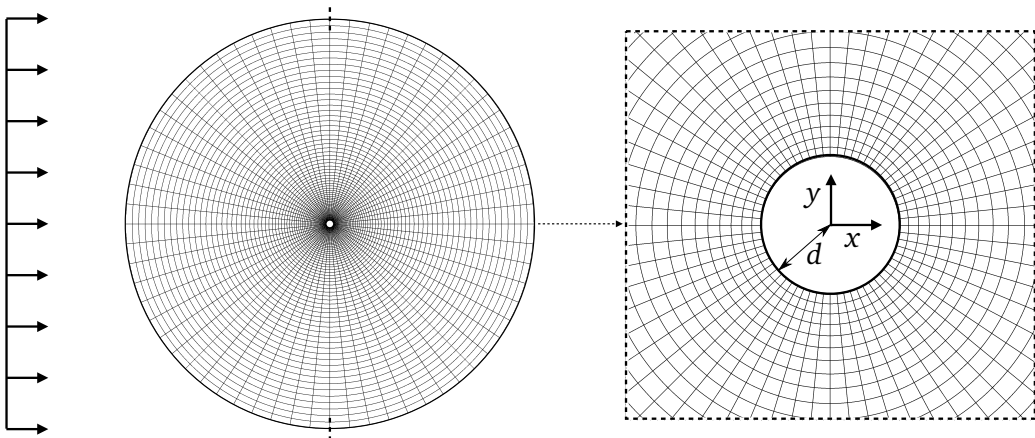


**Figure 4.20:** Schematic representation of the heated circular cylinder.

computational domain correspond to a velocity inlet with constant velocity  $(u, v) = (1, 0)$  and temperature  $T = T_\infty$ . The right half of the domain corresponds to a pressure outlet. Finally, the boundary condition corresponding to the heated cylinder is no-slip wall, with a constant temperature  $T = T_h$ . The system is an open system, and the thermodynamic pressure has a constant value set to  $p_0 = 1$ .

A reference temperature of  $\hat{T}_{\text{ref}} = 298.15 \text{ K}$  is taken. The conditions for the velocity inlet are for the isothermal case a dimensionless temperature of  $T_h = 1.0$  and  $T_\infty = 1$ , while for the non-isothermal  $T_h = 1.5$  and  $T_\infty = 1.0$ . A Reynolds number of 100 is used, for which the flow is unsteady and periodic. Gravity effects are taken as negligible. The prandtl number has a constant value of  $\text{Pr} = 0.71$  and the heat capacity ratio  $\gamma = 1.4$ . The transport parameters are calculated with Sutherlands law which is given by Equation (2.29) and the equation of state for the density is Equation (2.26).

6A polynomial degree of order three is used for both velocity components and the temperature, and two for pressure. In this simulations a curved mesh consisting of 64 elements in the radial direction, and 64 elements in the angular direction is used. The use of a curved mesh for this problem was done primarily to adequately represent the geometry of the heated cylinder . Another possibility could have been to use a method such as a Immersed Boundary Method, but it is beyond the scope of this work.

One point to note regarding the use of curved meshes within the DG-method (and in all High-order methods), is that special care has to be taken in the representation of curved elements (Bassi and Rebay, 1997) in order to use correctly quadrature rules. This is critical to preserve the convergence properties of DG-methods. In particular, since the highest degree of the polynomials used in this simulation is three, elements of the bi-cubic type are used, where 16 nodes are used per element for the discretization for a two-dimensional element. Moreover, the time discretization is performed with a BDF-3 scheme , and the time derivative of the continuity equation is calculated with a second order backward difference scheme (see Section 3.1.3). The simulation time corresponds to  $t = 100$ , and constant timesteps of  $\Delta t = 0.2$

are used. The initial conditions are

$$u(t=0) = 1 + u^{\text{vortex}}, \quad (4.17\text{a})$$

$$v(t=0) = 0 + v^{\text{vortex}}, \quad (4.17\text{b})$$

$$T(t=0) = 1, \quad (4.17\text{c})$$

$$p(t=0) = 0. \quad (4.17\text{d})$$

Here,  $u^{\text{vortex}}$  and  $v^{\text{vortex}}$  are the velocity component of a vortex field of radius  $r$  and central point  $(x^o, y^o)$  defined by

$$u^{\text{vortex}}(x, y) = \begin{cases} -a(y - y^0) & \text{if } \sqrt{(x - x^0)^2 + (y - y^0)^2} \leq r \\ 0 & \text{if } \sqrt{(x - x^0)^2 + (y - y^0)^2} > r \end{cases} \quad (4.18\text{a})$$

$$v^{\text{vortex}}(x, y) = \begin{cases} a(x - x^0) & \text{if } \sqrt{(x - x^0)^2 + (y - y^0)^2} \leq r \\ 0 & \text{if } \sqrt{(x - x^0)^2 + (y - y^0)^2} > r \end{cases} \quad (4.18\text{b})$$

where  $a$  corresponds to the vortex force. The reason for placing a vortex in the initial conditions is to include a perturbation on the system which triggers the vortex shedding phenomenon. The vortex moves with the flow and is eventually advected from the calculation domain. Specifically for this simulation a vortex of radius  $r = 1$  and strength  $a = 1$  is placed at  $(x^o, y^o) = (2, 0)$ . It is worth mentioning that the inclusion of the vortex in the initial conditions is not imperative to make the vortex shedding phenomenon emerge, but it is a way to accelerate its appearance. For the range of Reynolds numbers mentioned, even instabilities of the numerical method should be enough to make the phenomenon arise, but in a much slower way.

In the next sections a validation of the results will be shown. For this, the variables lift coefficient  $C_L$ , drag coefficient  $C_D$ , Strouhal number  $\text{St}$ , and Nusselt number  $\text{Nu}$  are calculated and compared with reference results. These characteristic quantities are defined as

$$C_L = \frac{2F_L}{\rho_\infty u_\infty^2 d} \quad (4.19)$$

$$C_D = \frac{2F_D}{\rho_\infty u_\infty^2 d} \quad (4.20)$$

$$\text{St} = \frac{f d}{u_\infty} \quad (4.21)$$

$$\text{Nu} = \frac{d}{\Delta T} \frac{1}{\|\partial S\|_{\text{leb}}} \oint_{\partial S} \nabla T \cdot \mathbf{n} dS \quad (4.22)$$

$F_L$  and  $F_D$  are the lift and drag force respectively,  $f$  is the vortex shedding frequency and  $\|\text{leb}\| = \pi d$  is the circumference of the cylinder.

---

### Isothermal case.

---

The isothermal case results are compared with the work of Sharma and Eswaran, 2004. They reported results for the case  $\text{Re} = 100$  and  $T_h = T_\infty$ . The Strouhal number and average drag coefficient calculated with the XNSEC-solver are  $\text{St} = 0.1639$  and  $C_{D,\text{avg}} = 1.3103$ , while the reference values  $\text{St} = 0.164$  and  $C_{D,\text{avg}} = 1.3183$ , which means a error of less than a 0.6% on both quantities. Its worth noting that preliminar calculations with a implicit Euler scheme for the discretization of the temporal terms didnt cause the vortex shedding phenomenom to appear, making necesary a BDF-3 scheme.

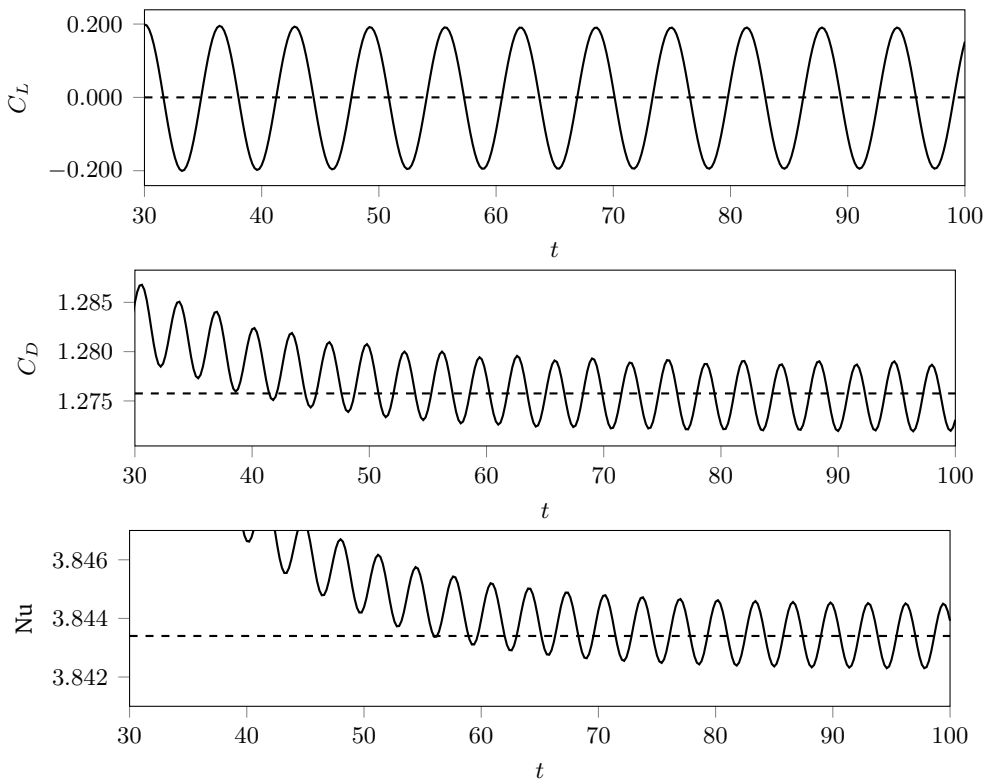


**Figure 4.21:** Temporal evolution of average Nusselt number, lift coefficient and drag coefficient of the heated cylinder

---

#### Non-isothermal case.

A comparison of the calculation results for the non-isothermal case was performed based on the results reported in Shi et al., 2004, Wang et al., 2000 and Hennink, 2022. The temporal evolution of the characteristic quantities  $C_D$ ,  $C_L$  and  $\text{Nu}$  is shown in Figure 4.21. The results agree very good with the references. The average Nusselt number is  $\text{Nu} = 3.8434$ , while the reference value from Hennink, 2022 is  $\text{Nu} = 3.804$ , which corresponds to a difference of 1.04%. The Strouhal number is  $\text{St} = 0.1538$  and the references report values of  $\text{St} = 0.152$  and  $\text{St} = 0.1536$ , a difference of approximately 1%. It is possible then to conclude that the XNSEC-solver allows to simulate adequately unsteady non-isothermal flows, where the fluid properties do present a scalar dependence (in this case, on the temperature). It is important to note that the temperature variation in this test-case causes only a moderate variation in the density. As will be seen later, the temporal term appearing in the continuity equation is problematic in the case of larger density differences (Knijker, 2011), as it is a cause of numerical instabilities.

---

#### 4.2.5 Rayleigh-Bénard Convection

The Rayleigh-Bénard convection is a configuration similar to the heated cavity presented in the last section, as the flow is also induced by buoyancy effects. The configuration consists of a fluid located between two horizontal plates maintained at different temperatures, with the lower temperature being higher than the upper temperature. It is known that under a

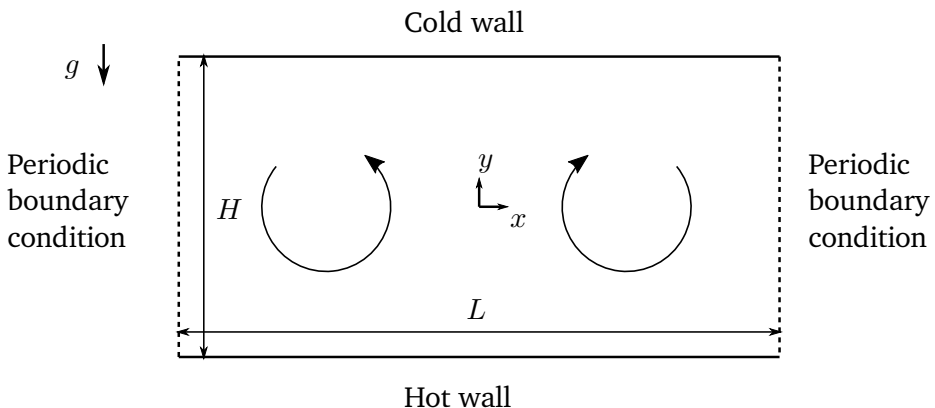


**Figure 4.22:** Geometry of the Rayleigh-Bénard convection problem. Convection rolls are sketched

certain Rayleigh number the flow presents a macroscopically stable behavior and the heat is simply transferred by conductive phenomena. When the Rayleigh number exceeds a certain critical value  $\text{Ra}_{\text{crit}}$ , the system becomes unstable, which causes a perturbation of the system to give rise to fluid motion, creating the so-called convection cells, also usually referred to as Bénard cells.

In the following sections two aspects of this situation will be discussed by making use of different type of boundary conditions on the sides. First in Section 4.2.5 periodic boundary conditions are used, which allows to study a single pair of convection rolls and to calculate numerically the critical value  $\text{Ra}_{\text{crit}}$ , which is compared with theoretical values. Subsequently, in Section 4.2.5 a transient simulation of this configuration is performed by using pressure-outlet boundary conditions. The results shown section are based on the work by Miao, 2022

### Periodic boundary conditions

In this section the fluid behavior will be analyzed by studying a system where a single convection-cell appears. As mentioned above, the nature of the governing equations gives rise to a complex behavior of the system. Making use of the linear stability theory for the governing equations under the Boussinesq assumption, it is possible to determine that for a system with rigid boundaries the critical Rayleigh number is  $\text{Ra}_{\text{crit}} = 1707.762$  (Chandrasekhar, 1961). Moreover, the wave number is  $a_c = 3.117$ , which implies that the convective rolls develop at an aspect ratio of  $2\pi/a_c = 2.016$ . For the simulations presented in this section an aspect ratio of  $L/H = 2$  is used, as is done by Kao and Yang, 2007. The geometry and boundary conditions of the analyzed problem can be found in Figure 4.22. The upper wall corresponds to a no-slip wall that is maintained at a constant temperature  $T_c$ . Similarly, the bottom wall is also a no-slip wall with a temperature  $T_h$ , with  $T_h > T_c$ . The boundary conditions on the left and right of the computational domain are periodic boundary conditions. Gravity has only one component in the negative direction of  $y$ .

For the range of Rayleigh numbers treated here, the simulations are treated as steady state simulations. For all simulations in this section a regular Cartesian grid consisting of  $32 \times 64$  cells, with dimensionless lengths  $L = 2$  and  $H = 1$  was used. The polynomial degree of both velocity components and temperature is four, and for pressure it is three. An open system is assumed, and  $p_0 = 1.0$  throughout the simulation.

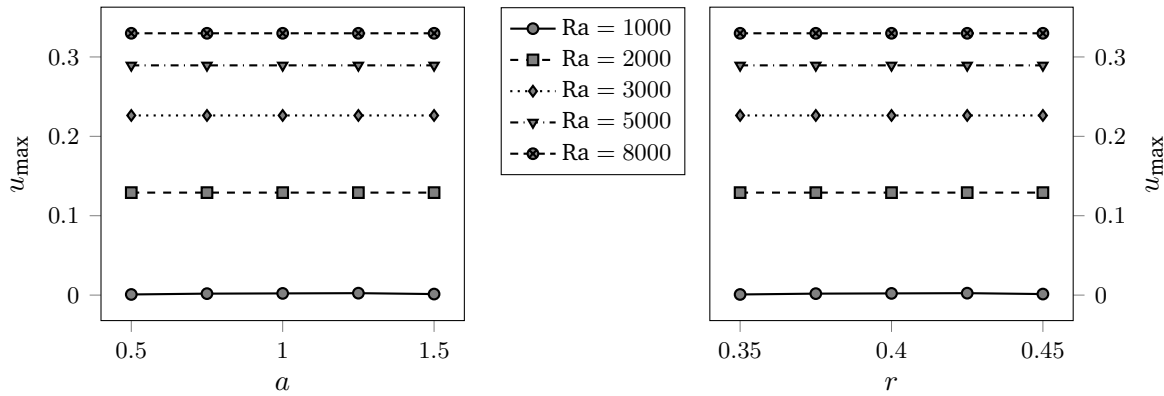


**Figure 4.23:** Maximum x-velocity in the Rayleigh-Bénard convection configuration for different  $a$  and  $r$ .

First, the stability of the XNSEC-solver will be studied by determining the critical value  $\text{Ra}_{\text{crit}}$ . As mentioned above, the theoretical value  $\text{Ra}_{\text{crit}} = 1707.762$  was determined using the Boussinesq assumption in the governing equations. This implies that the variation of densities within the system must be sufficiently small. For this reason, an analysis is performed for a dimensionless temperature difference  $\epsilon = (T_h - T_c)/(T_h + T_c) = 0.0001$ , This implies that the variation of densities within the system must be sufficiently small. For this reason, an analysis is performed for a dimensionless temperature difference  $T_h = 1.0001$  and  $T_c = 0.9999$ . The reference temperature is chosen as  $\hat{T}_{\text{ref}} = 600$  K. Since the XNSEC-solver is based on the low-Mach equation set, this choice of low temperature difference allows to compare the present results with those obtained analytically using the bousinesq approximation. The definition of the dimensionless numbers as well as the reference velocity are exactly the same as those mentioned in Section 4.2.3. The transport coefficients are calculated with Sutherlands Law.

Similarly to the case exposed in Section 4.2.4, velocity fields are initialized with vortices, which play the role within the simulation of a trigger for the inherent instabilities of the problem. In particular, two vortices with opposite directions of rotation are added. The velocity components of these are again given by equations Equation (4.18) and Equation (4.18). The coordinates of the first vortex are  $(x^o, y^o) = (-0.5, 0)$  and it has a strength  $a = 1$  and a radius  $r = 0.4$ . For the second vortex  $(x^o, y^o) = (0.5, 0)$ ,  $a = -1$  and  $r = 0.4$ . The initial conditions are

$$u(t=0) = 1 + u^{\text{vortex-left}} + u^{\text{vortex-right}}, \quad (4.23a)$$

$$v(t=0) = 0 + v^{\text{vortex-left}} + v^{\text{vortex-right}}, \quad (4.23b)$$

$$T(t=0) = 1, \quad (4.23c)$$

$$p(t=0) = -\frac{\rho y}{\text{Fr}^2}. \quad (4.23d)$$

It is of importance to mention that the initialization of the solver without the vortices leads the solver to a stationary solution where there is no fluid motion. Clearly, this is a solution of the equations, but, as already mentioned, it is an unstable solution.

First, a study was performed to demonstrate the independence of the steady-state solution from the chosen initial conditions. This is demonstrated in Figure 4.23, where it is shown for a given Rayleigh number the maximum velocity obtained inside the system, varying the strength  $a$  or the radius  $r$  of the vortices. It is also apparent that the case  $\text{Ra} = 1000$  does not exhibit a

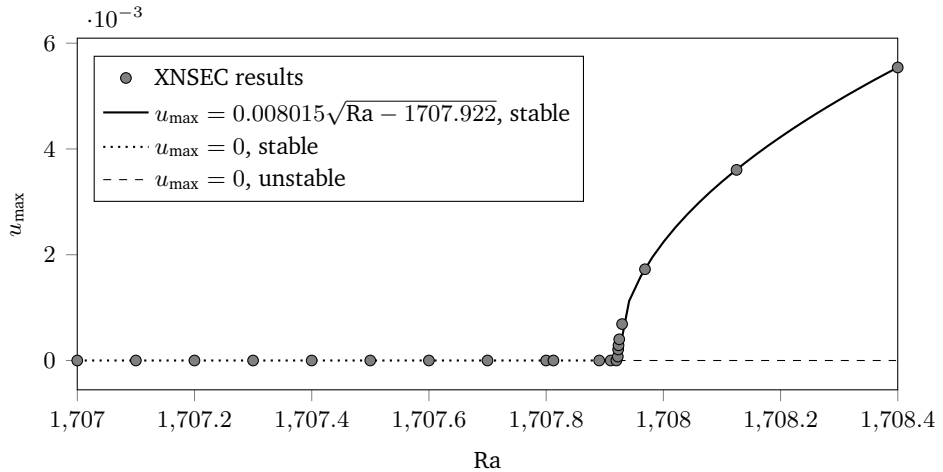


**Figure 4.24:** Stability behaviour of the Rayleigh-Bénard convection with  $\epsilon = 0.0001$ .

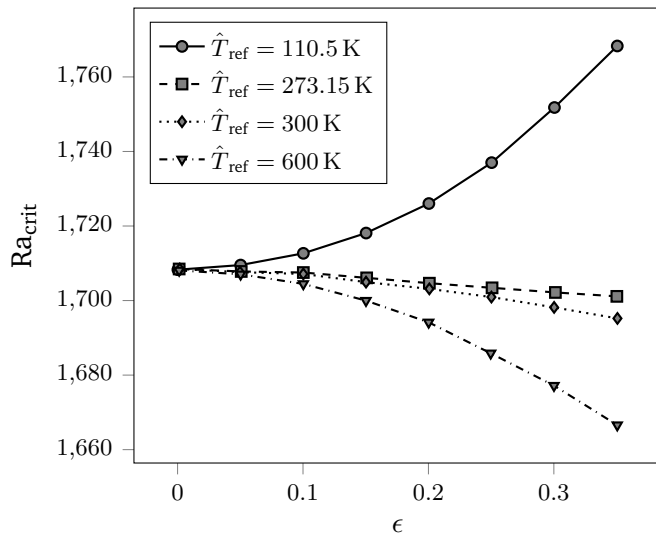


**Figure 4.25:** Critical Rayleigh number at different temperatures and different reference temperatures.

macroscopic fluid motion, while  $\text{Ra} = 2000$  does. This points to the fact that the critical value is effectively in this range.

Subsequently, a series of simulations were performed with  $a = 0.5$  y  $r = 0.4$ , in which a bisection algorithm was used to find the critical value, obtaining  $\text{Ra} = 1707.922$ , as shown in Figure 4.24. Compared to the theoretical value  $\text{Ra} = 1707.762$ , it presents a difference of only 0.009%. In addition, the proportionality  $u \propto \sqrt{\text{Ra} - \text{Ra}_{\text{Ra}}}$  that is expected by analytical arguments is also fulfilled, obtaining in particular  $u_{\text{max}} = 0.008015\sqrt{\text{Ra} - 1707.922}$ . It is possible to conclude that at least for small temperature differences, the low-Mach approximation has a similar behavior to the equations with the bousinesq approximation.

In relation to the above, it is interesting to analyze the influence of the temperature difference within the system with respect to the critical Rayleigh value. This is demonstrated in Figure 4.25, where the calculation is done for different values of the reference temperature. Clearly, for low  $\epsilon$  the critical value is very close to the theoretical value obtained under the Bousinesq approximation. As  $\epsilon$  increases, a larger deviation becomes apparent. This can be attributed

---

to the dependence of the viscosity, thermal conductivity, and density coefficients on the temperature.

Finally, in Figure 4.26 and Figure 4.27 the temperature fields and streamlines obtained with the XNSEC-solver for  $\epsilon = 0.5$  and  $\hat{T}_{\text{ref}} = 600 \text{ K}$  for different Rayleigh number are shown. An interesting point to mention is the difference between the results obtained using the Boussinesq and the low-Mach approximation. Comparing the results reported here with publications that use the Boussinesq approximation ( Shishkina, 2021; Zhou et al., 2004), a clear difference in the streamlines is observed. In particular, the centers of the streamlines obtained with the low-Mach solver are slightly shifted towards the colder zones, while the streamlines obtained with the Boussinesq approximation do not present this deviation and remain close to the center. A possible explanation for this is that with the Boussinesq approximation the expansion effects of the fluid are ignored, whereas in the low-Mach equations this is not the case. When the latter is used, the hot fluid moves the center of the streamline towards the cold fluid.

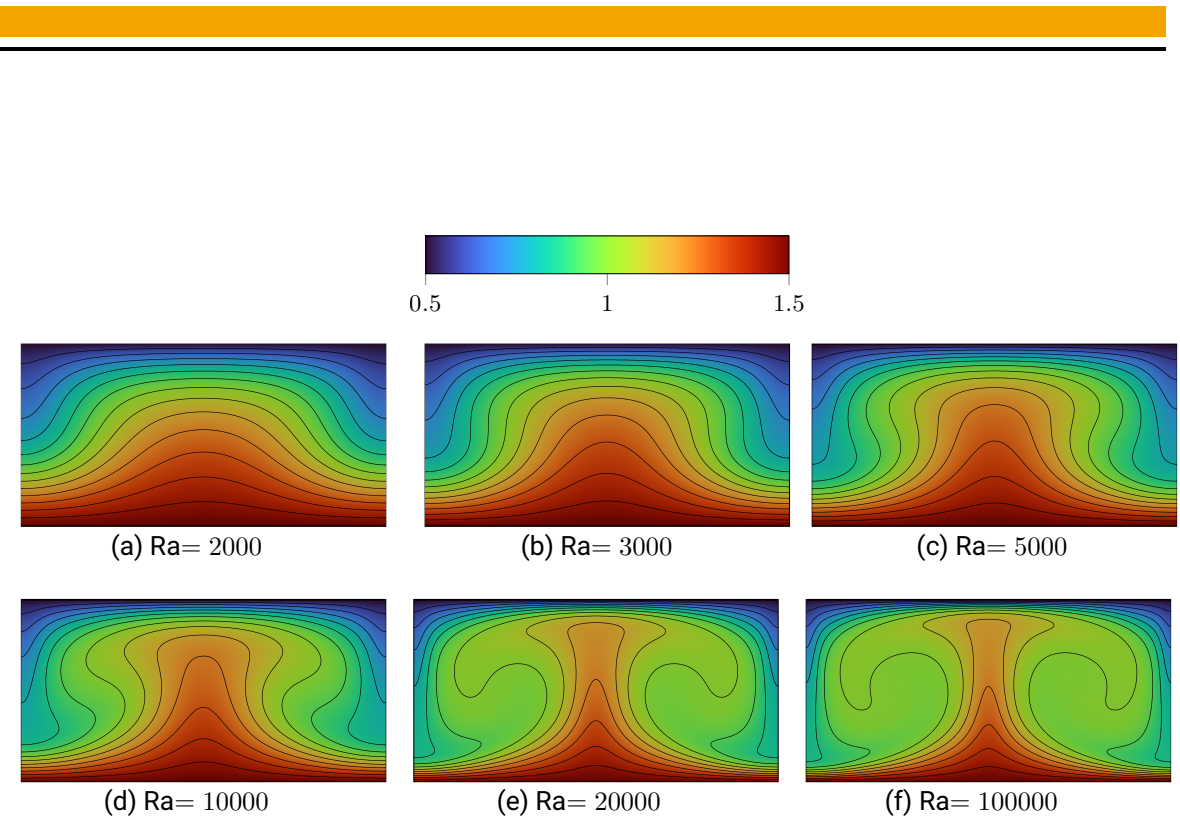


**Figure 4.26:** Temperature field and contours of a Rayleigh-Bénard convection roll

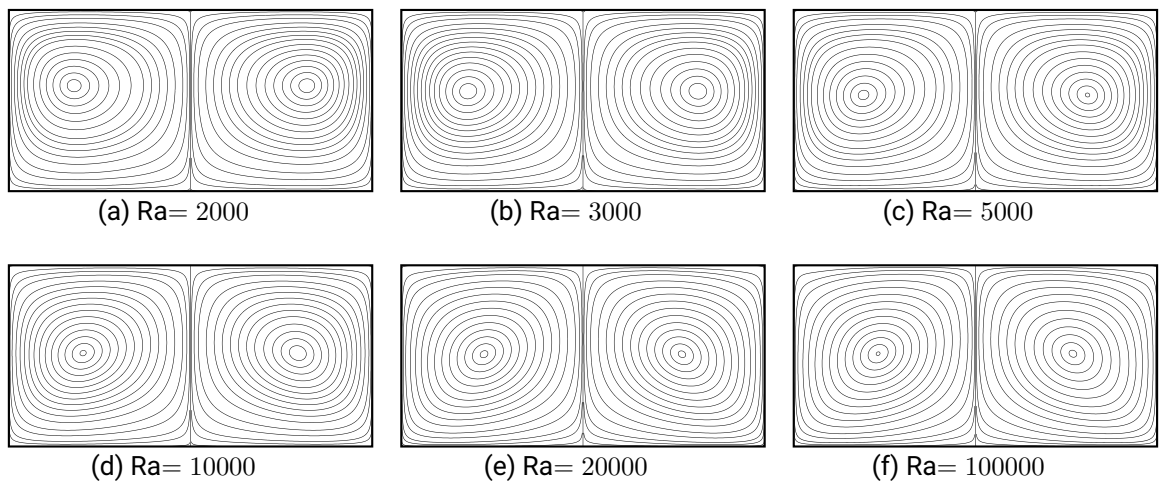


**Figure 4.27:** Streamlines of a Rayleigh-Bénard convection roll

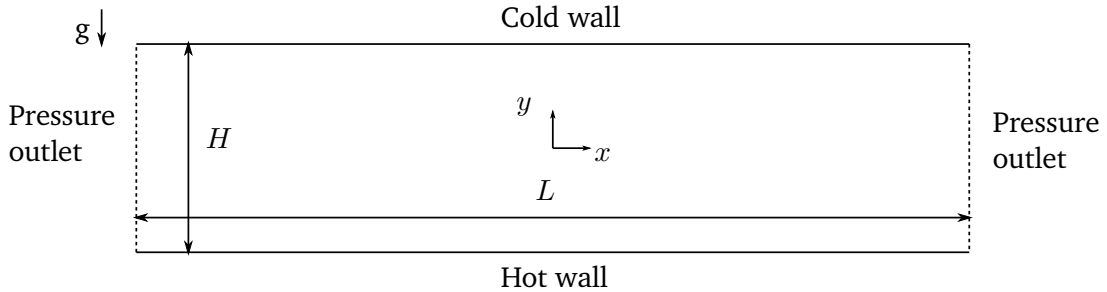


**Figure 4.28:** Geometry of the Rayleigh-Bénard convection with pressure outlet boundary conditions.

### Pressure outlet boundary condition

A transient calculation of the Rayleigh-Bénard configuration is shown in this subsection. The configuration is similar to the one described in the last subsection. A sketch showing the system is shown in Figure 4.28. The difference is that the barriers to the left and right are now considered pressure outlet boundary conditions and the length  $L$  of the system is chosen considerably longer. Theoretically, if the interest of the simulation is focused on the study of the behavior of convection rolls, an infinitely long system should be used to avoid the influence of the boundary condition. The adimensional lengths are chosen as  $H = 1$  and  $L = 10$ . A grid with  $32 \times 320$  cells is used. The polynomial degrees for the velocity components and temperature are set to four, and for the hydrodynamic pressure is three. The time discretization is again done with a BDF-3 scheme and the calculation time is 150, using timesteps of  $\Delta t = 0.5$ . The temperatures are set to  $T_h = 1.5$  and  $T_c = 0.5$ , with a reference temperature of  $\hat{T}_{\text{ref}} = 600$  K. The Rayleigh number is  $\text{Ra} = 5659$ . The initial conditions are chosen as

$$u(t = 0) = 0, \quad (4.24a)$$

$$v(t = 0) = 0, \quad (4.24b)$$

$$T(t = 0) = 1, \quad (4.24c)$$

$$p(t = 0) = -\frac{\rho y}{\text{Fr}^2}. \quad (4.24d)$$

Note that a resting fluid was given as an initial condition, as it was observed that the pressure outlet boundary condition introduce a sort of perturbation to the system, which triggers the movement of the fluid. Initially the vortices will appear close to the left and right boundaries, and start gradually filling the whole domain, reaching finally a steady solution, which can be seen in Figure 4.29. Clearly in the center of the domain (far away from the outlet boundary conditions), the structure of the solution is very similar to the ones shown in the last subsection. In fact, if the domain length is chosen sufficiently large, they are equal.

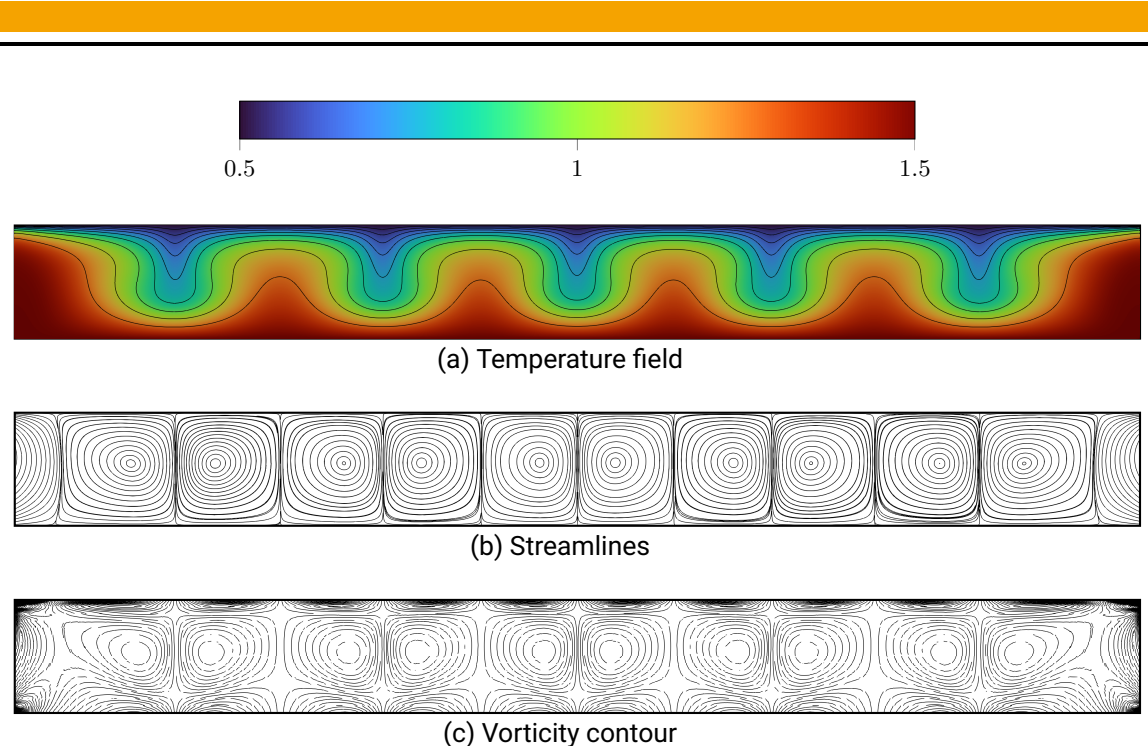


**Figure 4.29:** Temperature, streamlines and vorticity of the Rayleigh-Bénard flow with pressure outlets.

### 4.3 Multi-component non-isothermal cases

In this section, test cases for combustion applications will be shown. For all the cases treated here, the solution of the flame sheet problem described in ?? is calculated first. Subsequently, this solution is used as an initial estimate for the solution of the finite chemistry rate problem (c.f. Section 2.1.2). In Section 4.3.1 a co-flow laminar diffusion flame configuration is calculated and some remarks about the convergence of the solving algorithm of the XSEC-solver using this case are done. Next in Section 4.3.2 a diffusion flame in a counterflow configuration is simulated and validated by comparing it with results from a one-dimensional configuration. Finally in Section 4.3.3 a pseudo-one-dimensional diffusion flame configuration is used to show the convergence ratios of the fully coupled solver. In all the test cases presented in this section, a smoothing parameter  $\sigma = 0.02$  was used (cf. ??). Furthermore, methane combustion according to the one-step model shown in ?? is considered, therefore, the relevant chemical components are  $\text{CH}_4$ ,  $\text{O}_2$ ,  $\text{CO}_2$ ,  $\text{H}_2\text{O}$  and  $\text{N}_2$ , thus  $N = 5$  and  $\mathbf{Y}' = (Y_{\text{CH}_4}, Y_{\text{O}_2}, Y_{\text{CO}_2}, Y_{\text{H}_2\text{O}})$ . The nitrogen mass fraction  $Y_{\text{N}_2}$  is calculated according to Equation (2.23).

#### 4.3.1 Co-flow laminar diffusion flame

The co-flowing flame configuration is used as a first test to assess the behavior of the solver for reactive flows applications. It basically consists of two concentric ducts that emit fuel and oxidant into the system, creating a flame. This configuration has been widely studied. In the seminal work of Burke and Schumann, 1928 analytical expressions for the flame height and flame shape are obtained by studying a very simplified problem (constant density and velocity field, infinitely fast chemistry, among others). Later, Smooke and Giovangigli, 1992 and later works solved this configuration using a 2D-axisymmetric system and also used the flame sheet estimates to find adequate initial conditions for their Newton algorithm. It should be noted

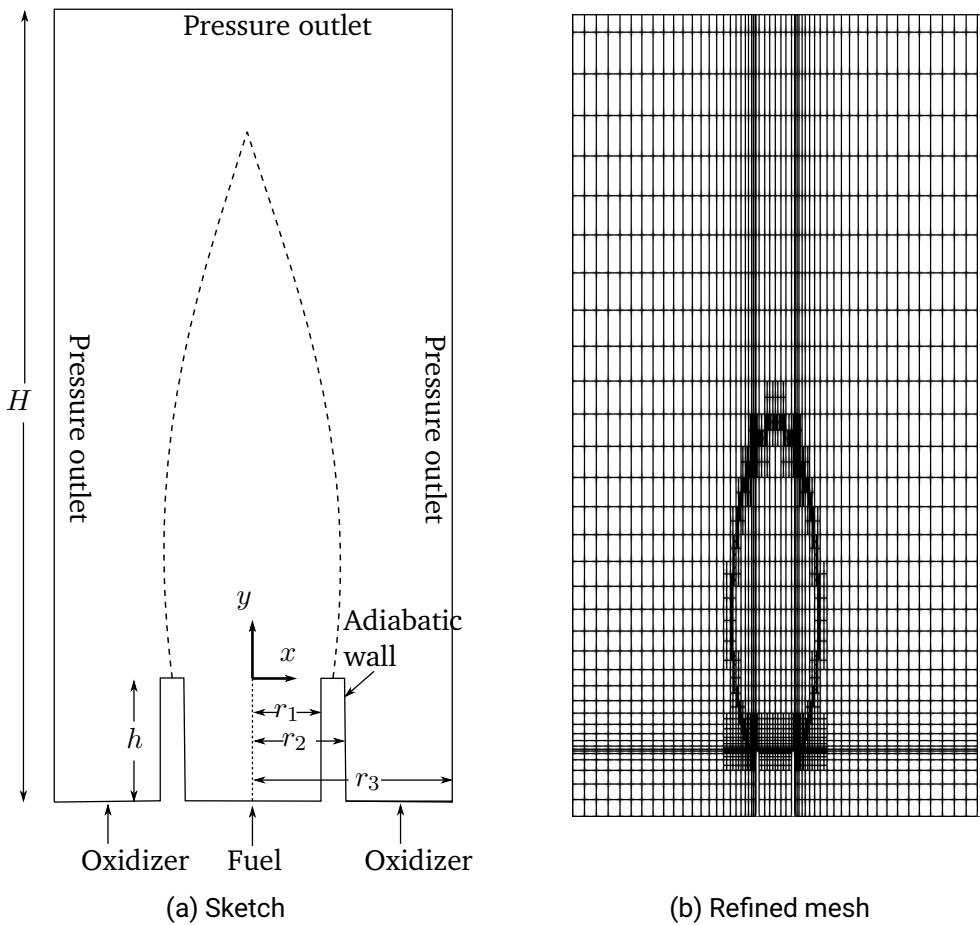


**Figure 4.30:** Geometry of a coflowing flame configuration (not to scale).

that the solution of the axisymmetric system of equations presents numerical difficulties that are not the main concern of the present work. For this reason, it was decided to solve a system with similar characteristics but which is possible to represent in Cartesian coordinates. This is possible if an infinitely long slot burner is considered.

### Set-up of the slot coflowing flame configuration

A schematic diagram of the configuration can be seen in Figure 4.30a, and consists of a fuel inlet with two oxygen inlets on its sides. Note that the system also includes the tips that separate both oxidizer and fuel inlets. The inclusion of this separation was seen to be necessary to be able to obtain a converged solution. Although the system is clearly symmetric around the axis  $x = 0$ , no symmetry assumption is made and the whole domain is considered for the simulation. The lengths depicted on Figure 4.30a are set as  $r_1 = 0.635$  cm,  $r_2 = 0.762$  cm, and  $r_3 = 7.747$  cm. Additionally  $h = 2.54$  cm and  $H = 40$  cm. The lengths  $r_3$  and  $L$  are set with arbitrarily large values in order to avoid influence on the outer boundary conditions on the solution of the flame zone. Setting a higher value of  $r_3$  or  $L$  did not significantly affect the results. The inlet boundary conditions are set as:

- Oxidizer inlet:  $\{\forall(x, y) : y = -R \wedge x \in [-X_3, -X_2] \cup [X_2, X_3]\}$

$$u = 0, \quad v = v_O, \quad T = T^O, \quad \mathbf{Y}' = (0, Y_{O_2}^O, 0, 0)$$

- Fuel Inlet:  $\{\forall(x, y) : y = -R \wedge x \in [-X_1, X_1]\}$

$$u = 0, \quad v = v_F(x), \quad T = T^F, \quad \mathbf{Y}' = (Y_{CH_4}^F, 0, 0, 0)$$

The oxidizer enters the system as a plug flow with a constant velocity of  $v_O = 4.1 \text{ cm s}^{-1}$ . The inlet velocity of the fuel stream  $v_F$  is a parabolic profile given by

$$v_F(x) = \left[ 1 - \left( \frac{x}{X_1} \right)^2 \right] v_m^F \quad (4.25)$$

with  $v_m^F = 2.427 \text{ cm s}^{-1}$ . The inlet temperatures of both streams is  $T^F = T^O = 300 \text{ K}$ . Combustion of diluted methane on air is considered, with  $Y_{CH_4}^F = 0.2$ ,  $Y_{N_2}^F = 0.8$ ,  $Y_{O_2}^O = 0.23$  and  $Y_{N_2}^O = 0.77$ . The superindexes  $F$  and  $O$  represent the fuel and oxidizer inlet respectively. The pressure outlet boundary condition is the same as Equation (2.36c). Finally, the boundary conditions at the tips correspond to adiabatic walls, which are defined as in Equation (2.36b), with  $\mathbf{u}_D = (0, 0)$ .

The variables are nondimensionalized in the usual way. The reference length  $\hat{L}_{\text{ref}} = \hat{r}_1$  and the reference velocity  $\hat{u}_{\text{ref}} = v_m^F$ . The reference temperature is  $\hat{T}_{\text{ref}} = T^F$ . All derived variables are nondimensionalized using the air stream as a reference condition, i.e.  $\hat{\rho}_{\text{ref}} = 1.17 \text{ kg m}^{-3}$ ,  $\hat{\mu}_{\text{ref}} = 1.85 \times 10^{-5} \text{ kg m}^{-1} \text{ s}^{-1}$ ,  $\hat{W}_{\text{ref}} = 28.82 \text{ kg kmol}^{-1}$ . This gives the non-dimensional numbers  $\text{Re} = 16.5$ ,  $\text{Da} = 4.3 \cdot 10^9$ . The Prandtl number is assumed to be constant with  $\text{Pr} = 0.71$ . The reference heat capacity is set  $\hat{c}_{p,\text{ref}} = 1.3 \text{ kJ kg}^{-1} \text{ K}^{-1}$ . Obviously the solution of a nondimensionalized system of equations should be independent of the reference values selected. Nevertheless, the choice of this value for the heat capacity is important because it gives a solution of the flame-sheet which is similar to the actual solution of the full problem. For this calculation, all Lewis numbers are set to unity. Gravity effects are not taken into account. The transport parameters are calculated using Sutherland law with  $\hat{S} = 110.5 \text{ K}$ . The mixture heat capacity  $c_p$  is calculated with Equation (2.28) and using NASA polynomials for the heat capacity of each component.

## Numerical results

Numerical experiments using the XNSEC-solver showed that the solution of the problem is highly mesh-dependent. The presence of very high gradients in some areas of the problem requires a higher density of cells around these regions to obtain a well-resolved solution. For the solution of the coflow flame, a stretched base mesh is used, with smaller elements in the vicinity of the inlets and larger elements farther away from the inlets. It was observed that the complex mixing phenomena that occur in the vicinity of the inlets have a critical effect on the convergence of the solution. For this reason, a special refinement of the base mesh was necessary in the vicinity of the tips. Furthermore, an adequate mesh resolution on the areas where the flame is located is also critical. To avoid over-solving in zones where actually no reaction is taking place, an adaptive mesh refinement strategy in a pseudo-time-stepping framework was used (see Section 3.2.5). After obtaining a steady state solution, the mesh is refined and the calculation is started again. In particular, for this case, several pseudo-timesteps were performed for the flame-sheet calculation. After each of these, the mesh is refined in the

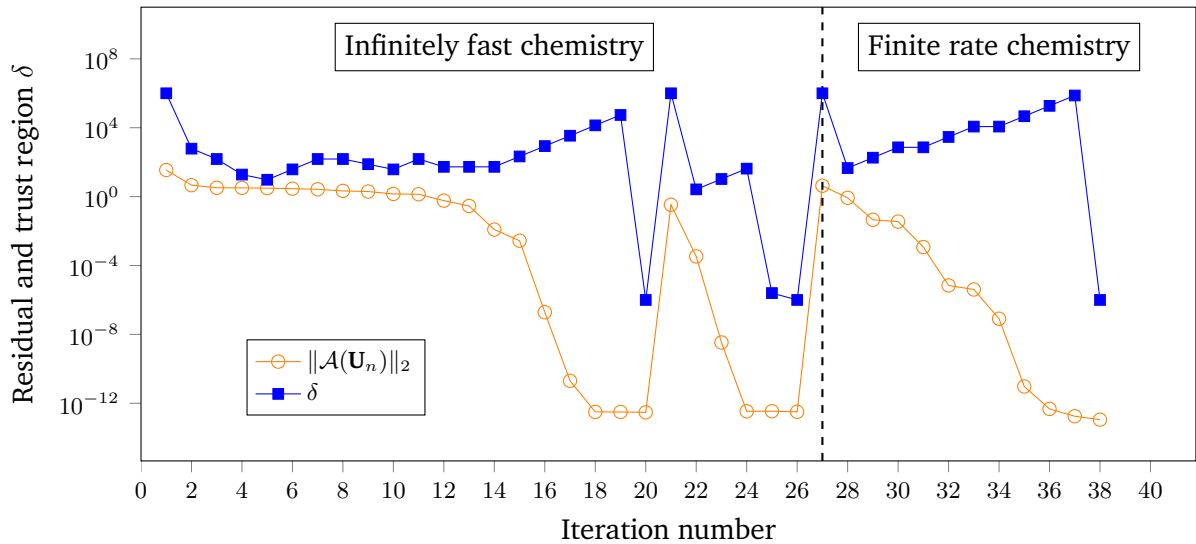


**Figure 4.31:** Typical convergence history of a diffusion flame in the coflowing flame configuration. A mesh refinement was done at iteration 21.

vicinity of the flame sheet, i.e., in the cells where  $z = z_{st}$ . In Figure 4.30b the actual mesh used for the solution of the full problem is shown. Clearly, the mentioned refinement strategy works for the cases where the Lewis number corresponds to unity and the  $c_p$  of the mixture has a constant value (assumptions made for the flame-sheet estimate). In case these conditions are not met, the solution obtained for the case with finite reaction rate will be slightly different from the flame-sheet solution. However, experiments with the XSEC-solver have shown that this refinement strategy is still beneficial for the convergence of the complete problem, but the selection of a good representative constant value for the heat capacity is important.

In Figure 4.31 the convergence history using the newton algorithm presented in Section 3.2.1 is shown. The flame-sheet calculation requires 20 Newton iterations to find a solution. It is clearly seen how the residuals  $\|\mathcal{A}(\mathbf{U}_n)\|_2$  for about the first 14 iterations decrease very slowly, while the *delta* parameter of the globalized Newton method is adapted to find an optimal value to reduce the residuals. Around iteration 13 the algorithm starts to increase *delta*, obtaining a faster reduction of the residuals and the solution to the problem is found in iteration number 20. Then mesh refinement is used, and 6 iterations are required to find a converged solution. Finally, in iteration number 27 the flame-sheet solution is used as the initial estimate for the full problem, which requires only 11 iterations to find a solution.

In Figure 4.32 solution fields of the coflow flame configuration are shown. Since for the selected inlet velocities the flame corresponds to a overventilated one, the typical jet form is observed. It can also clearly be seen from Figure 4.32c that all the fuel entering the system reacts with the oxygen. The exothermic reaction produces an acceleration on the flow field, as shown in Figure 4.32b. The maximum temperature reached corresponds to X (X Kelvin).

From this test case it is concluded that the strategy of using the flame-sheet as an initial condition presents an efficient way to obtain steady state solutions of combustion problems. Since the flame-sheet is only an estimate, it is possible to perform the calculations on relatively coarse grids, and use low order polynomial degrees. The obtained solution can be used as an estimate for calculations with higher polynomial degrees to find a more accurate solution of

the full problem in a few iterations. A disadvantage, as already mentioned, is the choice of the  $c_p$  parameter, since an inappropriate choice of it gives a solution of the flame-sheet problem far away from the solution of the full problem. However, the user's experience and access to experimental information allows estimating this value relatively easily. It is worth mentioning that the value chosen in this section ( $\hat{c}_{p,\text{ref}} = 1.3 \text{ kJ kg}^{-1} \text{ K}^{-1}$ ) served as an adequate estimate for all the simulations presented in this thesis.

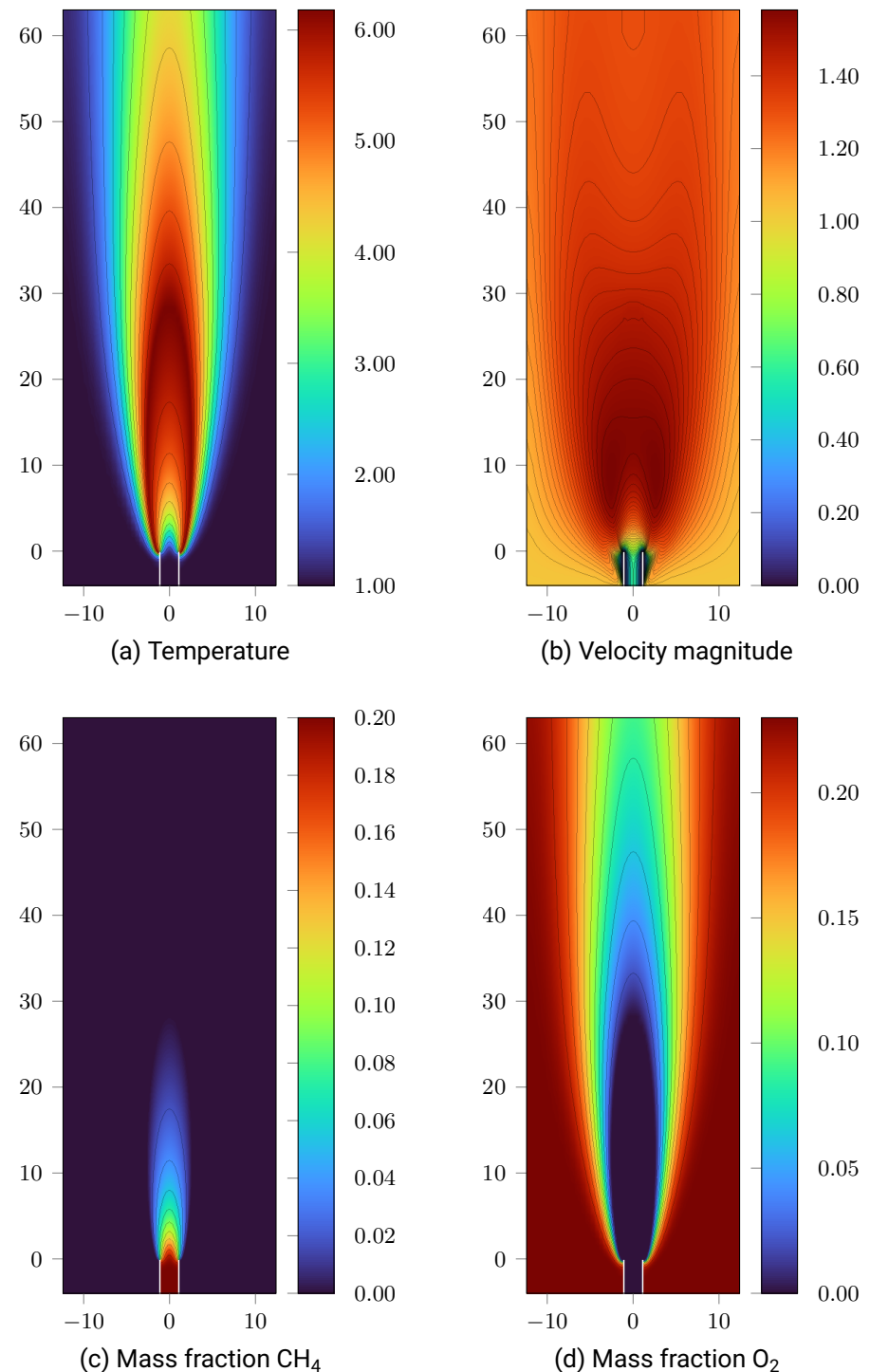


**Figure 4.32:** Solution field of a coflow flame configuration.

### 4.3.2 Counterflow diffusion flame

mencionar lo de que la malla fue manualmente creada de tal forma que la zona central tiene mas elementos The counterflow diffusion flame is a canonical configuration used to study the structure of non-premixed flames. In its most basic configuration it consists of two oppositely situated jets. The fuel (possibly mixed with some inert component such as nitrogen) is fed into the system by one of the jets, while the other jet feeds air to the system, thereby establishing a stagnation point flow. Upon contact, the reactants produce a flame which is located in the vicinity of the stagnation plane. A diagram of the setup can be seen in Figure 4.33. This simple configuration has been subject of study for decades because it provides a simple way of creating a strained diffusion flame, which proves to be useful when studying the flame structure, extinction limits or production of pollutants of flames Pandya and Weinberg, 1964 Spalding, 1961 Keyes and Smooke, 1987. By assuming an infinite injector diameter and self-similarity of the solution, it is possible to reduce the governing equations to a one-dimensional formulation (see e.g. the textbook of Kee Kee et al., 2003). As a means of validating our implementation we compare the results with the solution of the one-dimensional self-similar problem calculated with BVP4, a fourth order finite difference boundary value problem solver provided by MATLAB.

The combustion of a methane-nitrogen mixture with air was simulated using the *BoSSS* code. The mass composition of the fuel inlet was assumed to be  $Y_{\text{CH}_4}^0 = 0.2$  and  $Y_{\text{N}_2}^0 = 0.8$ , and the oxidizer inlet corresponds to air with  $Y_{\text{O}_2}^0 = 0.23$  and  $Y_{\text{N}_2}^0 = 0.77$ . Because we are dealing with an open system, the thermodynamic pressure  $\hat{p}_0$  is constant and set to the ambient pressure of 101 325 Pa. As noted by Sung et al., Sung et al., 1995 although the form of the inlet velocity profiles does have an influence on the solution of the problem, its effect on the solution near the flame zone is rather small. Nevertheless, as mentioned before the solution of the self-similar one-dimensional problem assumed an infinite injector diameter, which implies that the upstream velocity field has to be constant. Based on this fact we set the velocity profile of both inlets as a plug flow. Following combinations of inlet velocities were calculated:

- Low inlet velocities:  $u_{\text{fuel}}^0 = 0.048 \text{ m s}^{-1}$  and  $u_{\text{oxidizer}}^0 = 0.144 \text{ m s}^{-1}$ ,
- Medium inlet velocities:  $u_{\text{fuel}}^0 = 0.12 \text{ m s}^{-1}$  and  $u_{\text{oxidizer}}^0 = 0.36 \text{ m s}^{-1}$

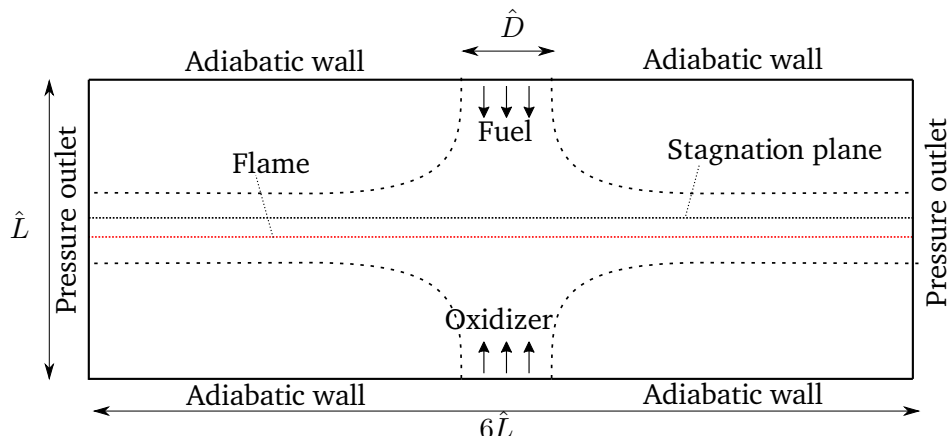


**Figure 4.33:** Schematic representation of the counterflow configuration.

- High inlet velocities:  $u_{\text{fuel}}^0 = 0.24 \text{ m s}^{-1}$  and  $u_{\text{oxidizer}}^0 = 0.72 \text{ m s}^{-1}$

By using as definition of the strain rate the maximum axial velocity gradient, the calculated strains for the three cases mentioned above are  $34 \text{ s}^{-1}$ ,  $76 \text{ s}^{-1}$  and  $155 \text{ s}^{-1}$ , respectively. The temperature of both inlets is 300 K. The separation between both jets  $\hat{L}$  is equal to 0.02 m, and the length of the inlet opening  $\hat{D}$  is 0.02 m. The left and right domain boundaries are selected to be at a distance  $3\hat{L}$  of the center. A non-unity but constant Lewis number formulation is used, with  $\text{Le}_{\text{CH}_4} = 0.97$ ,  $\text{Le}_{\text{O}_2} = 1.11$ ,  $\text{Le}_{\text{H}_2\text{O}} = 0.83$  and  $\text{Le}_{\text{CO}_2} = 1.39$ . Smooke and Giovangigli, 1991. The heat capacity of each component is evaluated locally from NASA polynomials, and the mixture heat capacity is calculated with Equation (2.28). In ?? the convergence history obtained for a typical calculation of the counter diffusion flame is presented. The solution of the flame sheet calculation requires 17 iterations until convergence is reached. The obtained solution is used as a starting value for the finite chemical rate calculation, which only needs 10 iterations until convergence is reached. We note that because the flame sheet calculation is only used as an approximation of the final solution, a low polynomial degree can be used. For the flame sheet calculation  $k = 2$  was chosen, resulting in a rather small system with 26,880 degrees of freedom. For the finite rate calculation  $k = 4$  was used, which resulted in a system with 174,110 degrees of freedom. With the above-mentioned another advantage of the approach of using the flame sheet calculation for two-dimensional simulations can be highlighted. The initial estimate can be found relatively easily for a system with few degrees of freedom. Using the solution found as the initial estimate has the consequence that Newton's algorithm for the complete problem (which has many more degrees of freedom) only needs a few iterations to find a solution. Because we are solving a two-dimensional configuration, in order to be able to compare our results with the ones obtained from the one-dimensional representation, the temperature, mass fractions and velocity profiles are extracted along the centerline of the system shown as the dashed line in Figure 4.33. In Figure 4.35 a comparison of the axial velocities calculated with BoSSS and the one-dimensional solution is shown. While for the high strain case the results agree closely, for lower strains a discrepancy is observed. Recall that the derivation of the one-dimensional approximation assumes a constant velocity field incoming to the flame zone in order to obtain a self-similar solution. In the case of the two-dimensional configuration presented here, the border effects do have an influence on the centerline, which disrupts the self-similarity. This effect is more pronounced for low velocities, which explains the discrepancy between curves. Similarly, In Figure 4.36 the temperature and mass fraction fields are presented. Again, a discrepancy is observed for low strains, but results show a good agreement for higher inlet velocities. It can also be observed how, as expected, Fernandez-tarrazo et al., 2006 at higher strains a significant penetration (leakage) of oxygen across the flame is present. Finally, in ?? the two-dimensional temperature, velocity and reaction rate fields for the case (a) are shown.

Finally, in Figure 4.37 we show how the maximum value of the temperature behaves for different mesh resolutions and polynomial degrees. The temperature tends to a limit value, and we observe how this value is reached already for coarse meshes when using a polynomial degree of three or four. We also observe that for  $k = 2$  the temperature tends to a limit value, but slower in comparison to  $k = 3$  or  $4$ . The values for  $k = 1$  are not displayed because for the mesh resolutions shown here, the values of the maximum temperature were of the order of 50 K bigger than the limit value. We note that the solution of this configuration showed singularities in the boundary points where the inlet and wall meet. This fact made hard to realize a  $h$ -convergence study for the complete domain. Based on this we decided to analyse a flame configuration that doesn't exhibit this behaviour, as shown in the next section.

We note that the solution of this configuration showed singularities in the boundary points where the inlet and wall meet, which induces a pollution phenomenon on the accuracy of the solution. This fact made hard to realize an  $h$ -convergence study for the complete domain. Based on this fact we decided to analyze a flame configuration that does not exhibit this behaviour, as shown in the next section.

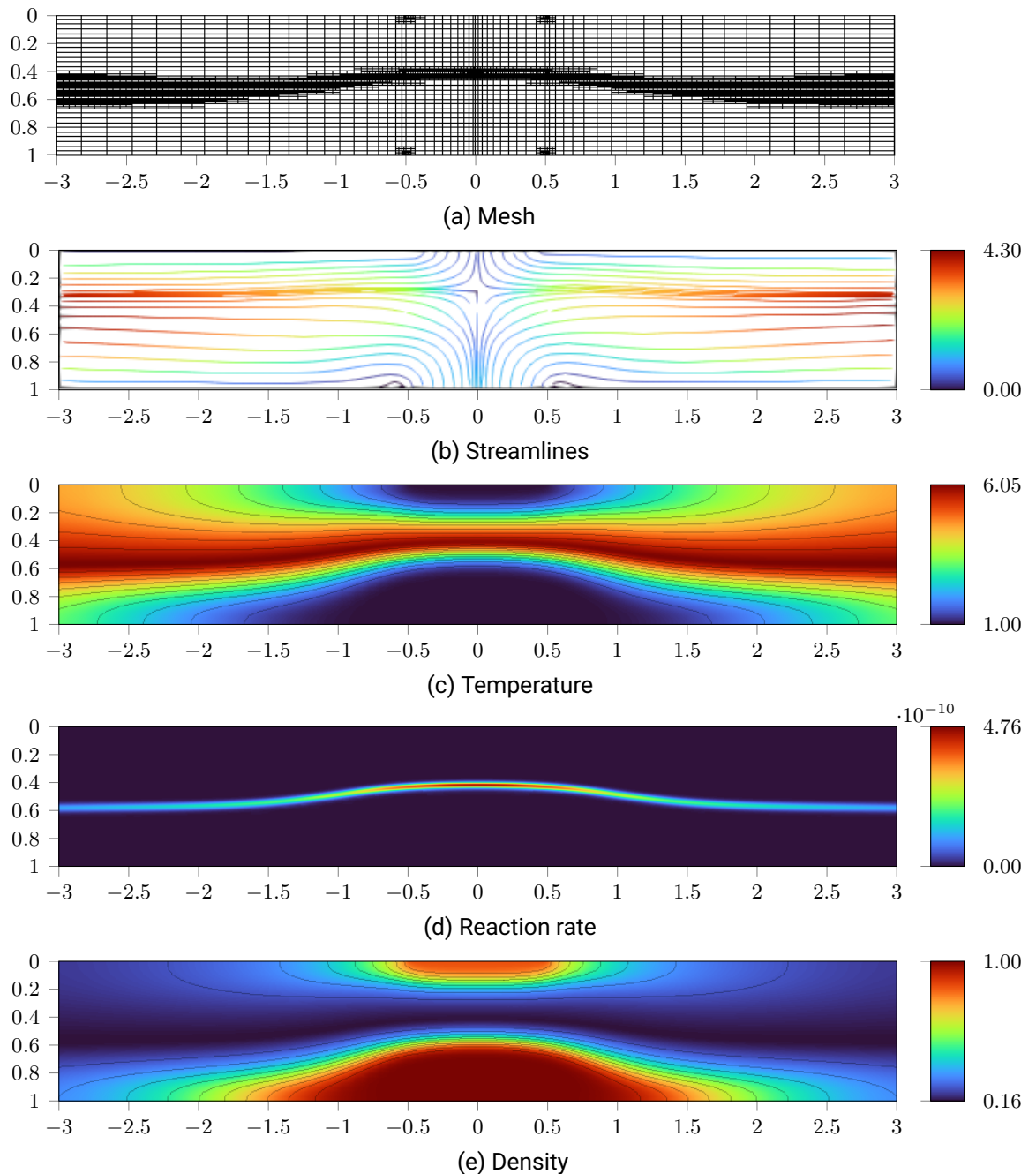


**Figure 4.34:** Nondimensional solution and derived fields of the counterflow flame configuration for case (a).

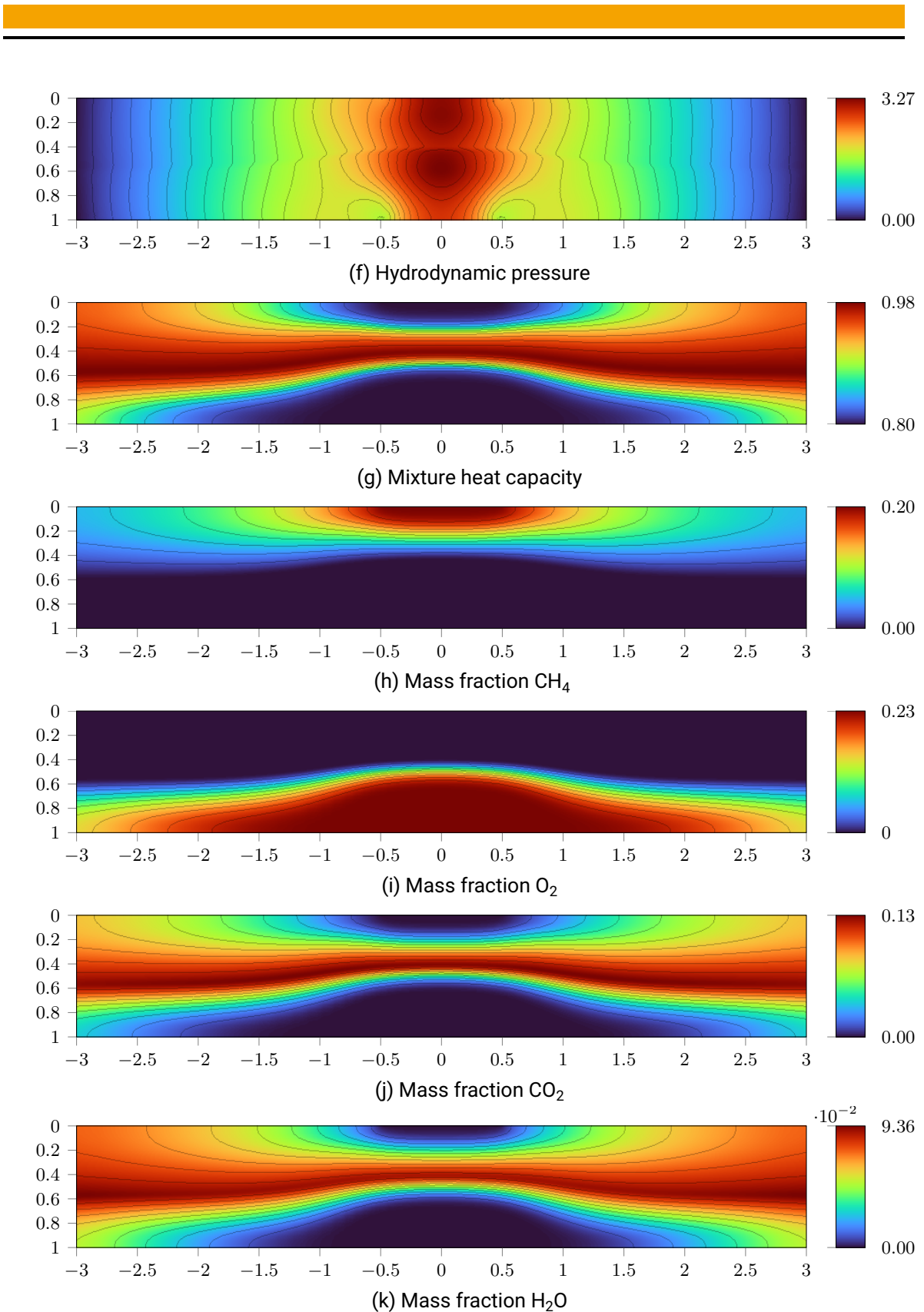


**Figure 4.34:** Solution and derived fields of the counterflow flame configuration with a strain of  $34\text{ s}^{-1}$  (continued).

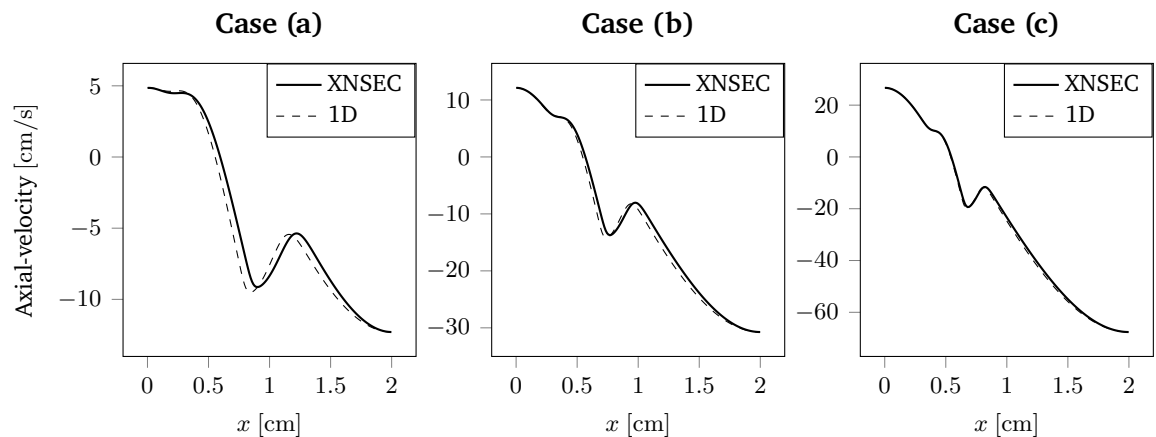


**Figure 4.35:** Comparison of the axial velocity calculated with the XNSEC-solver and the one-dimensional approximation.

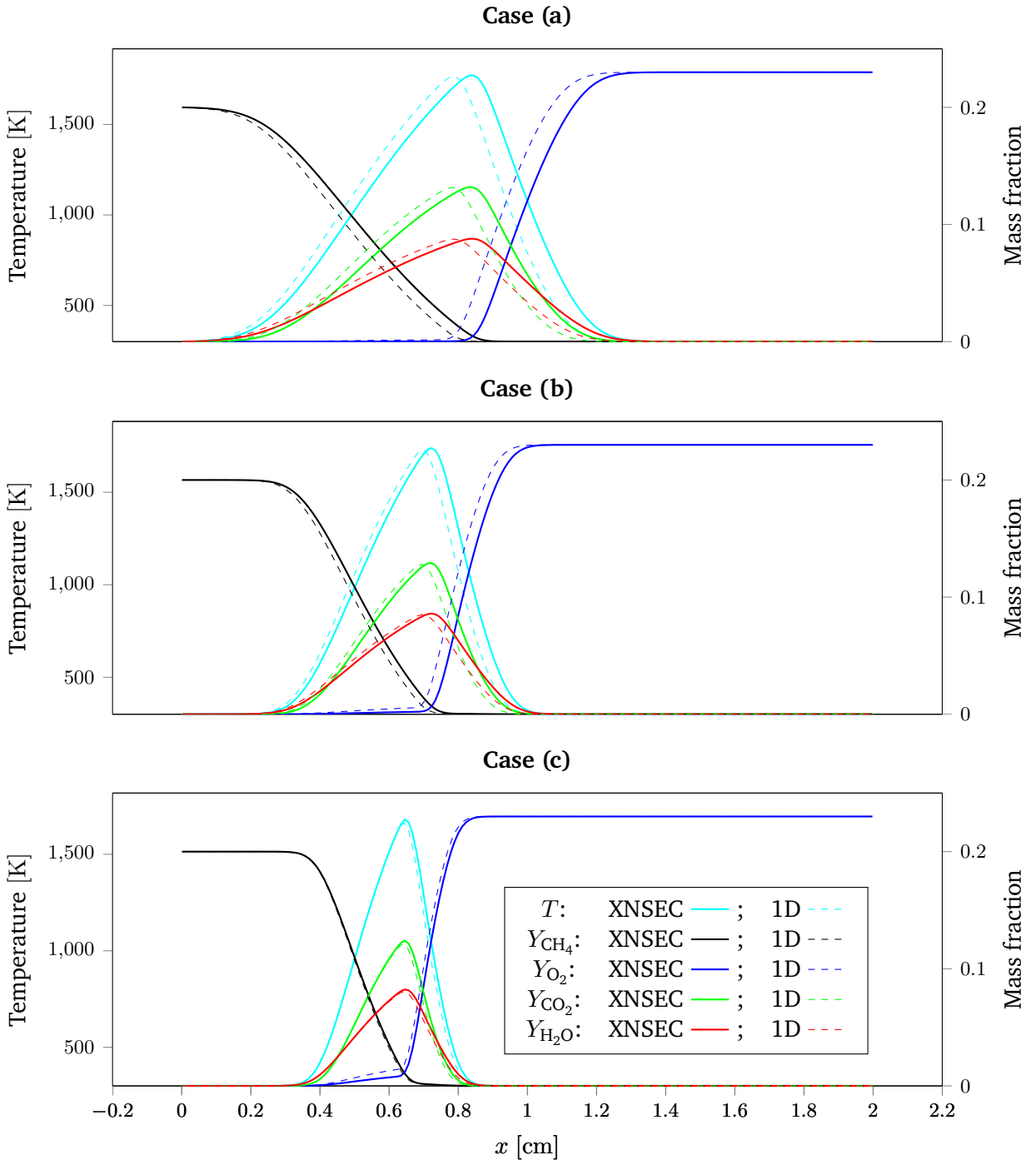


**Figure 4.36:** Comparison of temperature and mass fraction fields obtained with BoSSS and the one-dimensional approximation.

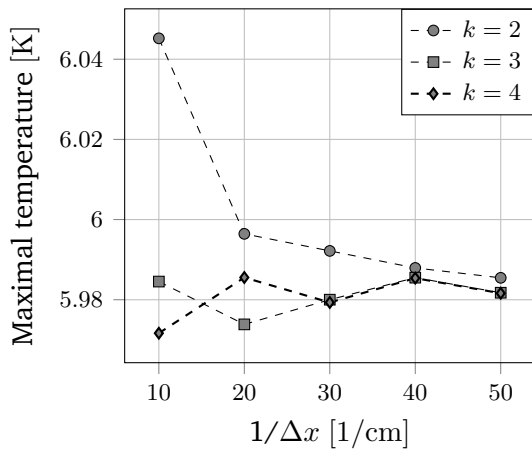


**Figure 4.37:** Maximum value of the temperature for the counter diffusion flame configuration, for different mesh sizes in the x-direction and polynomial degrees. Values for  $k = 1$  are not shown, because for this range of cell lengths the maximum temperature value was of the order of 50K higher than the ones depicted here.

### 4.3.3 Chambered diffusion flame

The chambered diffusion flame configuration has served as a model for many theoretical studies related to diffusion flames Matalon and Metzner, 2010; Rameau and Schmidt-Lainé, 1985; Matalon et al., 1980. A scheme of the configuration can be seen in Figure 4.38. Fuel is injected at a constant rate into the bottom of a small insulated chamber, while oxidant diffuses into the system against the direction of flow. Constant conditions at the outlet of the chamber are achieved by a rapid renewal of the flow of oxidant. Under these conditions a planar flame forms far away from the walls, which allows a one-dimensional description of the flame structure. The fuel inlet into the chamber is modelled with a velocity inlet boundary condition Equation (2.36a), while the flow outlet at the top is considered an outlet as given by Equation (2.36d). Since we are interested in the flame in wall distance, it is sufficient to set the remaining boundary conditions as periodic boundaries. This effectively transforms the problem into a pseudo two-dimensional configuration.

In this test case we study the combustion of a  $\text{CH}_4\text{-N}_2$  mixture with air. The thermodynamic pressure  $\hat{p}_0$  is set equal to an ambient pressure of 101 325 Pa. The inlet velocity of the fuel jet is set to  $0.025 \text{ m s}^{-1}$  and its mass composition is  $Y_{\text{CH}_4}^0 = 0.2$  and  $Y_{\text{N}_2}^0 = 0.8$  while air has a composition  $Y_{\text{O}_2}^0 = 0.23$  and  $Y_{\text{N}_2}^0 = 0.77$ . The temperature of the fuel and air feed streams is 300 K. The length of the system  $L$  is equal to 0.015 m. For this configuration an  $h$ -convergence study is conducted, where uniform Cartesian meshes with  $5 \times 2^6$ ,  $5 \times 2^7$ ,  $5 \times 2^8$ ,  $5 \times 2^9$  and  $5 \times 2^{10}$  cells are used. The polynomial degrees are varied from 1 to 4 for velocity, temperature and mass fractions, and from 0 to 3 for pressure. Errors are calculated using the finest mesh as a reference solution. The results are shown in Figure 4.39 for variables  $u_x$ ,  $T$ ,  $Y_{\text{CH}_4}$  and  $p$ . The convergence results for other variables are similar and not shown here. We observe the expected slope increase with increasing polynomial degrees. For low polynomial degrees the orders of convergence are very close to the theoretical values. However for higher polynomial degrees we observe a slight deterioration of the convergence rate.

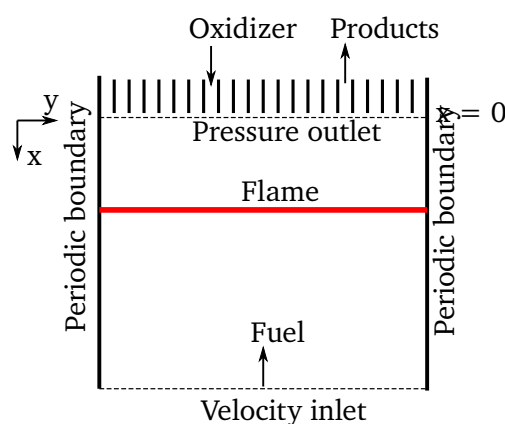


**Figure 4.38:** Schematic representation of the chambered diffusion flame configuration.

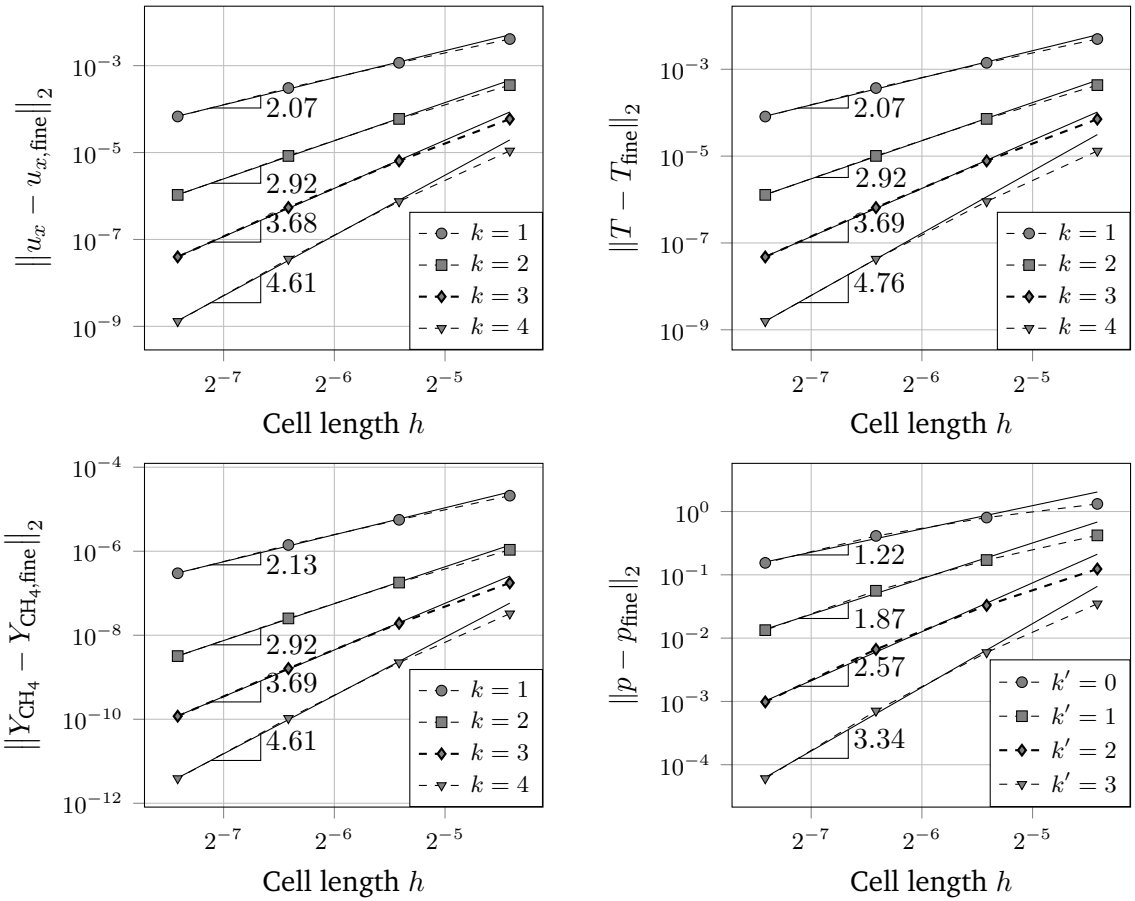


**Figure 4.39:** Convergence study for the chambered diffusion flame configuration.

## 5 Conclusion

---

In the present work we have shown the discretization using the DG method for the reactive low-Mach equations. A mixed order formulation has been used, where velocity, temperature and mass fractions are represented by polynomials of degree  $k$ , and pressure by polynomials of degree  $k - 1$ . The system obtained from the discretization was solved by means of a Newton-Dogleg type method. Additionally, a homotopy strategy for solving highly nonlinear systems was introduced and used for some of the presented test cases. For the reactive test cases the concept of the flame sheet estimate was demonstrated to be a useful and computationally cheap way of initializing the finite reaction rate combustion calculations. The solver was used to calculate three different benchmark configurations, one without combustion and two cases with combustion. The first of these is the differentially heated cavity. This benchmark case was solved for varying Rayleigh numbers, spanning from  $\text{Ra} = 10^2$  to  $\text{Ra} = 10^7$ . It was observed that for cases with Rayleigh number larger than  $10^5$  the use of our homotopy strategy was necessary to ensure convergence. Velocity and temperature profiles as well as thermodynamic pressure and Nusselt number were compared with a reference solution, obtaining very satisfactory results, thus validating our implementation of the method for variable density systems. An  $h$ -convergence study was presented for the differentially heated cavity, obtaining the expected convergence rates up to  $k = 4$ , where some degeneration on the rates was observed. Furthermore the counterflow diffusion flame configuration was analyzed, with which we intended to test the implemented chemistry model in conjunction with our solver. The results obtained with BoSSS were compared with results obtained by solving the self-similar one-dimensional representation of the counter diffusion flame configuration for varying strain rates. While for low strains some discrepancies between results were observed, the difference narrowed for high strains, which can be explained by the influence of the border effects on the centerline results for a two-dimensional configuration. Finally, the chambered diffusion flame configuration was used to study the convergence rates of our method. It was shown that, as expected, the convergence rates increase when using higher degree polynomials, but with some deterioration compared to the theoretical expected convergence. In future work the implemented solver is intended to be used in conjunction with our extended-DG solver Kummer, 2017; Kummer et al., 2021; Krause and Kummer, 2017 in order to study multiphase reactive systems such as droplets.



# Bibliography

---

- Armaly, B. F., Durst, F., Pereira, J. C. F., and Schönung, B. (1983). "Experimental and Theoretical Investigation of Backward-Facing Step Flow." In: *Journal of Fluid Mechanics* 127 (-1), p. 473. doi: [10.1017/S0022112083002839](https://doi.org/10.1017/S0022112083002839).
- Babuška, I. (1973). "The Finite Element Method with Lagrangian Multipliers." In: *Numerische Mathematik* 20.3, pp. 179–192. doi: [10.1007/BF01436561](https://doi.org/10.1007/BF01436561).
- Barkley, D., Gomes, G., and Henderson, R. (2000). "Three-Dimensional Instability in Flow over a Backward-Facing Step." In: *Journal of Fluid Mechanics* 473. doi: [10.1017/S002211200200232X](https://doi.org/10.1017/S002211200200232X).
- Bassi, F. and Rebay, S. (1997). "A High-Order Accurate Discontinuous Finite Element Method for the Numerical Solution of the Compressible Navier–Stokes Equations." In: *Journal of Computational Physics* 131.2, pp. 267–279. doi: [10.1006/jcph.1996.5572](https://doi.org/10.1006/jcph.1996.5572).
- Bird, R. B., Stewart, W. E., and Lightfoot, E. N. (1960). *Transport Phenomena*. New York: Wiley. 780 pp.
- Biswas, G., Breuer, M., and Durst, F. (2004). "Backward-Facing Step Flows for Various Expansion Ratios at Low and Moderate Reynolds Numbers." In: *Journal of Fluids Engineering* 126.3, pp. 362–374. doi: [10.1115/1.1760532](https://doi.org/10.1115/1.1760532).
- Botella, O. and Peyret, R. (1998). "Benchmark Spectral Results on the Lid-Driven Cavity Flow." In: *Computers & Fluids* 27, pp. 421–433. doi: [10.1016/S0045-7930\(98\)00002-4](https://doi.org/10.1016/S0045-7930(98)00002-4).
- Braack, M., Becker, R., Rannacher, R., and Warnatz, J. (1997). "An Adaptive Finite Element Method for Combustion Problems." In: *Proceedings of the Third Summer Conference, Numerical Modelling in Continuum Mechanics, Charles Universirt*.
- Burke, S. P. and Schumann, T. E. W. (1928). "Diffusion Flames." In: *Industrial & Engineering Chemistry* 20.10, pp. 998–1004. doi: [10.1021/ie50226a005](https://doi.org/10.1021/ie50226a005).
- Chandrasekhar, S. (1961). *Hydrodynamic and Hydromagnetic Stability*. Oxford: Oxford University Press.
- Cockburn, B., Karniadakis, G. E., and Shu, C.-W. (2000). "The Development of Discontinuous Galerkin Methods." In: *Discontinuous Galerkin Methods*. Ed. by B. Cockburn, G. E. Karniadakis, and C.-W. Shu. Lecture Notes in Computational Science and Engineering. Berlin, Heidelberg: Springer, pp. 3–50. doi: [10.1007/978-3-642-59721-3\\_1](https://doi.org/10.1007/978-3-642-59721-3_1).
- Dennis, J. E. and Schnabel, R. B. (1996). *Numerical Methods for Unconstrained Optimization and Nonlinear Equations*. Society for Industrial and Applied Mathematics. doi: [10.1137/1.9781611971200](https://doi.org/10.1137/1.9781611971200).
- Deuflhard, P. (2011). *Newton Methods for Nonlinear Problems*. Springer Series in Computational Mathematics. Berlin, Heidelberg: Springer Berlin Heidelberg. doi: [10.1007/978-3-642-23899-4](https://doi.org/10.1007/978-3-642-23899-4).

- Dobbins, R. R. and Smooke, M. D. (2010). “A Fully Implicit, Compact Finite Difference Method for the Numerical Solution of Unsteady Laminar Flames.” In: *Flow, Turbulence and Combustion* 85.3-4, pp. 763–799. doi: [10.1007/s10494-010-9278-z](https://doi.org/10.1007/s10494-010-9278-z).
- Fernandez-tarrazo, E., Sanchez, A., Linan, A., and Williams, F. (2006). “A Simple One-Step Chemistry Model for Partially Premixed Hydrocarbon Combustion.” In: *Combustion and Flame* 147.1-2, pp. 32–38. doi: [10.1016/j.combustflame.2006.08.001](https://doi.org/10.1016/j.combustflame.2006.08.001).
- Geisenhofer, M., Kummer, F., and Müller, B. (2019). “A Discontinuous Galerkin Immersed Boundary Solver for Compressible Flows: Adaptive Local Time Stepping for Artificial Viscosity-Based Shock-Capturing on Cut Cells.” In: *International Journal for Numerical Methods in Fluids* 91.9, pp. 448–472. doi: [10.1002/fld.4761](https://doi.org/10.1002/fld.4761).
- Girault, V., Rivière, B., and Wheeler, M. F. (2004). “A Discontinuous Galerkin Method with Nonoverlapping Domain Decomposition for the Stokes and Navier-Stokes Problems.” In: *Mathematics of Computation* 74.249, pp. 53–85. doi: [10.1090/S0025-5718-04-01652-7](https://doi.org/10.1090/S0025-5718-04-01652-7).
- Gutiérrez-Jorquera, J. and Kummer, F. (2022). “A Fully Coupled High-Order Discontinuous Galerkin Method for Diffusion Flames in a Low-Mach Number Framework.” In: *International Journal for Numerical Methods in Fluids* 94.4, pp. 316–345. doi: [10.1002/fld.5056](https://doi.org/10.1002/fld.5056).
- Hennink, A., Tiberga, M., and Lathouwers, D. (2021). “A Pressure-Based Solver for Low-Mach Number Flow Using a Discontinuous Galerkin Method.” In: *Journal of Computational Physics* 425, p. 109877. doi: [10.1016/j.jcp.2020.109877](https://doi.org/10.1016/j.jcp.2020.109877).
- Hennink, A. (2022). “Low-Mach Number Flow and the Discontinuous Galerkin Method.” In: doi: [10.4233/uuid:9b35b35a-0789-4883-a471-f8df0d7939ad](https://doi.org/10.4233/uuid:9b35b35a-0789-4883-a471-f8df0d7939ad).
- Johnson, R. F. and Kercher, A. D. (2020). “A Conservative Discontinuous Galerkin Discretization for the Chemically Reacting Navier-Stokes Equations.” In: *Journal of Computational Physics* 423, p. 109826. doi: [10.1016/j.jcp.2020.109826](https://doi.org/10.1016/j.jcp.2020.109826).
- Kao, P.-H. and Yang, R.-J. (2007). “Simulating Oscillatory Flows in Rayleigh–Bénard Convection Using the Lattice Boltzmann Method.” In: *International Journal of Heat and Mass Transfer* 50.17-18, pp. 3315–3328. doi: [10.1016/j.ijheatmasstransfer.2007.01.035](https://doi.org/10.1016/j.ijheatmasstransfer.2007.01.035).
- Karaa, S., Zhang, J., and Douglas, C. C. (2003). “Preconditioned Multigrid Simulation of an Axisymmetric Laminar Diffusion Flame.” In: *Mathematical and Computer Modelling* 38.3, pp. 269–279. doi: [10.1016/S0895-7177\(03\)90086-0](https://doi.org/10.1016/S0895-7177(03)90086-0).
- Kee, R. J., Coltrin, M. E., and Glarborg, P. (2003). *Chemically Reacting Flow: Theory and Practice*. Hoboken, N.J: Wiley-Interscience. 848 pp.
- Keshtiban, I., Belblidia, F., and Webster, M. (2003). “Compressible Flow Solvers for Low Mach Number Flows—a Review.” In: 23.
- Keyes, D. and Smooke, M. (1987). “Flame Sheet Starting Estimates for Counterflow Diffusion Flame Problems.” In: *Journal of Computational Physics* 73.2, pp. 267–288. doi: [10.1016/0021-9991\(87\)90137-9](https://doi.org/10.1016/0021-9991(87)90137-9).
- Kikker, A., Kummer, F., and Oberlack, M. (2020). “A Fully Coupled High-Order Discontinuous Galerkin Solver for Viscoelastic Fluid Flow.” In: *International Journal for Numerical Methods in Fluids* (). doi: [10.1002/fld.4950](https://doi.org/10.1002/fld.4950).

- Klein, B., Kummer, F., and Oberlack, M. (2013). "A SIMPLE Based Discontinuous Galerkin Solver for Steady Incompressible Flows." In: *Journal of Computational Physics* 237, pp. 235–250. doi: [10.1016/j.jcp.2012.11.051](https://doi.org/10.1016/j.jcp.2012.11.051).
- Klein, B., Müller, B., Kummer, F., and Oberlack, M. (2016). "A High-Order Discontinuous Galerkin Solver for Low Mach Number Flows." In: *International Journal for Numerical Methods in Fluids* 81.8, pp. 489–520. doi: [10.1002/fld.4193](https://doi.org/10.1002/fld.4193).
- Knikker, R. (2011). "A Comparative Study of High-Order Variable-Property Segregated Algorithms for Unsteady Low Mach Number Flows." In: *International Journal for Numerical Methods in Fluids* 66.4, pp. 403–427. doi: [10.1002/fld.2261](https://doi.org/10.1002/fld.2261).
- Krause, D. and Kummer, F. (2017). "An Incompressible Immersed Boundary Solver for Moving Body Flows Using a Cut Cell Discontinuous Galerkin Method." In: *Computers & Fluids* 153. doi: [10.1016/j.compfluid.2017.05.008](https://doi.org/10.1016/j.compfluid.2017.05.008).
- Kummer, F., Weber, J., and Smuda, M. (2021). "BoSSS: A Package for Multigrid Extended Discontinuous Galerkin Methods." In: *Computers & Mathematics with Applications*. Development and Application of Open-source Software for Problems with Numerical PDEs 81, pp. 237–257. doi: [10.1016/j.camwa.2020.05.001](https://doi.org/10.1016/j.camwa.2020.05.001).
- Kummer, F. (2012). "The BoSSS Discontinuous Galerkin Solver for Incompressible Fluid Dynamics and an Extension to Singular Equations." PhD thesis. Darmstadt: Technische Universität.
- Kummer, F. (2017). "Extended Discontinuous Galerkin Methods for Two-Phase Flows: The Spatial Discretization." In: *International Journal for Numerical Methods in Engineering* 109.2, pp. 259–289. doi: [10.1002/nme.5288](https://doi.org/10.1002/nme.5288).
- Lv, Y. and Ihme, M. (2017). "High-Order Discontinuous Galerkin Method for Applications to Multicomponent and Chemically Reacting Flows." In: *Acta Mechanica Sinica* 33, pp. 1–14. doi: [10.1007/s10409-017-0664-9](https://doi.org/10.1007/s10409-017-0664-9).
- Majda, A. and Sethian, J. (1985). "The Derivation and Numerical Solution of the Equations for Zero Mach Number Combustion." In: *Combustion Science and Technology* 42.3-4, pp. 185–205. doi: [10.1080/00102208508960376](https://doi.org/10.1080/00102208508960376).
- Matalon, M. and Metzner, P. (2010). "The Effect of Thermal Expansion on Diffusion Flame Instabilities." In: *Journal of Fluid Mechanics* 647, pp. 453–472. doi: [10.1017/S0022112009993016](https://doi.org/10.1017/S0022112009993016).
- Matalon, M., Ludford, G. S. S., and Buckmaster, J. (1980). "Diffusion Flames in a Chamber." In: *Gasdynamics of Explosions and Reactive Systems*. Ed. by A. K. Oppenheim. Pergamon, pp. 943–959. doi: [10.1016/B978-0-08-025442-5.50058-5](https://doi.org/10.1016/B978-0-08-025442-5.50058-5).
- McBride, B., Gordon, S., and Reno, M. (1993). *NASA Thermodynamic Data Base*. NASA Technical Memorandum 4513.
- Miao, C. (2022). "High-Order Simulation of Low-Mach-Flows." Darmstadt: Technische Universität Darmstadt.
- Müller, B. (1998). "Low-Mach-Number Asymptotics of the Navier-Stokes Equations." In: *Journal of Engineering Mathematics* 34.1, pp. 97–109. doi: [10.1023/A:1004349817404](https://doi.org/10.1023/A:1004349817404).
- Nonaka, A., Day, M. S., and Bell, J. B. (2018). "A Conservative, Thermodynamically Consistent Numerical Approach for Low Mach Number Combustion. Part I: Single-level Integration." In: *Combustion Theory and Modelling* 22.1, pp. 156–184. doi: [10.1080/13647830.2017.1390610](https://doi.org/10.1080/13647830.2017.1390610).

- Pailiere, H., Viozat, C., Kumbaro, A., and Toumi, I. (2000). "Comparison of Low Mach Number Models for Natural Convection Problems." In: *Heat and Mass Transfer* 36.6, pp. 567–573. doi: 10.1007/s002310000116.
- Pandya, T. P. and Weinberg, F. J. (1964). "The Structure of Flat, Counter-Flow Diffusion Flames." In: *Proceedings of the Royal Society of London. Series A, Mathematical and Physical Sciences* 279.1379, pp. 544–561. JSTOR: 2414698.
- Pawlowski, R. P., Shadid, J. N., Simonis, J. P., and Walker, H. F. (2006). "Globalization Techniques for Newton–Krylov Methods and Applications to the Fully Coupled Solution of the Navier–Stokes Equations." In: *SIAM Review* 48.4, pp. 700–721. doi: 10.1137/S0036144504443511.
- Pawlowski, R. P., Simonis, J. P., Walker, H. F., and Shadid, J. N. (2008). "Inexact Newton Dogleg Methods." In: *SIAM Journal on Numerical Analysis* 46.4, pp. 2112–2132. JSTOR: 40233295.
- Paxion, S., Baron, R., Gordner, A., Neuss, N., Bastian, P., Thévenin, D., and Wittum, G. (2001). "Development of a Parallel Unstructured Multigrid Solver for Laminar Flame Simulations with Detailed Chemistry and Transport." In: *Numerical Flow Simulation II*. Ed. by E. H. Hirschel. Notes on Numerical Fluid Mechanics (NNFM). Berlin, Heidelberg: Springer, pp. 181–198. doi: 10.1007/978-3-540-44567-8\_11.
- Peters, N. and Williams, F. A. (1987). "The Asymptotic Structure of Stoichiometric Methane-Air Flames." In: *Combustion and Flame* 68.2, pp. 185–207. doi: 10.1016/0010-2180(87)90057-5.
- Peters, N. (1985). "Numerical and Asymptotic Analysis of Systematically Reduced Reaction Schemes for Hydrocarbon Flames." In: *Numerical Simulation of Combustion Phenomena*. Ed. by R. Glowinski, B. Larrouy, and R. Temam. Lecture Notes in Physics. Berlin, Heidelberg: Springer, pp. 90–109. doi: 10.1007/BFb0008654.
- Pietro, D. A. D. and Ern, A. (2012). *Mathematical Aspects of Discontinuous Galerkin Methods*. Mathématiques et Applications. Berlin Heidelberg: Springer-Verlag.
- Poinson, T. and Veynante, D. (2005). *Theoretical and Numerical Combustion*. R.T. Edwards, Inc. 544 pp. Google Books: cqFDkeVABYoC.
- Rameau, J. F. and Schmidt-Lainé, C. (1985). "Numerical Bifurcation in Chambered Diffusion Flames." In: *Numerical Simulation of Combustion Phenomena*. Lecture Notes in Physics. Berlin, Heidelberg: Springer, pp. 335–349. doi: 10.1007/BFb0008671.
- Rehm, R. and Baum, H. (1978). "The Equations of Motion for Thermally Driven, Buoyant Flows." In: *Journal of Research of the National Bureau of Standards* 83.3, p. 297. doi: 10.6028/jres.083.019.
- Rhebergen, S., Cockburn, B., and van der Vegt, J. J. (2013). "A Space–Time Discontinuous Galerkin Method for the Incompressible Navier–Stokes Equations." In: *Journal of Computational Physics* 233, pp. 339–358. doi: 10.1016/j.jcp.2012.08.052.
- Schenk, O., Gärtner, K., and Fichtner, W. (2000). "Efficient Sparse LU Factorization with Left-Right Looking Strategy on Shared Memory Multiprocessors." In: *BIT Numerical Mathematics* 40.1, pp. 158–176. doi: 10.1023/A:1022326604210.

- Schenk, O. and Gärtner, K. (2002). "Two-Level Dynamic Scheduling in PARDISO: Improved Scalability on Shared Memory Multiprocessing Systems." In: *Parallel Computing* 28.2, pp. 187–197. doi: [10.1016/S0167-8191\(01\)00135-1](https://doi.org/10.1016/S0167-8191(01)00135-1).
- Schenk, O. and Gärtner, K. (2004). "Solving Unsymmetric Sparse Systems of Linear Equations with PARDISO." In: *Future Generation Computer Systems*. Selected Numerical Algorithms 20.3, pp. 475–487. doi: [10.1016/j.future.2003.07.011](https://doi.org/10.1016/j.future.2003.07.011).
- Sharma, A. and Eswaran, V. (2004). "HEAT AND FLUID FLOW ACROSS A SQUARE CYLINDER IN THE TWO-DIMENSIONAL LAMINAR FLOW REGIME." In: *Numerical Heat Transfer, Part A: Applications* 45.3, pp. 247–269. doi: [10.1080/10407780490278562](https://doi.org/10.1080/10407780490278562).
- Shahbazi, K., Fischer, P. F., and Ethier, C. R. (2007). "A High-Order Discontinuous Galerkin Method for the Unsteady Incompressible Navier–Stokes Equations." In: *Journal of Computational Physics* 222.1, pp. 391–407. doi: [10.1016/j.jcp.2006.07.029](https://doi.org/10.1016/j.jcp.2006.07.029).
- Shadid, J. N., Tuminaro, R. S., and Walker, H. F. (1997). "An Inexact Newton Method for Fully Coupled Solution of the Navier–Stokes Equations with Heat and Mass Transport." In: *Journal of Computational Physics* 137.1, pp. 155–185. doi: [10.1006/jcph.1997.5798](https://doi.org/10.1006/jcph.1997.5798).
- Shahbazi, K. (2005). "An Explicit Expression for the Penalty Parameter of the Interior Penalty Method." In: *Journal of Computational Physics* 205.2, pp. 401–407. doi: [10.1016/j.jcp.2004.11.017](https://doi.org/10.1016/j.jcp.2004.11.017).
- Shen, W., Zhang, J., and Yang, F. (2006). "Newton's Method for Steady and Unsteady Reacting Flows." In: *ACM-SE* 44. doi: [10.1145/1185448.1185621](https://doi.org/10.1145/1185448.1185621).
- Shi, J.-M., Gerlach, D., Breuer, M., Biswas, G., and Durst, F. (2004). "Heating Effect on Steady and Unsteady Horizontal Laminar Flow of Air Past a Circular Cylinder." In: *Physics of Fluids* 16.12, pp. 4331–4345. doi: [10.1063/1.1804547](https://doi.org/10.1063/1.1804547).
- Shishkina, O. (2021). "Rayleigh–Bénard Convection: The Container Shape Matters." In: *Physical Review Fluids* 6.9, p. 090502. doi: [10.1103/PhysRevFluids.6.090502](https://doi.org/10.1103/PhysRevFluids.6.090502).
- Smooke, M. D., Mitchell, R. E., and Keyes, D. E. (1986). "Numerical Solution of Two-Dimensional Axisymmetric Laminar Diffusion Flames." In: *Combustion Science and Technology* 67.4-6, pp. 85–122. doi: [10.1080/00102208908924063](https://doi.org/10.1080/00102208908924063).
- Smooke, M. D. and Giovangigli, V. (1991). "Formulation of the Premixed and Nonpremixed Test Problems." In: *Reduced Kinetic Mechanisms and Asymptotic Approximations for Methane-Air Flames: A Topical Volume*. Ed. by M. D. Smooke. Lecture Notes in Physics. Berlin, Heidelberg: Springer, pp. 1–28. doi: [10.1007/BFb0035363](https://doi.org/10.1007/BFb0035363).
- Smooke, M. D. and Giovangigli, V. (1991). "Premixed and Nonpremixed Test Problem Results." In: *Reduced Kinetic Mechanisms and Asymptotic Approximations for Methane-Air Flames*. Ed. by M. D. Smooke. Vol. 384. Lecture Notes in Physics. Berlin/Heidelberg: Springer-Verlag, pp. 29–47. doi: [10.1007/BFb0035364](https://doi.org/10.1007/BFb0035364).
- Smooke, M. D. and Giovangigli, V. (1992). "Numerical Modeling of Axisymmetric Laminar Diffusion Flames." In: *IMPACT of Computing in Science and Engineering* 4.1, pp. 46–79. doi: [10.1016/0899-8248\(92\)90016-2](https://doi.org/10.1016/0899-8248(92)90016-2).
- Spalding, D. B. (1961). "Theory of Mixing and Chemical Reaction in the Opposed-Jet Diffusion Flame." In: doi: [10.2514/8.5626](https://doi.org/10.2514/8.5626).

- Stauch, R., Lipp, S., and Maas, U. (2006). "Detailed Numerical Simulation of the Auto-Ignition of Liquid Fuel Droplets." In: *Advances in High Performance Computing and Computational Sciences*. Ed. by Y. Shokin, M. Resch, N. Shokina, N. Danaev, and M. Orunkhanov. Berlin, Heidelberg: Springer, pp. 127–137. doi: [10.1007/978-3-540-33844-4\\_11](https://doi.org/10.1007/978-3-540-33844-4_11).
- Stauch, R. and Maas, U. (2007). "The Auto-Ignition of Single n-Heptane/Iso-Octane Droplets." In: *International Journal of Heat and Mass Transfer* 50.15, pp. 3047–3053. doi: [10.1016/j.ijheatmasstransfer.2006.12.005](https://doi.org/10.1016/j.ijheatmasstransfer.2006.12.005).
- Sung, C. J., Liu, J. B., and Law, C. K. (1995). "Structural Response of Counterflow Diffusion Flames to Strain Rate Variations." In: *Combustion and Flame* 102.4, pp. 481–492. doi: [10.1016/0010-2180\(95\)00041-4](https://doi.org/10.1016/0010-2180(95)00041-4).
- Sutherland, W. (1893). "LII. The Viscosity of Gases and Molecular Force." In: *The London, Edinburgh, and Dublin Philosophical Magazine and Journal of Science* 36.223, pp. 507–531. doi: [10.1080/14786449308620508](https://doi.org/10.1080/14786449308620508).
- Tyliszczak, A. (2014). "Projection Method for High-Order Compact Schemes for Low Mach Number Flows in Enclosures." In: *International Journal of Numerical Methods for Heat & Fluid Flow* 24.5, pp. 1141–1174. doi: [10.1108/HFF-07-2012-0167](https://doi.org/10.1108/HFF-07-2012-0167).
- Vierendeels, J., Merci, B., and Dick, E. (2003). "Benchmark Solutions for the Natural Convective Heat Transfer Problem in a Square Cavity with Large Horizontal Temperature Differences." In: *International Journal of Numerical Methods for Heat & Fluid Flow* 13.8, pp. 1057–1078. doi: [10.1108/09615530310501957](https://doi.org/10.1108/09615530310501957).
- Wang, A.-B., Trávníček, Z., and Chia, K.-C. (2000). "On the Relationship of Effective Reynolds Number and Strouhal Number for the Laminar Vortex Shedding of a Heated Circular Cylinder." In: *Physics of Fluids* 12.6, pp. 1401–1410. doi: [10.1063/1.870391](https://doi.org/10.1063/1.870391).
- Westbrook, C. K. and Dryer, F. L. (1981). "Simplified Reaction Mechanisms for the Oxidation of Hydrocarbon Fuels in Flames." In: *Combustion Science and Technology* 27.1-2, pp. 31–43. doi: [10.1080/00102208108946970](https://doi.org/10.1080/00102208108946970).
- Williams, F. A. (2000). *Combustion Theory: The Fundamental Theory of Chemically Reacting Flow Systems*. 2. ed., [Nachdr.] Combustion Science and Engineering Series. Cambridge, Mass: Perseus Books. 680 pp.
- Xie, W. and Xi, G. (2016). "Fluid Flow and Heat Transfer Characteristics of Separation and Reattachment Flow over a Backward-Facing Step." In: *International Journal of Refrigeration* 74. doi: [10.1016/j.ijrefrig.2016.10.006](https://doi.org/10.1016/j.ijrefrig.2016.10.006).
- Xu, Y. and Smooke, M. D. (1993). "Application of a Primitive Variable Newton's Method for the Calculation of an Axisymmetric Laminar Diffusion Flame." In: *Journal of Computational Physics* 104.1, pp. 99–109. doi: [10.1006/jcph.1993.1012](https://doi.org/10.1006/jcph.1993.1012).
- Zhou, Y., Zhang, R., Staroselsky, I., and Chen, H. (2004). "Numerical Simulation of Laminar and Turbulent Buoyancy-Driven Flows Using a Lattice Boltzmann Based Algorithm." In: *International Journal of Heat and Mass Transfer* 47.22, pp. 4869–4879. doi: [10.1016/j.ijheatmasstransfer.2004.05.020](https://doi.org/10.1016/j.ijheatmasstransfer.2004.05.020).



# Curriculum vitae

---

Vor- und Nachname

## Persönliche Daten

Geburtsdatum: -

Geburtsort: -

Staatsangehörigkeit: -

## Schulbildung

Jahr - Jahr -

Jahr - Jahr -

## Studium

Jahr - Jahr -

## Wissenschaftliche

### Tätigkeit

Jahr - Jahr

Wissenschaftlicher Mitarbeiter am Fachgebiet für Strömungsdynamik im Fachbereich Maschinenbau der TU Darmstadt, Promotion und Lehrtätigkeit